DESIGN OF CHEMICAL SENSORS BASED ON SURFACE ENHANCED RAMAN SCATTERING

SUBMITTED IN PARTIAL FULFILMENT OF THE REQUIREMENTS
FOR THE AWARD OF THE DEGREE
OF

MASTERS OF TECHNOLOGY (2018-20)

IN

MICROWAVE & OPTICAL COMMUNICATION

Submitted by:

Varun Prasher

2K18/MOC/04

Under the supervision of

DR. YASHNA SHARMA

DEPARTMENT OF ELECTRONICS & COMMUNICATION ENGINEERING
DELHI TECHNOLOGICAL UNIVERSITY
(Formerly Delhi College of Engineering)
Bawana Road, Delhi – 110042

AUGUST, 2020

DESIGN OF CHEMICAL SENSORS BASED ON SURFACE ENHANCED RAMAN SCATTERING

SUBMITTED IN PARTIAL FULFILMENT OF THE REQUIREMENTS
FOR THE AWARD OF THE DEGREE
OF

MASTERS OF TECHNOLOGY (2018-20)

IN

MICROWAVE & OPTICAL COMMUNICATION

Submitted by:

Varun Prasher

2K18/MOC/04

Under the supervision of
DR. YASHNA SHARMA

DEPARTMENT OF ELECTRONICS & COMMUNICATION ENGINEERING
DELHI TECHNOLOGICAL UNIVERSITY
(Formerly Delhi College of Engineering)
Bawana Road, Delhi – 110042

AUGUST, 2020

DEPARTMENT OF ELECTRONICS & COMMUNICATION ENGINEERING

DELHI TECHNOLOGICAL UNIVERSITY

(Formerly Delhi College of Engineering)

Bawana Road, Delhi-110042

CANDIDATE'S DECLARATION

I, Varun Prasher, Roll No. 2K18/MOC/04, student of M.Tech (Microwave and Optical Communication), hereby declare that the project Dissertation titled "**Design of Chemical Sensors based on Surface Enhanced Raman Scattering**" which is submitted by me to the Department of Electronics and Communication Engineering, Delhi Technological University, Delhi in partial fulfilment of the requirement for the award of the degree of Master of Technology, is original and not copied from any source without proper citation. This work has not previously formed the basis for the award of any Degree, Diploma Associateship, Fellowship or other similar title or recognition.

Place: Delhi Varun Prasher

Date:17Aug 2020

Department of Electronics & Communication Engineering
Delhi Technological University
(Formerly Delhi College of Engineering)
Bawana Road, Delhi-110042

CERTIFICATE

I hereby certify that the Project Dissertation titled "Design of Chemical Sensors based on Surface Enhanced Raman Scattering" which is submitted by Varun Prasher, Roll No. 2K18/MOC/04, Department of Electronics & Communication Engineering, Delhi Technological University, Delhi in partial fulfillment of the requirement for the award of the degree of Master of Technology is a record of the project work carried out by the student under my supervision. To the best of my knowledge this work has not been submitted in part or full for any Degree or Diploma to this University or elsewhere.

(Digital signatures)

Place: Delhi

Date: 17Aug 2020

DR. YASHNA SHARMA

SUPERVISOR

(Assistant Professor)
Department of Electronics and Communication Engineering,
Delhi Technological University,
Bawana Road, Delhi – 110042

ABSTRACT

When light waves, with a specific wavelength, are incident on a metal-dielectric interface or on a nanoparticle, surface plasmons, localized surface plasmons or coupled plasmons are excited and lead to intensity enhancement. This phenomenon of light enhancement can be achieved by fabricating nanostructures with specific geometries and parameters. When these nanostructures are engineered appropriately, they result into light intensity enhancement of the order of tens of thousands. The phenomenon of electric field enhancement by using nanostructure with sharp edges, called lightning rod effect, can be exploited to further intensify the localized surface plasmons. For further enhancement of electric field intensity the possibility of enclosing these nanostructures within nano-line grating walls was explored. Variation of different parameters of these structures like orientation, gap and structural dimensions is explored for their influence on electromagnetic field enhancement. By optimizing these nanostructures, this work aims to propose an optimal nanostructure with high electromagnetic enhancement, for sensing chemical agents in trace quantities.

ACKNOWLEDGEMENT

I would like to thank my thesis mentor Dr. Yashna Sharma of Electronics and Communication Engineering Department at Delhi Technological University. She persistently guided me with new ideas and has always been welcoming to inputs from me. Her endeavor to keep herself abreast of new developments in the field and keenness to share her knowledge has always enabled me to put my efforts in right direction.

Dr. Yashna Sharma with her support, motivation and encouragement throughout the period this work was carried out, has not only supervised the project but has always enabled the keep going of project at right pace. Her readiness for consultation at all times, her educative comments, her concern, assistance and level of involvement up to minutest of the details have been instrumental. I would also like to thank all my family and friends for providing me with consistent support and continuous encouragement throughout through the process of researching and writing this thesis. This accomplishment would not have been possible without them.

Thank you.

Date: 17 Aug 2020

Varun Prasher
(2K18/MOC/04)

CONTENTS

LIST OF TABLES

LIST OF FIGURES

LIST OF ABBREVIATIONS

LSPR	Localized Surface Plasmon Resonance
SPP	Surface Plasmon Polaritons
SPR	Surface Plasmon Resonance
SPP	Surface Plasmon Polariton
FDTD	Finite Difference Time Domain
RI	Refractive Index
LSP	Localized Surface Plasmon
SERS	Surface Enhanced Raman Spectroscopy
SNOM	Scanning Near-field Optical Microscopy
SEM	Scanning Electron Microscope
TEM	Transmission Electron Microscopy

CHAPTER 1

INTRODUCTION

In defense and security sector, one of the most challenging and important tasks is to detect explosives and chemical warfare agents in minute quantities. Highly explosive materials like TNT and RDX and other potentially noxious substances like pathogenic viruses, bacteria and toxic chemical agents used in war which may have minor effects like irascibility on skin and eyes to severe consequences like choking and damage of human organs, must be identified at very low concentration levels to safeguard humanity and to prevent their heinous utilization against population. Continuous efforts have been put in past decades to device a quick, reliable economical and practical analytical tool which can identify multitudes of perilous material. Surface Enhanced Raman Spectroscopy has emerged as one of the most widely used detection techniques with accuracy of detection of even up to a level of single molecule.

For the fabrication of substrates with high electromagnetic enhancement, many anisotropic shapes have come up for their exceptional SERS enhancement. Few of those which are iteratively studied and evaluated are stars [59], triangles [57], [58] flowers [60] [33] among others. In order to make robust and inexpensive surface enhanced Raman spectroscopy substrates, the SERS active nanoparticles are synthesized by applying a thin coating of gold and silver on prefabricated affordable substrates like paper and dielectrics [61][62]. There are various methodologies available for the fabrication of SERS active nanostructures such as:

(a) Lithography

(b) Solution based synthesis

(c) Galvanic displacement reaction

(d) Chemical reduction method, and others

All these techniques are elaborated upon in a later subsection. All these techniques have got their respective associated pros and cons while obtaining one dimensional, two dimensional and three dimensional substrates. Solution-based synthesis using surfactants is quicker than lithography for large-scale fabrication but finds a problem with the organic layer rendering reduced efficacy and lowered sensitivity towards SERS phenomenon. The galvanic displacement on the other hand, provides clear surface, which in turn is more felicitous for surface enhanced Raman spectroscopy. The chemical reduction makes use of sacrificial templates for achieving highly SERS active substrates.

In past studies, it was brought out that different nanostructure shapes such as star shaped, triangular, square, rhombus, spherical ellipsoid produce different SERS enhancement factors. In this work, we considered spherical and ellipsoidal shaped nanoparticles, followed by analysis of triangular nanoparticles/nano-plates for their SERS enhancement factors. Besides this, different inter-arrangements of the bowtie were studied to achieve the best EM hotspot. The resonance wavelength and respective hotspot intensity is obtained and studied to bring out an optimal nano structure in context of maximum enhancement factor.

Noble metals in particular gold and silver are utilized for SERS applications due to their inert behaviour, and lesser losses [63]. In known laboratory atmospheric ambient conditions, gold nano-structures are preferred over silver ones due to their higher surface stability; therefore only gold is considered in this work.

1.1 AIM AND OBJECTIVE

In non-destructive in situ chemical detection at small scales of molecular level it is desired to use highly sensitive and accurate techniques like SERS. Surface Enhanced Raman Spectroscopy may facilitate detection of molecular occurrences by differentiating the products of a chemical reaction. High sensitivity of SERS detection techniques enables it to detect a trace quantity. This work will aim towards developing an SERS substrate with maximum surface enhancement so that it can be used for detection of trace amounts of chemical explosives for defense services of the country.

CHAPTER 2

LITERATURE REVIEW

2.1 SCATTERING

Scattering is the phenomenon of absorbing light by non-uniform surfaces and thereafter emission of light at different wavelength and energy. There are two theories about the nature of light - one states that it bears properties of wave while the other states that it displays characteristics of particle. The scattering phenomenon may be explained as the atoms of matter absorb the photons, i.e. light particles, if it has the appropriate energy to excite that atom. This absorbed energy shifts the electron of atom to higher energy levels, which on their return to lower ground energy state emit photon with certain wavelength and energy. The emitted photon may have same wavelength as incident light or may be larger or shorter than the incident light defining the type of scattering. The two types of scattering phenomena are as follows:

(a) Rayleigh scattering and

(b) Raman scattering.

2.1.1 Rayleigh Scattering

Lord Rayleigh was the first to realize the phenomenon of air molecules breaking up light into its constituent wavelengths. When the light passes through atmosphere it gets scattered due to gas molecules, this type of scattering is known as Rayleigh scattering. The process behind scattering is light absorption by a molecules and then radiation in a different direction. Scattering phenomenon is dependent on two factors:

(a) Wavelength of incident light.

(b) Size of particle that scatters the incident light.

The extent of scattering is inversely proportional to the wavelength raised to the power of four. This is the reason that smaller wavelengths are most scattered than larger wavelengths. It is known that visible blue light has smaller wavelength than red light which is why the sky looks blue due to more scattering of blue colour wavelength in atmosphere.

In terms of energy state diagram, Rayleigh scattering maybe easily understood from Fig. 2.1. It may be seen on the left that in ground state electron has got three states of vibration which have got their respective energies With incidence of monochromatic light the electron gets excited and rises to virtual energy state. Energy exchanged between photon and electron is given by

$$E=h\upsilon$$

Where υ = frequency of incident photon

h = Boltzmann constant

In virtual energy state, electron cannot stay for long and returns to a lower energy level. This translation of electron from higher to lower energy decides the type of scattering. If the electron emits same amount of energy as absorbed, the released photon has the same wavelength as that of incident photon as shown in Fig. 2.1(c). This is called Rayleigh scattering as incident and emitted wavelength are same.

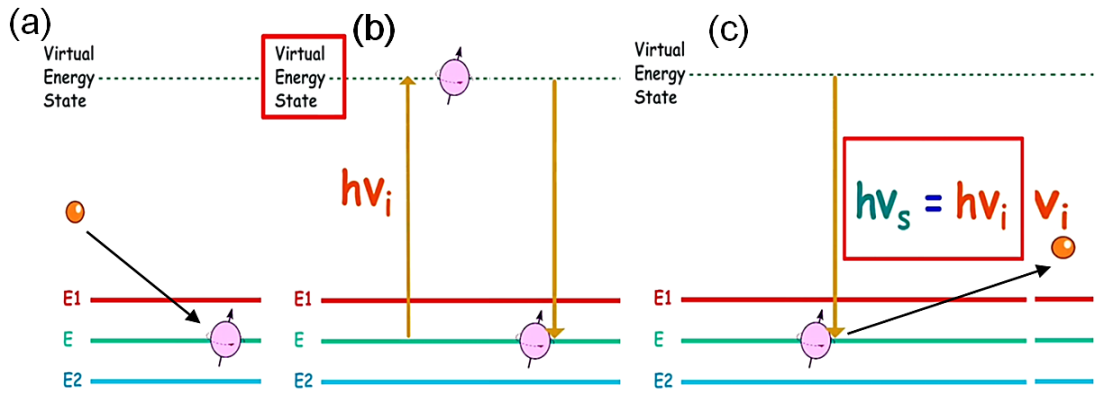

Figure 2.1 Rayleigh scattering: (a) incidence of photon with energy E=hυi on an electron, (b) electron gained energy ($h\upsilon_i$) from photon and raised to a virtual energy state and (c) electron returns from excited state to original ground state emitting energy (scattered energy $E_s = h\upsilon_s = h\upsilon_i$) [87]

According to the Rayleigh principle of scattering, the blue light with shorter wavelength scatters more and travels less. On the other hand, red light with smaller wavelength scatters less and is able to travel more. Therefore, during day time sky looks blue due to more scattered blue light, but reaches the observer due to lesser distance from sun, while in the evening and morning the red light scatters less and is able to travel more to reach the observer, at the same time blue scatters more and gets attenuated before reaching the observer. Therefore, sun appears red during its rise and set. As shown in fig. 2.2(a) light may be divided into its constituent wavelengths by a prism. Violet has the smallest wavelength followed by other colors in the VIBGYOR pattern with red having largest invisible light spectrum.

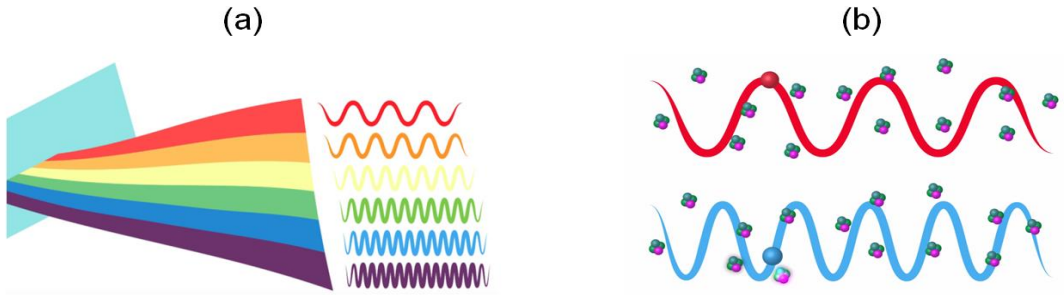

Figure 2.2 (a) When white light is split into its constituent colours/ wavelengths then it is observed that violet is most scattered while the red is least scattered (b) path traversed by the blue photon is longer than that by red photon therefore it experiences more scattering than red photon.

The wave path traversed by the red and blue photons in a medium may be considered here as shown in fig. 2.2(b). It may be easily noticed that the blue photon moves a lot more than red photons while travelling same distance. Therefore, it happens to strike more number of molecules while travelling the same distance and hence is dispersed more. In real life, blue light disperses six times more than red light. Hence blue light scatters more than the rest of light. This answers the basic question of why the sky is blue.

The atmosphere consists of gas molecules which are not visible but are present there to separate out different wavelengths of the visible incident light and scattering its blue element more than rest of the visible wavelengths, thus sky looks blue due to more scattered blue light.

2.1.2 Raman Scattering

In this section, the principle of Raman scattering and how it is different from the Rayleigh scattering will be discussed. Besides this, the two photon theory will be used to understand the concept of Raman scattering and generation of stokes lines and anti-stokes lines.

When the light is incident on a medium, it gets transmitted through it, but a small amount of light gets dispersed in the medium, this dispersion leads to scattering. As seen in the subsection 2.1.1, the light emitted has wavelength equal to that of the incident light giving rise to Rayleigh scattering but it may also happen that scattered wavelength is not equal to the incident photon wavelength. In the past studies, it was observed that about 1% of incident light when absorbed by medium is not reverted back by emission of same wavelength light but the wavelength emitted is different from the incident wavelength of light. This phenomenon of emission of light with different wavelength is known as Raman scattering.

This can be easily understood from following figure 2.3 using two photon theory. When electron is in its de-energized state i.e. not excited it stays in its ground state.

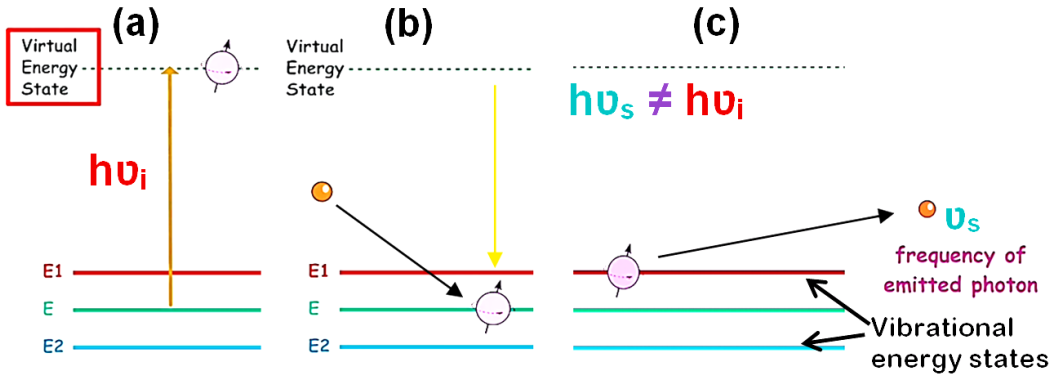

Figure 2.3 Raman Scattering: (a) incidence of photon with energy $E=h\upsilon_i$ on an electron in ground state, (b) electron gains energy ($h\upsilon_i$) from photon and rises to a virtual energy state and (c) electron returns from excited virtual energy state to either of the vibrational state and not to original ground state emitting energy [87] (scattered energy $E_s = h\upsilon_s \neq h\upsilon_i$).

Now point to note here is that there are two more energy levels close to the ground energy state of the electron. These two energy levels lie above and below the ground state and are called as vibrational energy levels. When Photon is incident on the electron it is excited to a virtual state of energy. Electron does not stay at its virtual excited state of energy for long and comes back to a lower energy level in a short span. But this time the lower energy state, which electron returns to is not the same as the ground state but is either of the vibrational levels. Due to this difference, the photon emitted bears different energy (hv_1) and hence a different wavelength than the incident one. This phenomenon is called as Raman scattering.

In simple words when the incident photon energy on an electron is not equal to the scattered energy i.e.

$$h\upsilon_s \neq h\upsilon_i$$

The scattering is termed as Raman scattering. This can be elaborated further using fig. 2.4.

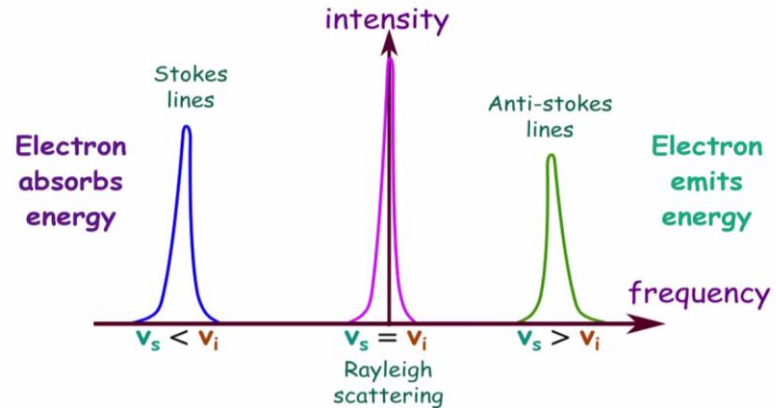

Figure 2.4 Raman Scattering giving rise to Stokes lines when frequency of scattered photon (υ_s) is less than frequency of incident photon (υ_i) and anti-stokes lines when frequency of scattered photon (υ_s) is greater than frequency of incident photon (υ_i) [87].

If the electron returns from virtual energy state to a vibrational state lower in energy then its ground state then the photon emitted has the higher energy as compared to incident light, i.e.

$$\upsilon_s > \upsilon_i$$

giving rise to anti stokes line. On the contrary when the electron returns to a vibrational state which lies higher than the ground energy state, then it emits a photon with lower energy than that of the photon absorbed while excitation of electron, i.e.

$$\upsilon_s < \upsilon_i$$

giving rise to Stokes lines.

2.2 SURFACE PLASMON

Surface plasmons (SPs) are coherent electron oscillations occurring at the interface between two materials; with condition that across the interface there is change of sign of real part of the dielectric function of the two materials, for example, a metal-dielectric interface and metal-air interface [88, 89].Surface Plasmons have the following properties (Hornyak et al)

(a) Occur on the surface of a metal,

(b) are quantized local electrons on the metal surface and

(c) Consist of collective oscillations of the free electron gas.

2.2.1 Surface Plasmon Polariton

Surface plasmon polaritons are electromagnetic disturbances which propagate at the metal-dielectric interface, momentarily appearing while in the direction perpendicular to the interface. These electromagnetic surface waves are a result of interaction of electromagnetic fields with free electron cloud available on the metal surface [90].

The coupling of the electromagnetic field and the surface charges results into an increased SPP momentum as compared to momentum of light in free space [53] as per SPP dispersion relation

$$K_{spp} = \mathrm{k}\sqrt{\frac{\varepsilon_d \cdot \varepsilon_m}{\varepsilon_d + \varepsilon_m}} \qquad \text{..... 2.1}$$

This yields to a momentum mismatch between light and SPP. [53] This mismatch must be overcome by coupling light and SPP modes at the interface when

$$\varepsilon_d + \varepsilon_m = 0.$$

The momentum of light and SPP can be matched using different coupler configurations such as prism couplers, grating couplers, fiber and waveguide couplers. These techniques are elaborated in section 2.3.

2.3 EXCITATION OF SURFACE PLASMON POLARITONS

"Surface plasmon" may be excited in following four ways of excitation.

(a) Prism coupling

(b) Grating coupling

(c) Using highly focused optical beam

(d) Near field excitation

All these excitation methodologies are elaborated in subsequent paragraphs.

2.3.1 Prism Coupling

In this technique, a prism like transparent structure is used to couple the light into surface plasmons. The prism used for coupling of light may either be hemispherical in shape or can be prism shaped. The hemispherical shaped coupling prism offers better coupling due to wider coupling angles presented by its structure, while the prism shaped glass prism will offer lesser coupling of light due to smaller coupling angles available with such structures. There are two methods to use prism for coupling [86] electromagnetic field to the substrate these are:

(a) Kretschmann Configuration

(b) Otto Configuration

Difference between these two techniques can easily be understood by the difference in the method to couple the light into surface plasmons. In Otto method, the analyte lies in between the prism and plasmon active metal layer. Otto method has inherited complexities due to uneven gap between metal surface and prism resulting into improper coupling of light. To overcome this complexity, Kretschmann came up with a different coupling technique in which the position of analyte and metal was interchanged; where the metal layer was between the analyte and prism. These two structural configurations of prism coupling technique may be better understood from Fig. 2.5.

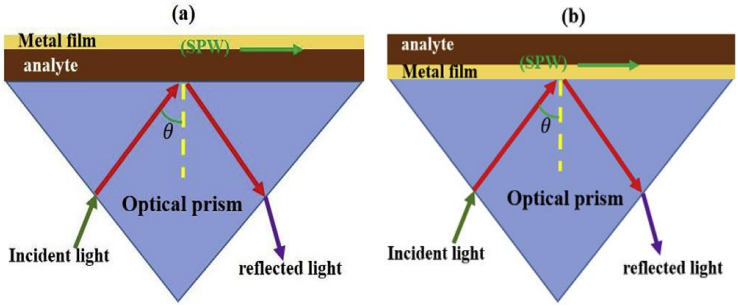

Figure 2.5 Prism coupling (a) Otto configuration, (b) Kretschmann configuration.

Due to its simplicity, prism coupling technique is most widely used excitation technique for excitation of surface plasmons. However there is drawback associated with this technique that it is often bulky.

2.3.2 Grating coupling

It is known that the wave vector of surface plasmon polaritons is longer as compared to the propagating electromagnetic field; hence it cannot excite the surface plasmon polaritons. To overcome the mismatch of wave vector between the in-plane momentum $k_x = k \sin \theta$ of incident photons and propagation constant of dielectric β, the metal surface is patterned with a shallow grating [90]. This grating can be one dimensional in the form of linear grooves or periodically occurring holes with lattice constant 'a'. In case of simple one-dimensional grooves (refer Fig. 2.6), following condition need to be satisfied for phase matching

$$\beta = k \sin \theta \pm Ug \qquad \text{..... 2.2}$$

Where $g = 2\pi/a$ is the reciprocal grating vector and $U = 1, 2, 3 \ldots$

As with prism coupling, excitation of SPPs is detected as a minimum in the reflected light.

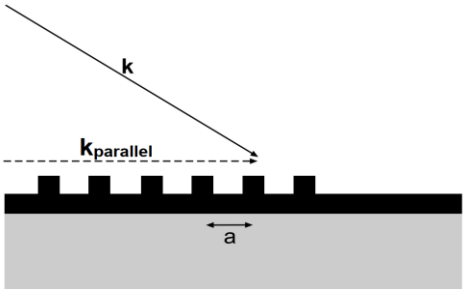

Figure 2.6 Phase-matching of light to SPPs using a grating [90].

It is known that the wave vector of surface plasmon polaritons is longer as compared to the propagating electromagnetic field; hence it cannot excite the surface plasmon polaritons. If grating period is made comparable to wavelength of surface plasmon polaritons, then it will permit matching of momentum and hence coupling into SPP. The reverse process can also take place: SPPs propagating along a surface modulated with a grating can couple to light and thus radiate. It is not necessary to craft the grating directly in the metal surface, but can be comprised of dielectric material.

2.3.3 Near Field Excitation

The pointed tip support is set in a manner such that the field distribution may be imaged with the help of an ordinary immersion microscope. The type of microscope is emerged in the refractive index matching fluid which is applied on the glass side. In this arrangement the excitation laser is on metal air interface side and detector microscope is on glass metal junction side.

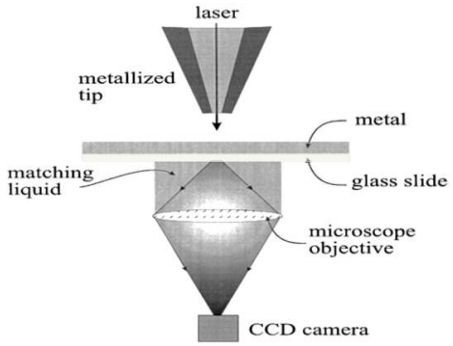

Figure 2.7 Schematic arrangement for far-field imaging the distribution of a localized surface plasmon excited in spatial domain.

2.4 SURFACE ENHANCED RAMAN SPECTROSCOPY (SERS)

Surface-enhanced Raman scattering (SERS) is a spectroscopic technique which is combination of modern laser spectroscopy techniques and the exciting optical properties of metallic nanostructures, which results in highly enhanced Raman signals when Raman molecules are brought in the nearfield zone of gold and silver nanostructures. The effect not only provides the structural details of Raman spectroscopy but also facilitates ultrasensitive detection limits, permitting Raman spectroscopy of single molecules [91].

Surface enhanced Raman scattering (SERS), exploits the generation of highly localized electromagnetic fields in the near-field region of metallic nanostructures for enhancing spontaneous Raman scattering of suitable molecules.

The Raman Effect (in respect of molecules) relates the inelastic scattering phenomenon between an incident photon and a molecule, occurring due to fundamental vibrational or rotational mode of the molecules, as depicted in Fig. 2.8.

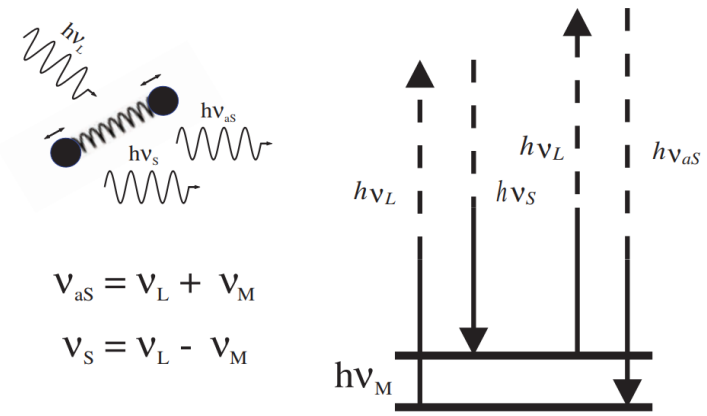

Figure 2.8 Schematic depiction of Raman scattering and fluorescence. (a) Generation of Stokes and anti-Stokes radiation via scattering events [91].

The spectrum of Raman spectroscopy shows much sharper transitions than that of fluorescence, therefore enabling a thorough analysis of the molecule considered. Usually the photons contributing towards Raman transitions are not in resonance with the molecule and the excitation occurs through virtual levels. Typical Raman scattering cross sections σ_{RS} are usually less than one tenth of the cross section of a fluorescent process,

i.e. typically 10-31 cm^2/molecule $\leq \sigma_{RS} \leq$ 10-29 cm^2/molecule [90]. The total power of the in-elastically scattered beam is linearly proportional to the intensity of the incident excitation beam. In Raman scattering for Stokes process the power of the scattered beam is given by

$$\mathbf{P_S(\upsilon_S) = N.\sigma_{RS}.I(\upsilon_L)} \qquad \textbf{……2.3}$$

Where N = number of Stokes-active scatterers within the excitation spot,

σ_{RS} = scattering cross section and

$I(\upsilon_L)$ = intensity of the excitation beam.

SERS is enhancement of this process, which is achieved by positioning the Raman-active molecules being studied inside the near-field region of a metallic nanostructure. The metallic nanostructure can be metallic colloidal nanostructures, explicitly arracnged group of nanoparticle or a roughened surface. The enhancement of scattered power P_S is due to two effects.

(a) Firstly, the Raman cross section σ_{RS} is enlarged, due to change of surroundings of the molecule. This increment in cross section ($\sigma_{SERS} > \sigma_{RS}$) is known as the chemical or electronic contribution to the Raman enhancement. The maximum enhancement due to increase in effective cross section is of the order of 100 [90].

(b) A more dominant factor contributing towards the total enhancement of scattered power PS is the increased electromagnetic field due to localized surface plasmons excitation and intensification of the electric field lines (lightning rod effect) at the interface of metal and dielectric [92]. As a result of this both incident and scattered light are enhanced. This electromagnetic enhancement factor is expressed as:

$$\mathbf{L}\,(\upsilon) = \frac{|\mathbf{E_{loc}}\,(\upsilon)|}{|\mathbf{E_0}|} \qquad \textbf{……..2.4}$$

where $|\mathbf{E}_{loc}|$ = local field amplitude at the Raman active site.

Under SERS conditions the total power of the Stokes beam is

$$P_S(\upsilon_s) = N \cdot \sigma_{SERS} \cdot L(\upsilon_L)^2 \cdot L(\upsilon_s)^2 \cdot I(\upsilon_L) \qquad \textbf{……..2.5}$$

It may be noted that the frequency difference $\Delta\upsilon = \upsilon_L - \upsilon_s$ between the incident photons frequency and the scattered photons frequency is negligibly smaller than the linewidth Γ of a localized surface plasmon mode, therefore $|\mathbf{L(\upsilon_L)}| \approx |\mathbf{L(\upsilon_s)}|$. Thus it is brought out that the contribution of this electromagnetic phenomenon to the total SERS enhancement is proportional to the fourth power of the field enhancement factor. Thus the power enhancement factor [92] of the Stokes beam is given by:

$$\mathbf{R} = \frac{|\mathbf{E_{loc}}|^4}{|\mathbf{E_0}|^4} \qquad \textbf{…….2.6}$$

The expression given by equation 2.6 for electromagnetic enhancement will be extensively used for calculation of enhancement factor in this work.

2.5 DIFFERENT FACTORS AFFECTING SURFACE ENHANCEMENT SPECTROSCOPY

Different physical arrangements of nanoparticles are proposed in past studies. Beside physical arrangement of nanoparticle there are many more factors which require attention while designing and SERS substrate. Few of these factors are listed below:

(a) Shape of nanoparticle grown on substrate

(b) Material of nanoparticles and substrate.

(c) Size of nanoparticle or nanostructure.

(d) Environment or filling material.

(e) Physical arrangement of nanoparticles.

(f) Spacing between nanoparticles.

(g) Illumination method and type of polarization.

2.5.1 SHAPE OF GROWN NANOPARTICLES

The nanoparticles deposited on the substrate definitely enhance the Raman spectroscopy sensitivity leading to phenomenon known as surface enhanced Raman spectroscopy, however the shape of the ground particles always has a major dictating role to play in defining the extent of enhancement and the resonance wavelength full stop in past works there are different Nano structures supposed to be grown or deposited on metallic or dielectric substrates few of these are listed below [28].

(a) Sphere [21] [18]

(b) Ellipsoid

(c) Rhombic plates/discs and square plates [21]

(d) Triangular plates [11], [13], [15]

(e) Circular discs

(f) Cylindrical (Nano wires)

Each of the mention the shapes have got their own pros and cons in context of is of preposition or growth method on substrate, improvisation of enhancement, adaptability to different structural arrangements and resonance wavelength. Different shapes provide different enhancements of electric field depending upon different permutations and combinations with other affecting factors as mentioned in beginning of this section.

2.5.2 MATERIAL OF SUBSTRATES AND NANO STRUCTURES DEPOSITED

Preparing a SERS substrate has always been a challenging task and an active area of concern for the researchers. With advent of new Nano technologies that facilitate attuning of attributes on nanoscale, specifically by chemical procedures has been attracting the attention of researchers for past decade [34]**.** SERS substrates can be categorized into two categories

(a) Conventional substrates. Conventional substrates are those which have noble metals like gold and silver as their constituents.

(b) Hybrid substrates. Hybrid substrates are those which have constituents of disparate chemical characteristics.

Both of these substrates are elaborated with their types in subsequent paragraphs.

2.5.2.1 Conventional substrate

It is evident that major contributor of enhancement of Raman signal in SERS is electromagnetic enhancement full stop this electromagnetic enhancement has court localized surface plasmon resonance LSPR as it's crucial benefactor. LSPR is grossly dependent on shape, size and material of substrate. In this section *only material aspect of substrate is considered*. Due to their LSPR attributes noble metals are extensively used for preparing SERS Nano structures full stop when size of nanostructure is increased, a corresponding increase in atmosphere is observed [32]. Particles which have sharp edges display higher resonance and Intel to better sensitivity than blunt edged particles of similar size and shape [65]**.** Local Surface Plasmon Resonance to occur the size of nanoparticle must be smaller than the wavelength of incident light; meanwhile it should not be too miniscule to produce insufficient polarization and the execrable plasmon resonance. When these nanoparticles are arranged in a particular pattern at nanoscales, then pattern configuration and spacing between nanoparticles will affect the coupling between the particles, which in turn has an important role to play in enhancement of SERS. Mainly there are two Nano structural formations of noble metals used as conventional substrate these are

(a) Metal Electrode

(b) Colloidal Metal Nanoparticles

Both of these nano structural formations of noble metals are elaborated in following subsections:

(a) **Metal electrode.** Electrodes are most extensively used for in-situ observation of electrochemical reactions and related systems. These are produced by refining and electrode by using "oxidation-reduction cycles" process giving an enhancement factor of 106 [34]. Oxidation-reduction cycles also known as redox is a a combination of two processes, occurring alternately, memory oxidation in which an atom loses electrons and reduction in which an atom gains electrons. Typically particles rising from 25 to 500 nm are produced on the electrode surface by redox reaction cycles. Structure of these particles depends on intensity of current flow on and hydrogen emission. The absorption property or ability to mind with analyte molecules increases due to refund surfaces of silver electrode.

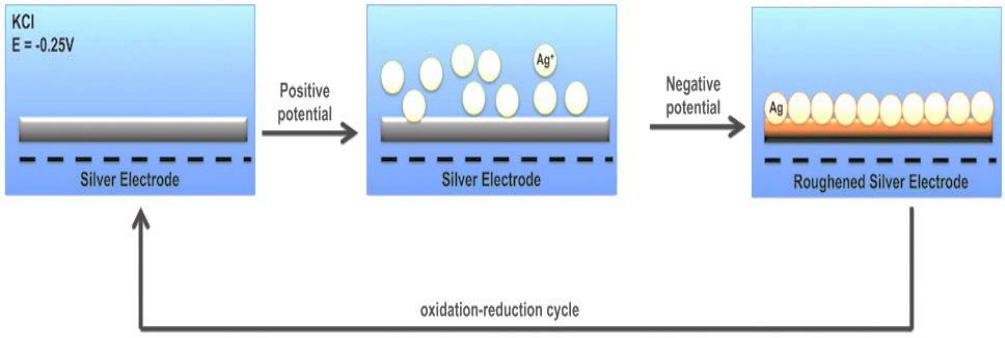

Figure 2.9 Schematic diagram of REDOX reaction of Au electrode in Potassium Chloride solution [34].

(b) Colloidal metal nanoparticles. Colloidal metal nanoparticles are currently used as SERS substrate due to their high sensing capability is in vastly different analytical and governments. With due course of advancement in field of SERS techniques has been developed to control the physical aspects like size and shape also their physical arrangement in an environment these are the three factors which have a substantial effect on SERS activity.

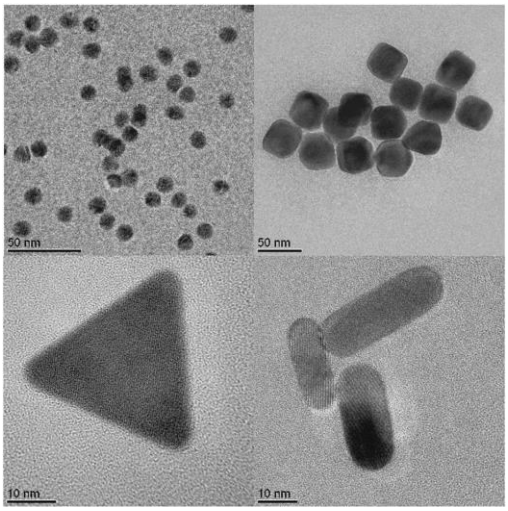

Figure 2.10 TEM images of Au NPs with spherical, cubic, triangular and cylindrical morphologies [34].

Fig. 2.10 shows different morphologies that can be utilized as SERS substrates. These metal colloids may be obtained by different methods namely chemical reduction method, laser ablation method or seed mediation depending upon shape of colloidal nanoparticles.

2.5.2.2 Hybrid substrates

Hybrid substrates, as name suggests, are derived from heterogeneous elements. Hybrid substrates may be further categorized into two types:

(a) Coupled inorganic materials

(b) Polymer composites

Both of these types of hybrid substrates are explained in following sections.

(a) Coupled Inorganic Materials. Inorganic materials due to their chemical and structural stability properties to withstand in adverse environmental conditions for long time were extensively used for production of SERS substrates by supporting active metals on solid structure surfaces this can be achieved in either of the two following SERS substrate surfaces.

(i) Metal Coated Surfaces. To obtain and SERS substrate metallic nanoparticles are adhere to inorganic material by chemical for

electrostatic process to stop this deposition of metal nanoparticles maybe in form of rough coating for in form of island on inorganic material. Different technical and environmental factors like the position rate, geometry coma temperature and annealing; play a crucial role in defining size and shape of nanostructure.

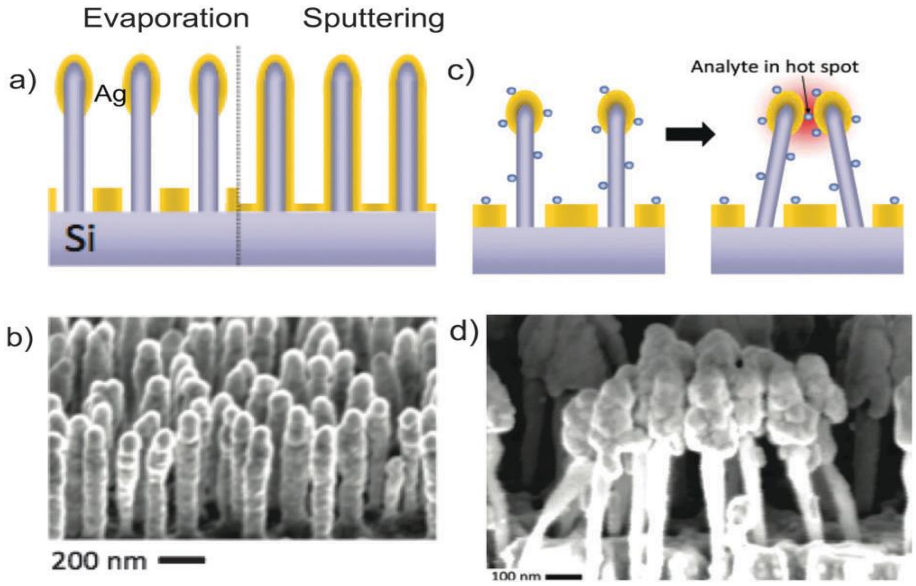

Figure 2.11 Metal coated surfaceS: (a) Evaporation and sputtering deposition of silver tips on silicon pillars while sputtering yields conformal coatings; (b) SEM image of the Ag coated silicon nano-pillars; (c) scheme of the enhancement mechanism – the solvent evaporates and this surface tension will pull the silicon nano-pillars together, trapping the analyte at the ''hot spot'' giving rise to a large Raman signal; (d) SEM image of a cluster of leaning silver coated silicon nano-pillars. Copyright Wiley Publishing Group (2012).

(ii) Core shell particles. As the name depicts core shell nanoparticles consists of a core made up of dielectric material which is covered by a shell made up of thin active metal. Also instead of dielectric metal core shell nanostructure both core and shell may be made of different metals and no dielectric. Core shell Nano structures in heriot advantage of tunable surface plasmon resonance frequency by wearing core and shell dimensions ratio and permit superlative SPR wavelength and excitation wavelength.

(iii) Metal carbon nanostructure. These are quite similar to core shell nanoparticles; with metal as code with carbon shell covering it full stop this metal nanoparticles covered with carbon are often used to make

tags which are compatible with biological analytes with an aim to immunoassays [66]. The graphene based hybrid substrates which are decorated with gold nanoparticles permitted SERS detection of Cyclo-Trimethylene Trinitramine (RDX) to as low quantity as 5 fm and Trinitrotoluene (TNT) at 10 fm.

(iv) Metal porous materials. The stable SERS substrate is obtained by subsuming metal nano particles in matrix of a porous material. Nipples material maybe porous glass ceramics for a cheaper option is templated nano-porous metals. These solid surface substrates have got advantage being fine stable mattresses due to my stability during manufacturing the process and lesser assemblage of metal nanoparticles. Such substrates have got uniform size distribution of nanoparticles and thus provide an option to use selective analyte on basis of size of pore.

(b) Polymer Composites Structures. Polymer composites have emerged as a new type of hybrid substrate containing SERS active metal particles of nanoscale. In such substrates, the matrix of polymer molecules is capable of controlling distance between metallic nanoparticles and abutting environment. There are several methods adopted to produce polymer nanocomposites but broccoli all of these fall into two broad categories.

(i) Intrinsic Technique. In this method metallic solids are chemically reduced while polymer Matrix acting as stabilizing platform for colloidal metal Nano structures.

(ii) Blending Technique. In this technique prefabricated metallic nanoparticles are mixed with polymer to make a homogeneous mixture or a blend of metal and polymer nanoparticles [23].

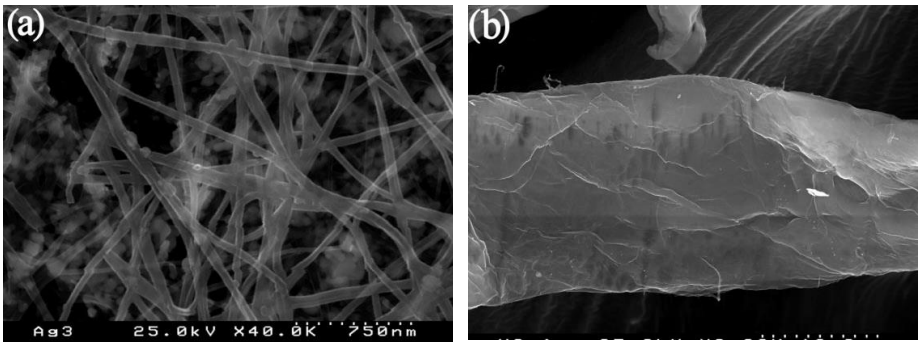

Figure 2.12 Polymer composites : Scanning electron microscopic images of (a) the silver in bacterial cellulose and (b) silver in vegetal cellulose nanocomposites [34].

2.5.3 SIZE OF NANO PARTICLES

Size of the SERS active nanostructure has a vital role to play defining plasmon resonance and electromagnetic field enhancement. The size of the metallic nanoparticles contributing towards SERS effect must be far smaller than the exciting radiation in past studies it is brought out that SERS active nanoparticles must have dimensions in between 5 nm to 100 nm. Also it was realized with time that source is best obtained with dimensions somewhere around 20 to 70 nm. On the contrary the SERS active nanoparticle must not be too minuscule (less than 5 nm), so that it does not swerve from its imitating bulky plasmon characteristics and display Quantum effect. For too small Nano structures, scattering of electrons on the surface will come into action, with an outcome of reduced electrical conductivity and telling to low polarization of nanoparticles, the scaling down plasmon resonance and in turn a SERS enhancement .

It is very well elaborated in past studies [67]. Plasmon resonance wavelength is dependent on size of nanoparticles. For instance resonant wavelength of 22.8 nm silver nano-particle is 406 nm while that of 37.8 nm nanoparticle display high enhancement of electric field at 428 nm. It is also brought out [68, 69] that when the nano-sphere is Elongated the resonance band of surface plasmon splits up into two parts first low frequency longitude and second high frequency Transverse part.

2.5.4 ENVIRONMENT

Environment here is mainly to do with the surroundings of the SERS active nanostructure. Thus environment can be divided into two parts

(a) Bridging material between SERS nanoparticles.

(b) Coupling medium between light and SERS active nanoparticles.

Both of these are discussed in the following subsections.

(a) Bridging Material Between SERS Nanoparticles. Material for filler material between SERS nanoparticles are usually polymers which acts as link between dimers and primers of cold. Different research groups have got different approaches towards linkers material. Free main contributors have been Feldheim, Huo, Wang and Sung and coworkers who used phenyl acetylene, acid-based mono-functional nanoparticles polyelectrolyte and solid phase Nano linkers.

(b) Coupling Medium Between Light and SERS Active Nanoparticles. Light coupling medium depends on excitation technique used to excite the surface plasmons. The coupling medium can be vacuum, air, glass or oil. The coupling medium plays a vital role to define the extent of light coupled with active metal and thus quantum of surface plasmon excitation in turn maximum enhancement factor.

2.5.5 Physical Arrangement of Nanoparticles

Physical arrangement of nanoparticles is considered in respect of other nanoparticles and polarization of source excitation. The nanoparticle arrangement can be categorized into three categories vis-a-vis:

(a) 1-dimensional nanoparticle array

(b) 2-dimensional nanoparticles array

(c) 3-dimensional nanoparticles array

(a) One Dimensional Nanoparticles Array. One dimensional nanoparticles array has been an alluring option for designing optical devices with Nano dimensions. Due to the property of captivating light between the nanoparticles the nanoparticle arrays have emerged as a strong beta for providing highly enhanced electromagnetic fields at junctures of adjoining nanoparticles. Recent studies have brought out that array of one dimensional nanoparticles is capable of amalgamating local electromagnetic field enhancement of adjacent nanoparticles arranged into one dimensional attractive manner and sharing to colossus electromagnetic field enhancement (of the order of |E|2>107), facilitating detection at the level of single molecule [70]. In another study it was brought out that a chain of similar nanoparticles with continuous decrease in size and spacing between nanoparticles will result in to magnificent electromagnetic field enhancement because of cascade effect [71]. These are further of two types:

(i) Solvent based one dimensional metal nanoparticle array.

(ii) Confronting nano-discs.

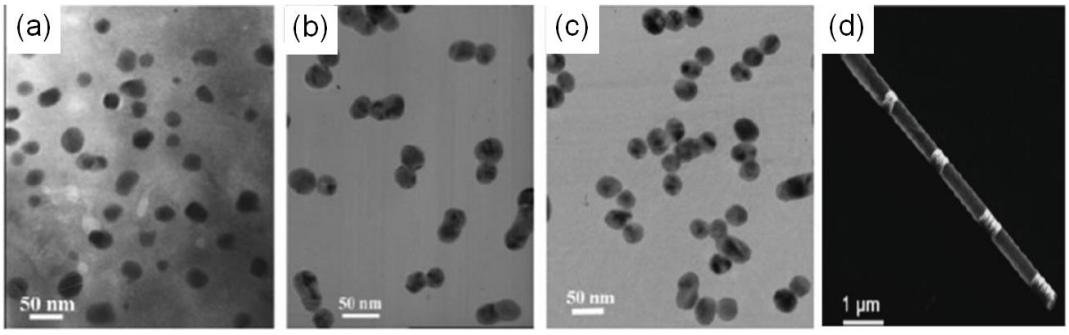

Figure 2.13 Transmission Electron Microscopy images of 1-D silver nanoparticle aggregates: (a) single particle colloids, (b) two, (c) three, (d) Scanning Electron Microscopy image of 1-D arrays of identical gold nano-disks with 120-nm thickness and 30-nm separation [21]. Copyright 2006, National Academy of Sciences.

(a) Two-dimensional SERS Substarte. Two dimensional Nano arrays consist of nanoparticles which are packed compactly and are periodically arranged along two of the three dimensional axis. Maximum density of hotspots can be

obtained on surface, with tightly packed nanoparticles providing enhanced Raman Effect due to long range effect. In two dimensional nanoparticles are the enhancement factor is manifold than those of disorganized metal nanoparticles. Due to procedural is most of the studies remained convert to small sized (5 to 50 nm) nanoparticles these arrays can be obtained by following four techniques:

(i) Self-assembly. Most popular technique to fabricate a two-dimensional array of nanoparticles. In this technique a drop of solution which contains active nanoparticles is evaporated onto a specially prepared substrate. The evaporation process will provide a well ordered array of nanoparticles because of mutual inference of capillary action and interfacial forces. [72, 73] Self-assembly technique has got an edge over conventional lithography technique by providing extremely squeezed inter partition arrangement with few nm gaps between them providing huge field enhancement moreover these densely packed nanoparticles will result into maximum density of hotspots on the surface.

(ii) Electrostatic assembly. The layer by layer procedure works on the concept of self-assembly of layers of oppositely charged nanoparticles ultra-thin films. Layer by layer is a proven technique to fabricate organic, inorganic for hybrid nanomaterial substrates. A very popular of these techniques is Langmuir Blodgett (LB), which is used to deposit a functional layer of highly ordered nanoparticles. the process involves spreading of colloidal solution of nanoparticles onto water surface and a densely packed array is obtained by compressing the same by applying surface pressure [74]. The Langmuir Blodgett process provides dexterity tuning the enhancement factor for resonant wavelength by wearing the inter-particle distance by regulating the pressure applied on the surface. Once an active metal layer is obtained by layer by layer method then it can be transferred onto a temperature sensitive in polymer layer whose morphology is temperature dependent.

(iii) Template assembly using colloidal crystal. Colloidal crystals have been evinced as a cost effective and simplified technique to fabricate templated two dimensional Nano structures in comparison to lithographic methods for stop different templated colloidal techniques in wall "drop casting, spin coating, dip coating and electrophoretic deposition" techniques [21].

(iv) Nanoporous template assembly. The anodic Aluminium oxide laminates bearing well-arranged nano-pore arrays are used as template to fabricate two-dimensional metallic nanostructural arrays [75, 76]. The porous Aluminum oxide players have got inherited advantage of ability to manipulate 4 size, thickness of walls and in turn spacing between nanoparticles and their periodicity.

(b) Three Dimensional SERS Substrates. Three dimensional substrate display the highest sensitivity among all three types of SERS substrates, that too up to a level of single molecule [77, 78]. Best high sensitivity is obtained due to following reasons

(i) Higher probability of exciting laser to reach hotspots due to higher interaction between light and mobile nanoparticle clusters.

(ii) These moving nanoparticles have greater potential to incarcerate analytes in the small gaps.

The loose morphology of three dimensional Nano structures on templated substrate facilitates efficient interaction between incident excitation light and Nano structures. The kind of substrates have got substantial surface area to bind with and lights and come up with high concentration of hotspots within illuminated spot of excitation laser. These three dimensional solid States have got audit advantage of very high stability under ambient conditions. The three-dimensional metallic Nano structures may be obtained by either of the following two processes:

(i) Three dimensional templates are used to deposit active metal Nano structures and post the position of metal nanoparticles the three-dimensional templates are withdrawn to provide recurrent porous Nano structures.

(ii) In second method three-dimensional templates on left as it is, to strengthen the metallic Nano structures in three dimensional SERS substrates.

2.5.6 Spacing Between Nanoparticles

The SERS is influenced by distance between nanoparticles, now this is distance maybe:

(a) Between analyte and metal nanostructures or

(b) Mutual distance between contiguous metal Nano structures.

BJ Kennedy et.al. about relation between SERS intensity 'I' and distance between analyte and metal nanoparticles [29] in 1999 as follows:

$$\boldsymbol{I = \left(\frac{a+g}{a}\right)^{-10}} \qquad \textbf{.....2.7}$$

Where a= average size of nanoparticles contributing to electromagnetic field enhancement.

g= gap between analytes and metal surface.

It is imperative to emphasize on the fact that this phenomenon of electromagnetic field enhancement besides distance depends on geometrical characteristics like shape size and mutual orientation of Nano structures as already elaborated in previous subsections. Secondly spacing between active metal Nano structures must be appropriate for surface plasmon resonance to occur. if it is too large than those surface plasmon excitation may occur but resonance between surface plasmon may not appear and hence no significant enhancement is achieved. On the other hand if

the gap is too small then poor polarization of electromagnetic field may entail to lower enhancement factor.

2.6 ENHANCEMENT FACTOR CALCULATION

Enhancement factor is one of the vital factors in SERS phenomenon. Since magnitude of enhancement factor of SERS is a decisive criterion to interpret potential of SERS active substrate, therefore for a clear definition of SERS enhancement factor necessitates a clear procedure for its calculation. Application of different substrates mandates use of different method methodology for calculation of SERS enhancement factor. Commonly SERS enhancement factor is denoted by ratio of "SERS intensity per molecule within hotspot and Raman intensity per molecule in scattering volume".

$$\mathbf{EF} = \frac{I_{SERS}/N_{SERS}}{I_{Ref}/N_{Ref}} \qquad \textbf{.....2.8}$$

Where I_{SERS} and I_{Ref} = measured Raman intensities of the SERS and the reference samples.

N_{SERS} and N_{Ref} = the numbers of molecules on the surface of the bowtie and the reference sample.

The ratio of N_{SERS} and N_{Ref} may be approximated to

$$\frac{N_{SERS}}{N_{Ref}} = \frac{M_{SERS} \cdot Volume\ of\ liquid\ on\ SERS}{M_{Ref} \cdot Volume\ of\ liquid\ on\ reference} \qquad \textbf{..... 2.9}$$

$$\frac{N_{SERS}}{N_{Ref}} = \frac{M_{SERS} \cdot A_{Bowtie} \cdot h}{M_{Ref} \cdot A_{Ref} \cdot h} = \frac{M_{SERS} \cdot A_{Bowtie}}{M_{Ref} \cdot A_{Ref}} \qquad \textbf{..... 2.10}$$

where M_{SERS} and M_{Ref} are the molecular concentrations of the SERS and reference samples,

A_{Bowtie} = area of the bowties, and

A_{Ref} = exposure area of the laser beam on the reference sample, which is equal to the beam area.

Importantly, since in the bowtie the hotspot only exists within the gap area, the actual effective area is much smaller than the whole bowtie area and hence the corresponding EF at the gap is much larger than the calculated one.

It is known that enhancement factor is caused due to two major contributing mechanism; namely electromagnetic and chemical mechanism. The EM field enhancement takes place significantly at both incident frequency and Stokes frequency. Since Stokes Frequency Shift much lesser than the incident frequency the net electric field enhancement can be estimated to:

$$EF = \frac{|\mathbf{E}|^4}{|E_o|^4} \qquad \text{..... 2-1}$$

Where |E0| = magnitude of the incident electric field and

|E| = magnitude of the electric field in the vicinity of the plasmonic nanostructures.

The other contributor is the chemical enhancement, this happened due to the transfer of electrons between the molecules and metal nano-structures exchange electrons and it usually lies in between 10^1-10^3.From the above theory, it is clear that enhancement factor depends on the magnitude of E-filed enhancement achievable with the SERS substrates

2.7 APPLICATIONS OF PLASMONICS

In last few decades tremendous amount of work has been put in the field of surface enhanced Raman spectroscopy and it has observed remarkable evolution in manufacturing techniques of SERS substrates. This fact brings SERS spectroscopy ahead of other analytical tools to distinguish chemical and biological species. There are numerous applications of surface plasmon polariton demonstrated in sub wavelength optics; this may be categorized into following categories:

(a) As surface plasmon polariton waveguides
(b) As surface plasmon polariton sources
(c) In near field optics
(d) Surface enhanced Raman spectroscopy
(e) Data storage
(f) Solar cells
(g) Chemical sensors

(h) Biosensors

2.7.1 As Surface Plasmon Polariton Waveguides

Quinten et.al. brought out concept of continuous chain of silver nanoparticles of spherical shape acting as optical waveguide **6-2**. Mie calculations were used to estimate light propagation through elongated linear chain of uniformly spaced silver nano-spheres. The illumination of first particle in the chain with polarized light having polarization perpendicular and parallel to axis of nano-spheres chain leads to two phenomena:

(a) The light polarized parallel to axis is efficiently guided through the chain with constant decay of intensity.

(b) The light polarized perpendicular to the axis of chain heavily deteriorates.

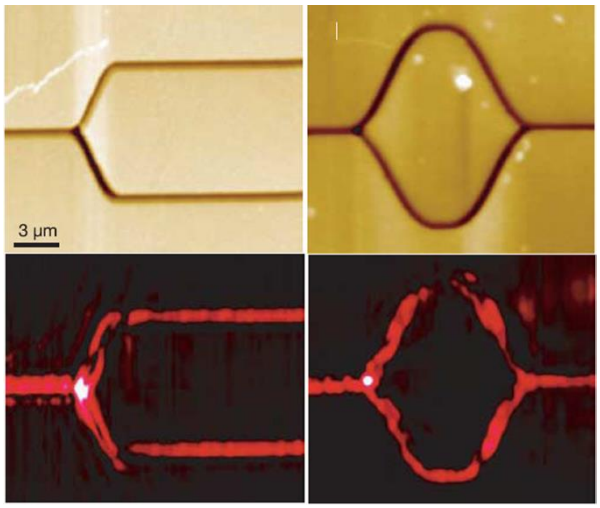

Figure 2.14 Plasmonic Y-splitter and Mach–Zehnder (MZ) interferometer. (a) (b) Topographical images and (c) (d) Scanning Near-field Optical Microscopy images [53].

This is observed due to the fact that surface plasmon polariton obtained the oscillations energy by pairing of the illumination due to incident light at parallel polarization to the chain axis, howbeit other spares are not able to pair up surface plasmon polariton for illumination by incident light with perpendicular polarization. Weeber et.al. have proposed propagation of light through nanowires laid on transparent substrates [55]. Zhang et.al. have introduced new proposal of integrating dielectric

waveguides with surface plasmon polaritons [56]. Ebbesen and co-workers fabricated waveguide structures of depth 1.2 micrometer in 1.8 micrometer gold film on silicon substrate.

2.7.2 As Surface Plasmon Polariton Sources

Regular Bull's-Eye pattern was proposed by Lezec et.al. at egress of only hole in a metal film providing a highly focused beam with the very small double angle [79]**.** A cylindrical structure with radius 125 nm is made using a thin silver film. Then concentric grooves which are 60 nm deep and have periodicity of 500 nm gap in between two consecutive grooves. These grooves patterned using to discrete disengaged 300 and thick silver films catering for bullseye patterns for input and output sides of the nano-road. If one who is crafted in the thin suspended syllabus in the calculations establish that light escaping through hole is completely distracted into hemispherical pattern stop now the bullseye is applied on the input side of the whole and then at the exit side stop when bullseye is placed on the input side of the word the light transmission is enhanced at particular wavelength governed by periodicity of groups due to surface plasmon polariton resonating or matching with corrugation period, but the light at the output is still diffracted akin to hole without any e bullseye pattern placed at input. When a similar bullseye pattern is placed at exit of the cylinder the addressing light intensity strongly depends on the angle of diffraction.The pattern of light emerging and exit of Nano silver cylinder with bullseye corrugated pattern on both inlet and outlet has emerged apparently as a narrow beam with divergence angle of $\pm 3^0$ from the axis of the beam. Does a coextensive circular corrugated patterned silver film at inlet and outlet of a silver cylinder can be utilized as a surface plasmon polariton source of highly convergent and directional light with very high efficiency. With similar principles Oulton and Zhang et.al. [80] have proposed an ultra-miniaturized lasers capable of generating coherent electromagnetic fields.

2.7.3 Near Field Optical Analysis.

Conventional microscopes are limited by their highest resolution achieved up to a factor of half wave length, to facilitate operation on small scale resolutions of the

order of nm scanning near field optical microscope as an Scanning Near-field Optical Microscopy is used.

The most crucial component of SNOM is the proverb which is prepared by making a small hole on tapered optical fiber which is coated with metal. The constraint for efficiency of SNOM probe is limited amount of light from small objects collected by prob. Ketterson et.al. came up with a solution for this problem, they made use of tungsten filament as probe tip. A 50 nm thick film was deposited on a microscope glass. The surface plasmon polariton are excited on surface of silver film with in Kretschmann Total Internal Refraction setup. This whole arrangement results localized enhanced electromagnetic fields on each of the surface irregularities due to surface plasmon polariton which scatter the field and a conical radiation is obtained. Thus minute scattering surface plasmon polariton, acts like a probe and overcome drawbacks of hole in the probe resulting into improvised light collection efficiency.

2.7.4 Surface enhanced Raman spectroscopy

If surface plasmon polaritons find their most extensive application in any field then it is surface enhanced Raman spectroscopy. The surface enhanced Raman spectroscopy enhancement may have two contributing factors electromagnetic enhancement and chemical enhancement. However the most significant contributor is electromagnetic enhancement which is attributable to surface plasmon polariton and localized surface plasmon excitation. Raman scattering phenomena for the detection of single molecule have been studied by Kartin Kneipp et.al. [81]. Enhancement factors as large as 10^{14} to 10^{15} was obtained from a single molecule deposited on the surface of silver film. Most of this enhancement originates from junctions of nanoparticles because of exceedingly enhanced fields due to plasmonic phenomena. A Stokes shift towards greater wavelength than incident light is observed due to emission of light with largest wavelength from these nano-junctions, which are called as hotspots. There have been increasing efforts towards achieving better enhancement factors, one of these works by Xu, Zhang et.al. used periodic array of gold Nano wires implanted in porous alumina membrane to illustrate extremely sensitive recognition of organic molecules by SERS phenomenon [82]. Usually in SERS detection procedures, the detection of light is done

from same spot as where incident laser light is focused on to i.e. hotspot of SERS on metallic nanostructure. However, this approach is not suitable for few applications, specifically when working with living organisms, where cells may be destroyed by high power generated by incident laser light. Fang, Xu et.al. have come up with a solution for this by demonstrating large SERS enhancements achieved at junction of silver nanowires and adjoining silver nanoparticles [83]. With this substantial SERS enhancement detection can be performed at a point away from excitation source or hotspot.

2.7.5 Data storage

Information on concentration of more than one terabit per cubic cm can be e achieved by multiplexed optical recording which facilitates storing numerous independently addressable Nano patterns in a particular recording volume. There are five dimensions in which in optical nanoparticle may be addressed:

(a) Polarization

(b) Wavelength and

(c) Three dimensional space

Such recording mediums are still to be developed which process high discriminatory properties towards all five dimensions mentioned above semi column this poses challenge for instilling multiplexing in recording of information. in recent past localized surface plasmon resonance shown by gold nano-rods has been exploited by Zijstra [84] for actual five dimensional recording. The concept of recording in in five dimensions may be understood with the help of fig. 2.15. The specimen comprises of multiple layers stacked one above other for stop this layers are 1 micrometer thick recording layers and 10 micrometer thick transparent separating layers arranged alternate to each other in two dimensions of polarization and wavelength.

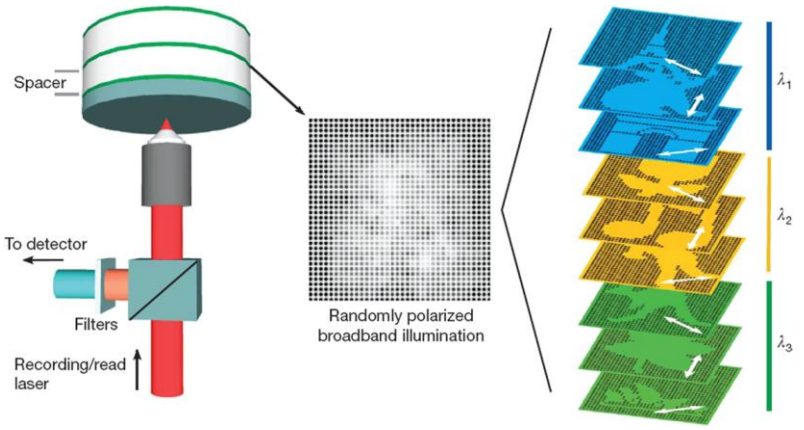

Figure 2.15 SPP as data storage. Sample structure and patterning. Left: the sample consists of thin recording layers deposited with gold nanorods; these recording layers were spaced by a transparent separator, multiple images were patterned using different wavelengths (λ1−3) and polarizations of the recording laser. Middle: when illuminated with un-polarized broadband illumination; a convolution of all patterns will be observed on the detector. Right: when the right polarization and wavelength are chosen; the patterns can be read out individually [53].

To perceive successful five dimensional encryption of recording substrate following vital factors must be met [53]:

(a) Material must be arranged in all five dimensions while writing and reading.

(b) Recording technique must be capable of providing multiple channels for recording in individual dimension.

(c) Possess stability in ambient environmental condition and must be readable without damaging recorded data.

The Zijstra et.al. have suggested use of surface plasmon polariton gold nano-rods based recording substrate. These nano-rods are exceptionally sensitive towards polarization and wavelength once five dimensional encryption of nano-rods is complete the reading may be performed by photo-thermal restructuring principle and twin photo eminence detection.

2.7.6 Solar Cells

These are also known as photovoltaic cells. Hanuman hand increased thickness will facilitate absorption of incident light but on the contrary decreased thickness will provide higher efficiency of conversion of light into electric energy. for ordinary cell structure and the absorption is decreased entailing to lesser excitation of charge carriers and photocurrent generation for thickness of the order of nm, thus limiting conversion efficiency. Therefore it is highly desired to develop a technology which provides better tradeoff between light absorbed and light trap for conversion to electrical energy. It is observed that thin films with metal nanostructure deposited are capable of incarcerating and escorting sunlight incident on it, to sub wavelength thick absorbing layer by phenomena of SPP excitation. A tremendous solar cell efficiency enhancement of light to electricity conversion was observed on the position of metal nanostructures [53]. On deposition of silver, gold and copper nanostructures photovoltaic current was amplified by a factor of 1.3, 2.2 and 2.7 respectively [85].

2.7.7 Biological and chemical sensors

A device capable of identifying chemical attributes of a sample and converting it into electrical data is known as chemical sensor. The similar properties of the sensor may be used to analyze and detect biological samples as well. The response of chemical sensor deviates from normal neutral value when chemical or biological sample to be detected comes into its vicinity. As already covered in section 2.9, dielectric constant of environment plays an important role in SERS phenomena. Addition of chemical in close proximity of the sensor will change refractive index of its surrounding and will facilitate its detection. In addition to this if appropriately selected ligand is deposited on SERS active metallic layer, will further enhance chances of detection at nanoscale.

2.8 FINITE DIFFERENCE TIME DOMAIN (FDTD)

Finite difference time domain is a time-domain method, which is capable of performing analysis over a wide frequency band within a single simulation, while treating nonlinear aspects of material in their actual way of existence.

The FDTD method is related to the family of general grid-based differential numerical modelling methods also known as finite difference methods. The time-dependent Maxwell's equations are broken and simplified using central-difference approximations to partial derivatives in time and space. The finite-difference equations obtained are then solved by simulator using a leapfrog manner. The electric field vector and the magnetic field vector components of a spatial volume are solved individually at alternate time intervals and this process is repeated iteratively till the time the desired transient response or steady-state electromagnetic field behaviour is completely developed.

In process of implementation of FDTD solution of Maxwell's equations, firstly a computational domain is required to be established. This computational domain may be defined as a physical region which will undergo simulations. In the computational domain the electric and magnetic fields are resolved at all the points. The complete volume of the computational domain is divided into small cells for which material must be defined. Usually, the material is metal, dielectric or free-space (air). Any material for which permeability, permittivity, and conductivity are defined can be used for simulations.

As FDTD is a time-domain technique with a single simulation, the response of the system over a wide range of frequencies canbe obtained especially when a broadband source like a Gaussian pulse source is used. Thus it makes it suitable for analysis of systems whose resonant frequencies are not known, or whenever it is required to obtain a broadband response of a system.

CHAPTER 3

SPHERICAL AND ELLIPSOIDAL DIMERS

3.1 AIM

This project aims at designing a structure which can enhance the electromagnetic field at a point, called hotspot, such that when it interacts with an analyte,i.e. sample to be detected or examined, it facilitates its detection by enhancing the electromagnetic field scattered from the analyte. For this purpose many structures are considered and examined for their efficacy of electric field magnification. Firstly spherical dimers were considered and then ellipsoidal dimers were studied. Thereafter, bowtie structures were studied. To summarize different nano-structures considered and implemented in this course of action are as follows:

(a) Spherical Dimers

(b) Ellipsoidal Dimers

(c) Bowties

(d) Symmetric array of triangular shaped bowtie and different combinations made by varying the length of bowtie and keeping its width constant.

(e) Symmetric array of triangular shaped bowtie and different combinations obtained by varying the width of bowtie and keeping its length constant.

(f) Array of asymmetric triangular bowtie with constant length

(g) Array of symmetric triangular bowtie with sides stacked with each other.

(h) Movement of one triangular nanostructure of bowtie with the triangular nanostructure having V groove in it.

(i) Trident vs a triangular nano-plate.

In subsequent paragraphs one by one these structures and results obtained from them will be elaborated.

3.2 SPHERICAL DIMER

In this a dimer of two spheres with 20 nm diameter is considered. This is the initial structure to analyze the enhancement factor of a dimer. Before analyzing this structure itself it was decided to study the effect of different simulation parameters simulation parameters on the enhancement factor, so that the best simulation parameters simulation parameters are obtained which may be treated as standard parameters for rest of the structures to be considered in this work. Before moving ahead it will appropriate to note the parameters which are kept constant during analysis of spherical dimer, these are:

(a) Structures understudy is symmetric about (0,0,0) in XY plane of Cartesian x,y,z coordinates.

(b) Geometric features are varied in XY plane

Further, to confirm optimal simulation parameters the convergence study is performed by varying two factors:

(c) Effect of perfectly matched layer (PML).

(d) Effect of mesh size.

3.2.1 Effect of Perfectly Matched Layers (PML)

A perfectly matched layer is an imaginary absorbing layer used for simulation of wave propagation equations, it is meant to curtail a particular region for computational purposes and simulate a boundary less system. It is very useful in numerical techniques like finite difference time domain (FDTD). The perfectly matched layers are varied from 8 to 14, without varying any other physical parameter and its effect was analysed on the electric field enhancement. The observations made in due course are mentioned in table 3.1.

Sl. No.	No. of PML	Electric Filed Intensity Enhancement Factor	Resonant Wavelength (nm)
1.	8	4.64	534.483
2.	10	4	534.483
3.	12	4.03	534.483
4.	14	4.11	534.483

Table 3.1 Results of variation of perfectly matched layer (PML) in case of spherical dimer.

The results obtained and shown in table 3.1 are elaborated in following fig. 3.1.

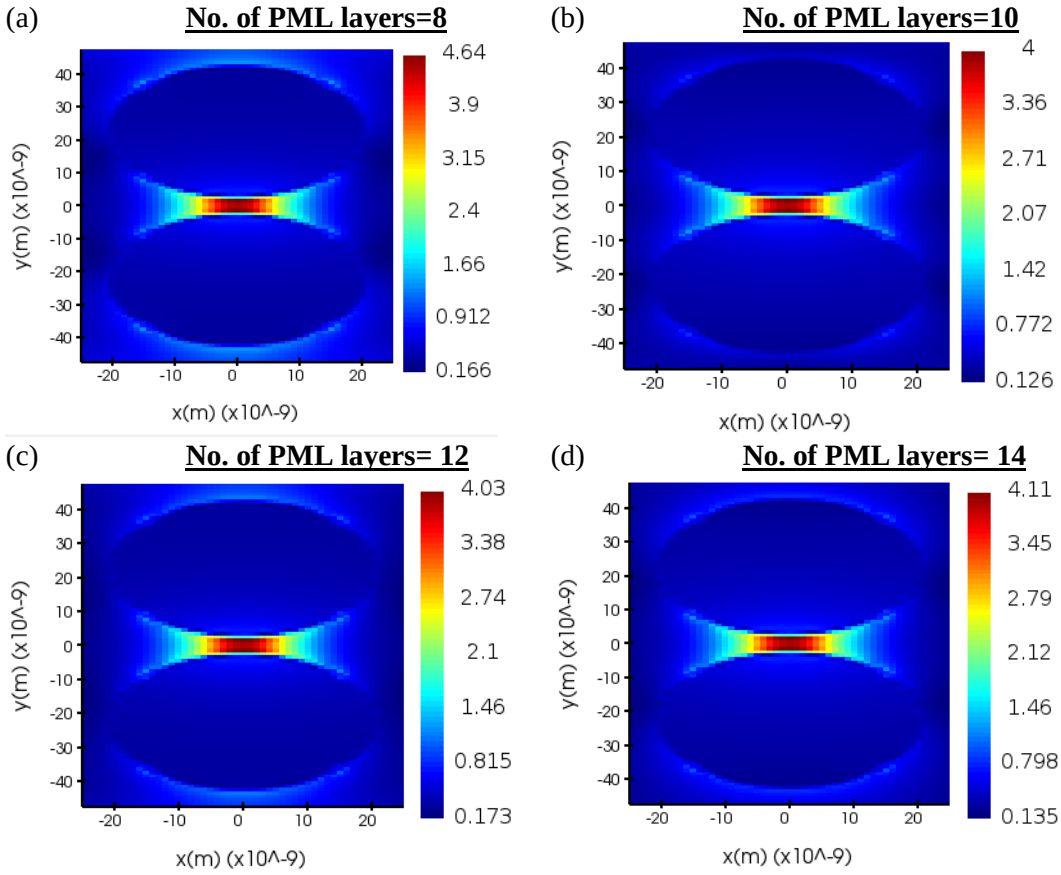

Figure 3.1 Results of variation of number of perfectly matched layer (PML) layers in case of spherical nanoparticle dimers

It was found that enhancement factor did not show any significant change due to variation of number of perfectly matched layers. From the table above it may be noticed that intensity first decreased and then increased fractionally with increase in

number of PML, but it remained lesser than the intensity obtained with eight perfectly matched layers (PML). However, increasing the number of perfectly matched layers significantly increased the processing time. So we can reach to a conclusion to adhere with minimum number of PML providing maximum enhancement. This process facilitated to finalize the optimal number of PML layers that is it. Thus PML will remain constant for all future considerations throughout this work and will be kept equal to 8.

3.2.2 Effect of Mesh Size

Before we go ahead with variation of mesh size it is better to understand what exactly the mesh is and how it affects the simulation region. The smaller is the mesh size, the higher will be the resolution of simulation results obtained and more will be processing time of that particular problem. This higher resolution with smaller mesh size will provide more accurate results about intensity of light in particular regions. For this we observe the highest intensity of light obtained at the hotspot and keep a check on the value of mesh size at which this intensity becomes unchanged for any further reduction in it. For considering the size of mesh we require some reference value which relates it to the nano-structures being observed, this is the smallest gap in between the nano-structures under consideration. In this work it will be the gap between the closest edges of the dimer, g = 5nm, therefore the mesh size is varied from g to g/8. The observations made in due course are as tabulated below:

Sl. No.	Mesh Size	Electric Filed Intensity Enhancement Factor	Resonant Wavelength
1.	g/2	3.8	534.483
2.	g/3	3.94	534.483
3.	g/4	4.34	534.483
4.	g/5	4.64	534.483
5.	g/6	4.64	534.483
6.	g/7	4.64	534.483
7.	g/8	4.64	534.483

Table 3.2 Results of variation of mesh size in case of spherical nanoparticle dimers

It was observed that as the mesh size was decreased from g (5 nm) to g/8 (0.625 nm) the enhancement factor became constant after g/5 i.e. 1 nm. From the table above it may be noted that intensity of light at hotspot increases with decrease in size and

becomes constant at mesh size equal to and less than 1 nm. The observations made by varying the mesh size are elaborated in fig. 3.2:

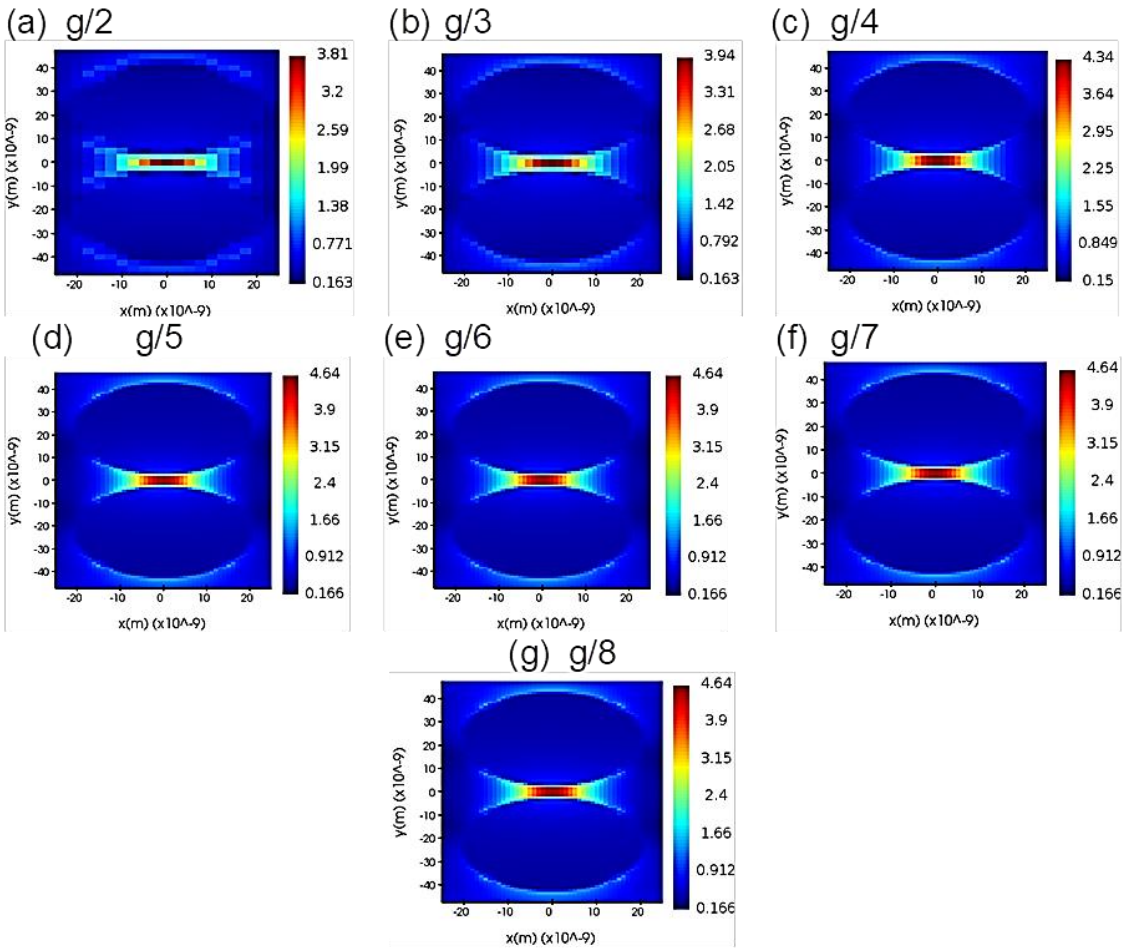

Figure 3.2 Results of variation of mesh size in case of spherical nanoparticle dimers with mesh size (a) m = g/2, (b) m = g/3, (c) m = g/4, (d) m = g/5, (e) m = g/6, (f) m = g/7 and (g) m = g/8, where g is smallest gap between two spherical nanostructures.

With this we can conclude that further decrease in mesh size will not give any advantage in respect of resolution or accuracy. Therefore an optimal mesh size was obtained at g/5 equal to 1 nm. This optimal mesh size of 1 nm will be treated as standard mesh size in all the future considerations in this work.

After obtaining the standard simulation parameters to be considered in rest of the work, changes in structural parameters will be analyzed. The first step towards structural change would be to change the dimensions of the nanostructures considered

(i.e. spherical nanoparticles or ellipsoidal nanoparticles), by changing one of the axis of the spheres to make them ellipsoids. Different analysis is done for ellipsoids and results obtained are covered in subsequent sections.

3.3 ELLIPSOIDAL DIMER

In this section two ellipsoids of similar shape are considered to be placed at 5 nm distance from each other. Initially only two nano ellipsoids are considered followed by an periodic array of the same, however to analyze the effect of SERS active material as substrate and surroundings, a base and walls on either side of the nano-structure are considered in subsequent structural configurations.

3.3.1 Structural details

Ellipsoidal nanostructure under consideration has following dimensions:

(a) Major axis of the ellipsoid= 80 nm.

(b) Minor axis of the ellipsoid = 40 nm.

(c) Gap between the two ellipsoids is 5 nm.

With these basic structural details, a total of 6 different configurations will be analyzed for enhancement of electric field intensity. These 6 structural arrangements are as follows:

(a) Two ellipsoids with their major axis aligned to each other.

(b) Periodic array of two ellipsoids with their major axis aligned.

(c) Ellipsoids with 60 nm walls on either side.

(d) Periodic array of two ellipsoids with grating of 60 nm wall thickness 10 nm away from ellipsoid.

(e) Periodic array of two ellipsoid with grating of 40 nm wall thickness 5nm away from ellipsoid.

(f) Array of two ellipsoid array with minor axis aligned with 60nm wall 10nm away from ellipsoid.

3.3.2 Two ellipsoids with their major axis aligned to each other

In this structural arrangement two ellipsoids were so arranged such that their major axis aligned with each other, to create a dimer structure with a gap of 5 nm in between vertices two ellipsoids.

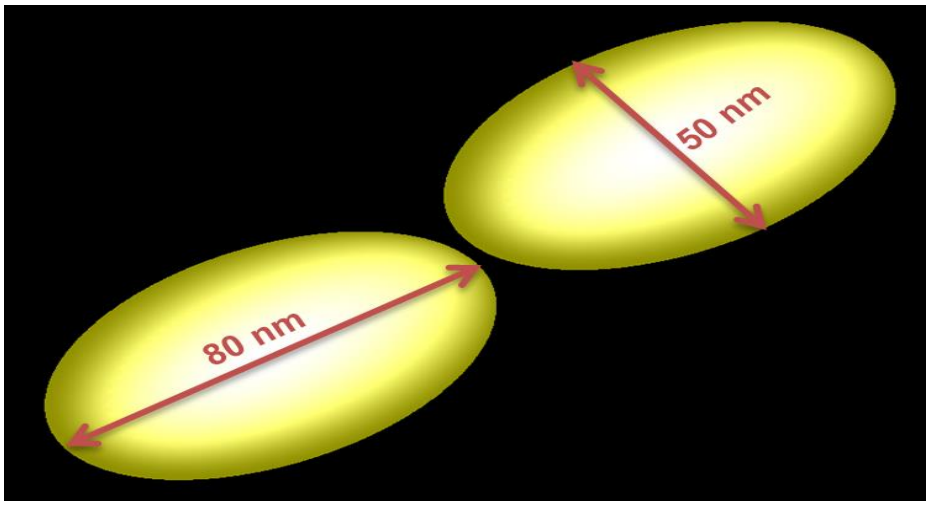

Figure 3.3 Ellipsoidal dimer nanostructure with major axis of ellipsoids aligned

These were analyzed for any difference in respect to enhancement of electric field intensity at the hotspot as compared to the spherical dimer.

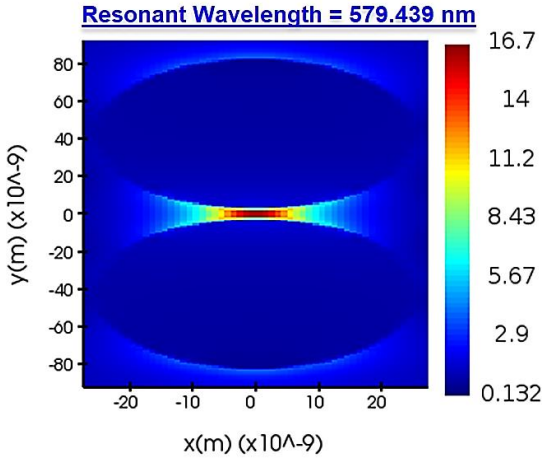

Figure 3.4 Electric field enhancement produced by ellipsoidal dimer nanostructure with major axis of ellipsoids aligned

It was observed that there was a significant increase in enhancement of electric field intensity at the hotspot (16.7) as compared to dimer with spherical nano-structures (4.64). The maximum enhancement of the electric field obtained was16.7 at resonant wavelength of 579 nm. This is mainly because of crowding of E-field lines at the vertex of the nano-ellipsoid.

3.3.3 Array of two ellipsoids with their major axis aligned

This structural arrangement is similar to the two ellipsoids considered in previous subsection but the difference is that it is iterated in both X and Y directions with distance between two consecutive ellipsoids equal to 5 nm, with their major axis aligned with Y direction and minor axis aligned with X direction. It was seen that the maximum enhancement of electric field intensity obtained was 19.4 at resonance wavelength of 673.913 nm. This will be more clear with the help of fig. 3.5.

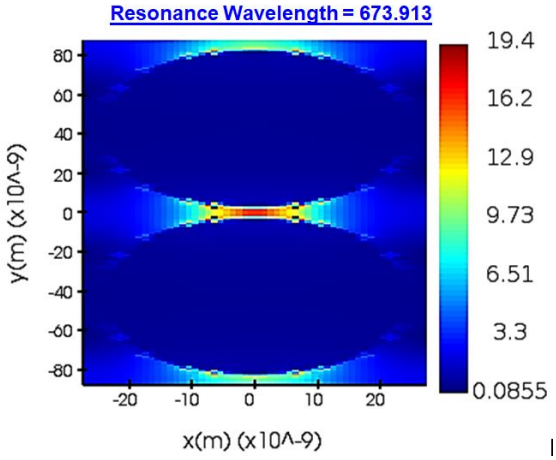

Figure 3.5 Array of two ellipsoids with their major axis aligned.

3.3.4 Ellipsoidal dimer with 60 nm wide nano-gratings on either side

In the previous subsection it was seen that there was an improvement of electric field intensity in case of an array of similar structures as compared to individual nano-structures. In this section ellipsoidal nano-structure with two walls on either side is considered. This nano-grating will be 55 nm long and will be 60 nm wide with thickness of 50 nm. Also there is a 50 nm thick substrate which lies underneath all the four structures (two walls and two ellipsoids). The structural details may be easily understood with the help of the following fig. 3.6.

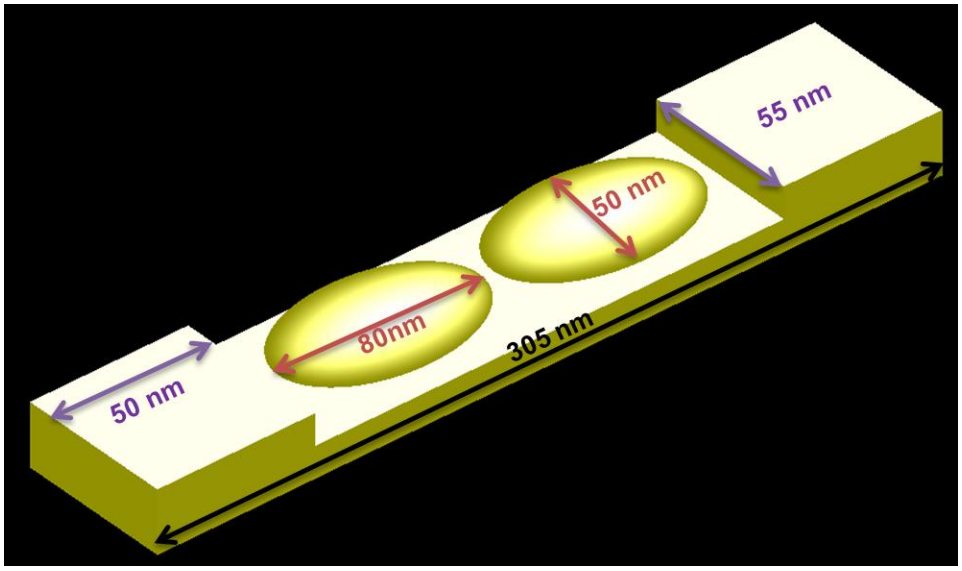

Figure 3.6 Ellipsoidal dimer nanostructure between 60 nm wide nano-gratings.

The maximum enhancement of electric field intensity obtained in this case was 30.3 at resonance wavelength of 673 nm.

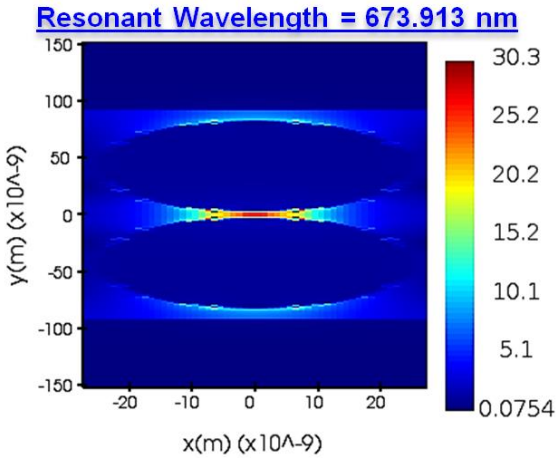

Figure 3.7 Electric field enhancement produced by ellipsoidal dimer with 60 nm grating wall on either side

3.3.5 Array of two ellipsoids in between periodic nano-gratings (60 nm wide at 10 nm from nano-ellipsoid)

In a sequence of progress to previous subsection in which dimer two ellipsoid is considered with two 60 nm thick walls on either side, in this subsection an array of similar structures is considered. This array of dimers of two nano-ellipsoids iterates in x-y plane with 60 nm thick nano-grating in between two consecutive nano-dimers in y direction. This nano-grating is 10 nm away from ellipsoidal nano-structure.

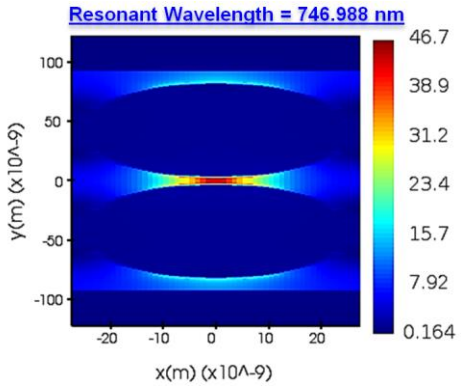

Figure 3.8 Electric field enhancement produced by array of two ellipsoids in between periodic nano-gratings (60 nm wide at 10 nm from nano-ellipsoid).

It was observed that the maximum enhancement of electric field intensity is 46.7 obtained at a resonant frequency of 746 nm, the same is depicted in fig. 3.8.

3.3.6 Array of two ellipsoids in between periodic nano-gratings (60 nm wide at 5 nm from nano-ellipsoid)

With an aim to understand the effect of grating in between the nano-structures, it was decided to move the grating wall closer to the nano-structure, such that the distance between the nano-dimers and the wall is equal to the minimum gap in between the elements of nano-structure i.e. 5 nm.

It was observed that such structural arrangement provided an enhancement of electric field intensity of 48.7 at a resonant wavelength of 805 nm. It may be noted that with decrease in gap between nano-grating and nano-ellipsoid, there is a minor increment in electric field intensity and a red shift in the resonant wavelength in this case.

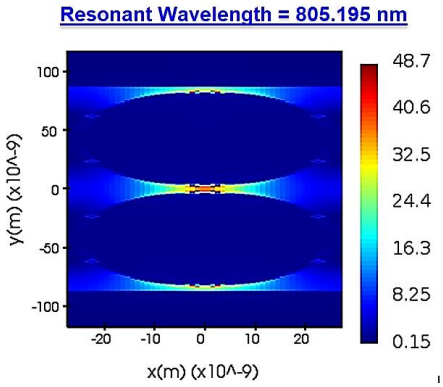

Figure 3.9 Electric field enhancement produced by array of two ellipsoids in between periodic nano-gratings (60 nm wide at 5 nm from nano-ellipsoid).

So it is concluded that a fairly good distance between the nanostructure and grating walls is 10 nm. This distance of 10 nm will be treated as a standard distance between grating walls and nanostructures for all the future nanostructural configurations in this work.

3.3.7 Array of two nano-ellipsoids (with minor axis aligned) in between periodic nano-gratings (60 nm wide at 10 nm from nano-ellipsoid)

Having considered all the structural arrangements of ellipsoids and grating walls and their arrays, next the alignment of minor of the ellipsoids may be considered

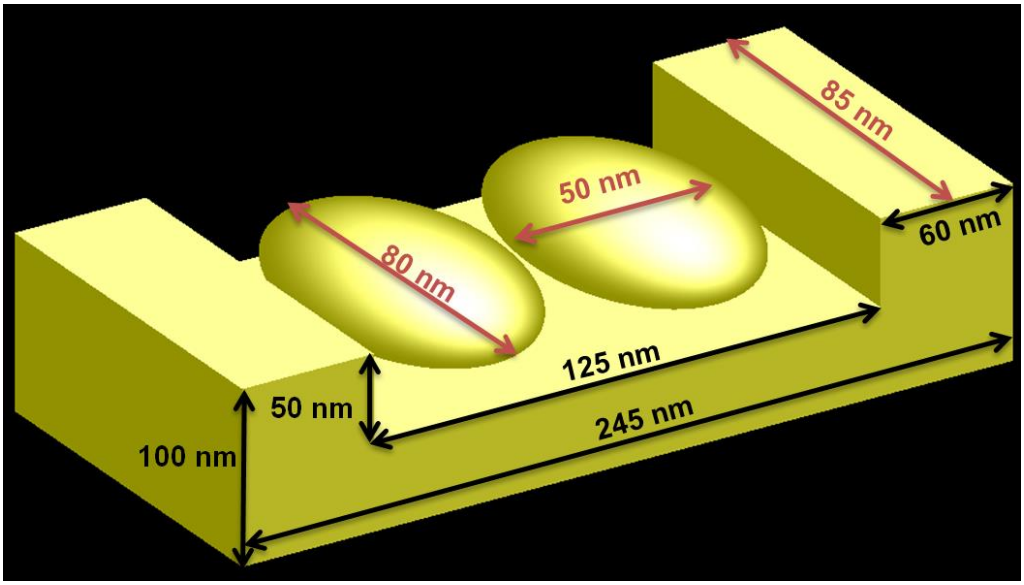

Figure 3.10 Array of two ellipsoid (Minor axis aligned) array with 60nm thick grating wall 10nm away from ellipsoid

. In this subsection the nano-ellipsoids will be positioned such that their minor axes are aligned to each other and in turn with y-axis and rest of the structural parameters in respect of gap between the ellipsoids, thickness of nano-grating etc. are same as were in previous subsection. The aim of considering this structural arrangement was to analyze the possibility of increased enhancement of electric field intensity at hotspot due to reduced overall distance between the nano-gratings and longer nano-ellipsoid dimensions to collect maximum electric field from the source.

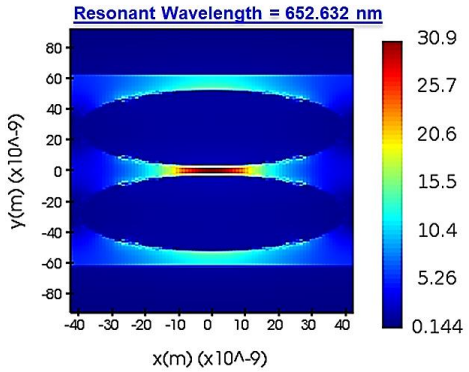

Figure 3.11 Electric field enhancement produced by array of two ellipsoid (Minor axis aligned) array with 60nm thick grating wall 10nm away from ellipsoid

A dip in enhancement of electric field was observed in this structural arrangement such that the maximum enhanced electric field of 21.9 was obtained at a resonant wavelength of 613 nm. This is expected because the grating wall confinement is absent in this direction.

3.3.8 Results and observations

In this section two ellipsoids were arranged in different ways to make a dimer nanostructure. The six ellipsoidal dimer nanostructures analyzed in this section and results observed can be summarized in tabular form as in table 3.3:

S.no.	Configuration	Major axis	Minor axis	Electric field intensity enhancement	Resonant wavelength (nm)
1.	Two ellipsoids with their major axis aligned to each other.	80	40	16.7	579.439
2.	Array of two ellipsoids with their major axis aligned.	80	40	19.4	673.913
3.	Ellipsoids with 60 nm walls on either side.	80	40	30.9	673.913
4.	Array of two ellipsoids (Major axis aligned) with grating of 60 nm wall thickness 10 nm away from ellipsoid	80	40	46.7	746.988

S.no.	Configuration	Major axis	Minor axis	Electric field intensity enhancement	Resonant wavelength (nm)
5.	Array of two ellipsoids (Major axis aligned) with grating of 40 nm wall thickness 5nm away from ellipsoid	80	40	48.7	805.195
6.	Array of two ellipsoids (Minor axis aligned) array 21.5 nm width with 60nm wall 10nm away from ellipsoid	40	21.5	21.9	613.861

Table 3.3 Comparative analysis of ellipsoidal dimer nanostructures

From above table it maybe concluded that for ellipsoidal nanoparticle dimers, the maximum electric field enhancement of 48.7 at resonant wavelength of 805.195 nm was provided by array of two ellipsoids with major axis aligned with each other places 5 nm away and we enclosed in 40nm grating wall on either sides spaced 5 nm from ellipsoid nanostructure. Another ellipsoidal configuration which was very close to it was an array of two ellipsoids (Major axis aligned) with 60 nm wide nano-grating 10 nm away from ellipsoid providing and electric field intensity and harassment of 46.7 at a resonant wavelength of 746.988 nm. The enhancement factor for all six configurations are plotted in graph 3.1.

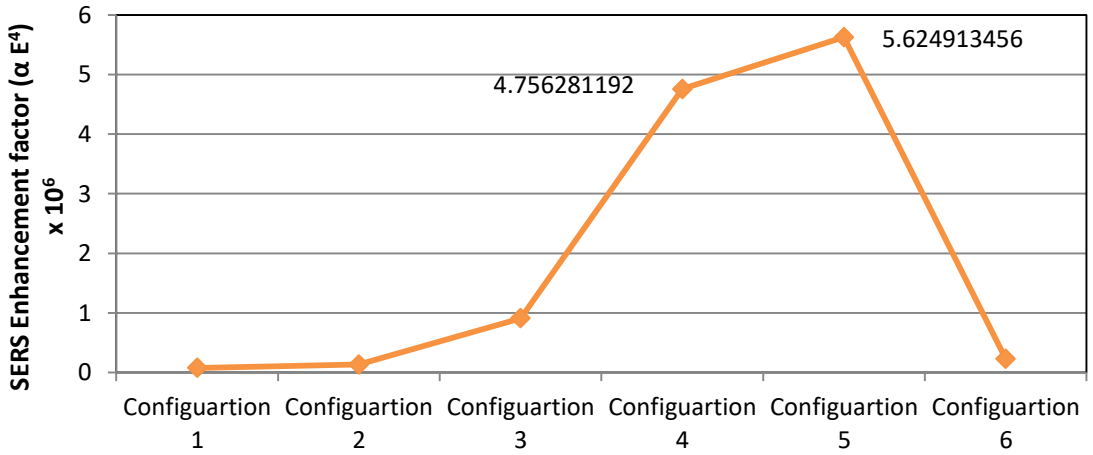

Figure 3.12 Graphical representation of Enhancement Factor obtained from different ellipsoidal nano-dimer structural configurations.

From fig. 3.12 it may be observed that configuration-4 with nano-grating at 10 nm gap from nano-dimer and configuration-5 with nano-grating at 5 nm gap from nano-dimer, produced the best results. The later configuration is quite close to the earlier configuration in respect of electric field intensity enhancement but is much easier to fabricate on large scale due to larger dimensions and gap between the nanostructures and nano-grating, therefore it will be treated as the standard configuration for rest of the nano-structural configurations considered in this work.

CHAPTER 4

TRIANGULAR SHAPED BOWTIE NANOSTRUCTURES

In this chapter bowtie nanostructures are analyzed. The two sides of bowtie are geometrically similar and equal in dimension in section 4.1 and 4.2, making them symmetric bowtie while in section 4.3 the two sides of the bowtie are different resulting into asymmetric bowtie. These simulations are being carried out. These simulations were carried out in following three parts to assess the variation of enhancement factor by varying the physical dimensions of the bowtie:

(a) Firstly the symmetry of bowtie is maintained by varying vertex angles ($\theta1 = \theta2$) at edges of bowtie nanostructures facing each other such that width of bowtie proportionately varies (($h1 = h2$) α ($\theta1 = \theta2$)), refer Fig. 4.1.

(b) Secondly the symmetry of bowtie is maintained by varying vertex angles ($\theta1 = \theta2$) at edges of bowtie nanostructures facing each other such that length of bowtie proportionately varies [($a = b$) α ($\theta1 = \theta2$) and ($h1 = h2 = 43.3$ nm)], refer Fig. 4.8.

(c) Thirdly asymmetric bowtie was considered, by varying vertex angles ($\theta1 \neq \theta2$) at edges of bowtie nanostructures facing each other such that length of bowtie proportionately varies [($a \alpha \theta1$) and ($b \alpha \theta2$) and ($h1 = h2 = 43.3$ nm)] but width remains constant, refer Fig. 4.11.

These three simulations may be summarized in Table 4.1 Refer Fig. 4.1:

Sl. No.	Simulation	Base length	Height	Vertex angle of bowtie
1	symmetric	a=b, constant	h1=h2, variable	$\theta1=\theta2$, variable
2	symmetric	a=b, variable	h1=h2, constant	$\theta1=\theta2$, variable
3	asymmetric	$a\neq b$, variable	h1=h2, constant	$\theta1\neq\theta2$, variable

Table 4.1 Three types of triangular bowtie nanostructure analyzed.

4.1 ARRAY OF SYMMETRIC TRIANGULAR BOWTIE NANO STRUCTURE WITH VARIABLE WIDTH

As covered in previous section in this part of simulation the bowtie is kept symmetric by keeping both the nanostructures of the bowtie similar to each other and equal in dimensions. The two nanostructures of the bowtie are kept at standard minimum distance of 5 nm. In this part of simulation length of the bowtie kept constant and the width is varied while varying the vertex angles of the two triangular nanostructures of the bowtie. in reference to Fig. 4.1 the dimensions 'a' and 'b' are kept constant and equal to 50 nm for all the values of θ_1 and θ_2 and the dimensions h_1 and h_2 are varied in proportion to angle θ_1 and θ_2, such that $(h_1 = h_2)\ \alpha\ (\theta_1 = \theta_2)$.

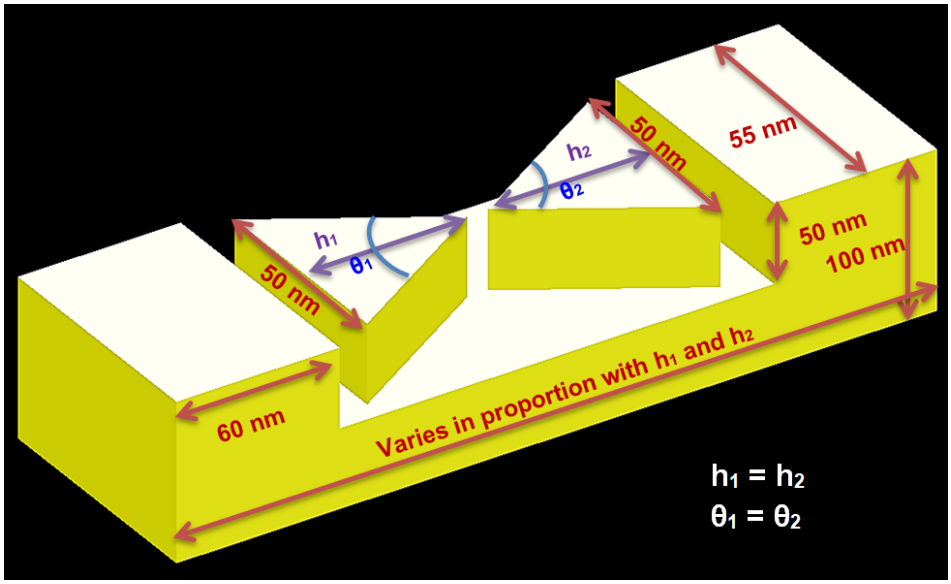

Figure 4.1 Symmetric Triangular Bowtie Nano Structure with Base of Triangle Constant (equal to 50 nm).

4.1.1 Observations

Different structural configurations of the symmetric bowtie have been studied for the enhancement of electric field intensity. The first and foremost observation made was that there is a hotspot created between the closer edges of two triangular nanostructures of the bowtie facing each other. Now the next step was to vary the structure of the bowtie to analyze whether it makes any difference to the enhancement factor or not. For this purpose the nanostructure was varied such that the length of the

nano-bowtie is kept constant (a = b = 50 nm) and width is varied in proportion to the vertex angle $\theta_1 = \theta_2$, i.e.

(a) a=b=50 nm

(b) $\theta_1 = \theta_2$ =20°, 30°, 40°, 50°, 60°

(c) $h_1 = h_2$; varied in proportion with angle θ1 and θ2 respectively

Observations made from these nanostructures are covered in following paragraphs.

4.1.2 Symmetric Bowtie with Vertex Angles $\theta_1 = \theta_2$=60°

In this configuration both the nanostructures of the bowtie nanostructure are made equilateral triangles with all the vertex angles equal to 60° and all sides of a triangular structure are equal to 50 nm in turn providing dimensions h_1 and h_2 equal to 43.3 nm. It was observed that maximum enhancement of electric field intensity obtained for this arrangement was 48.5 and an enhancement factor of 5.4×10^6 at a resonant wavelength of 696.629 nm.

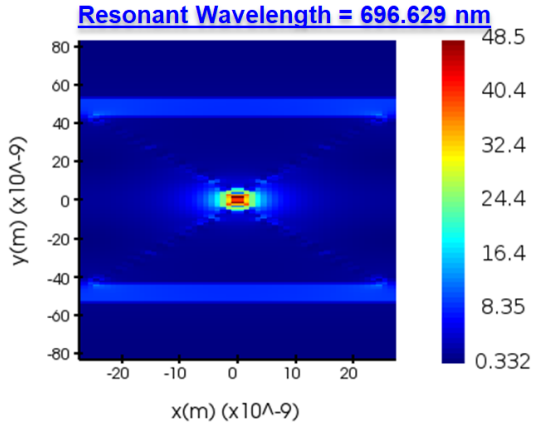

Figure 4.2 Electric field enhancement produced by Array of bowtie with Vertex Angles (θ1 = θ2=60°) of the Triangular Nanostructures.

4.1.3 Symmetric Bowtie with Vertex Angles $\theta_1 = \theta_2$ =50°

The parameters which were mentioned in previous subsection are maintained for this structural arrangement too; the only difference was that the vertex angles of both

triangular nanostructures of bowtie were reduced to 50°. This resulted in increase in width of the bowtie as compared to the 60° triangular bowtie, as each of the triangular nanostructures of the bowtie was elongated from 43.3 nm to 53.6 nm. This moved the nano-gratings away from each other by 20.6 nm. This structural configuration provided maximum enhancement of electric field as 73.7 and an enhancement factor of $2.9x10^7$ at resonance wavelength of 837.838 nm.

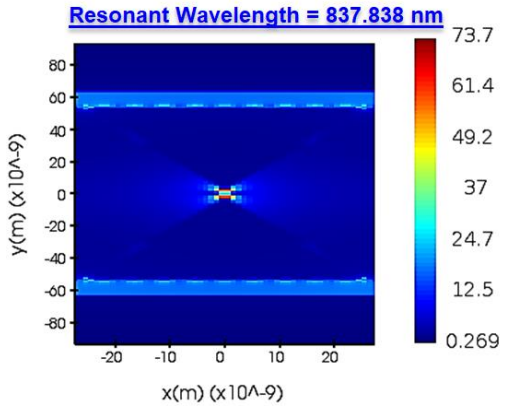

Figure 4.3 Electric field enhancement produced by Array of bowtie with Vertex Angles (θ1 = θ2=50°) of the Triangular Nanostructures.

4.1.4 Bowtie with Vertex Angles ($\theta_1 = \theta_2$ =40°) of the Triangular Nanostructures

In this step the vertex angles of two triangular nanostructures' edges facing each other were further reduced to 40°, resulting in further elongation of nano-structure.

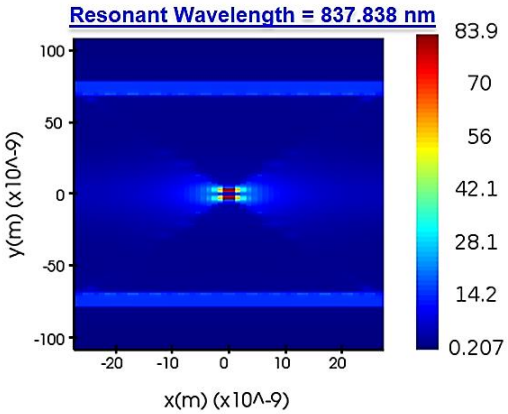

Figure 4.4 Electric field enhancement produced by Array of bowtie with Vertex Angles (θ1 = θ2=40°) of the Triangular Nanostructures.

Each of the triangular nanostructures was elongated to 68.7 nm, moving the grating walls farther from each other in danger proportion. This configuration obtained a

maximum electric field enhancement of 83.9 and an enhancement factor of $4.9x10^7$ at resonant wavelength 837.838 nm.

4.1.5 Bowtie with Vertex Angles ($\theta_1 = \theta_2 = 30°$) of the Triangular Nanostructures

In this subsection the vertex angle of the bowtie at edges facing each other was reduced to 30°. The triangular nanostructures of bowtie had length $h_1 = h_2$ equal to 93.3 nm. This structure provided two maxima of electric field intensity enchantment equal to 89.6 and 76.1 and enhancement factors of $6.4x10^7$ and $3.3\ x10^7$ at resonant wavelengths 1000 nm and 746.988 nm respectively.

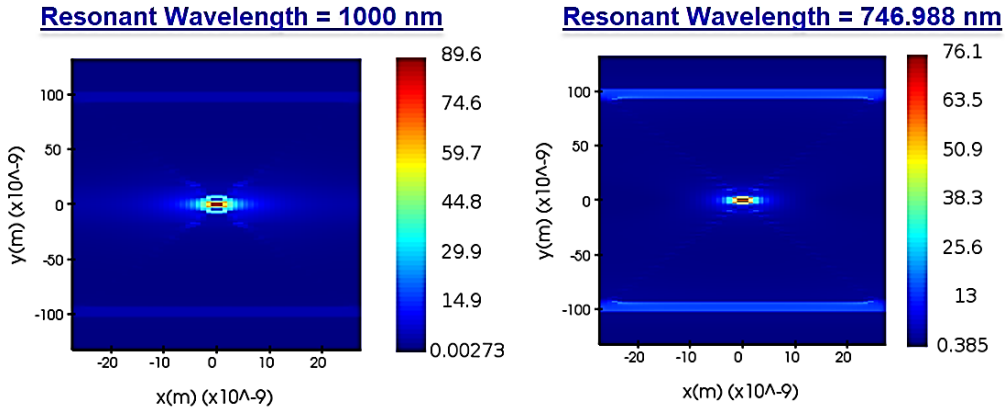

Figure 4.5 Electric field enhancement produced by Array of bowtie with Vertex Angles (θ1 = θ2=30°) of the Triangular Nanostructures.

4.1.6 Bowtie with Vertex Angles ($\theta_1 = \theta_2 = 20°$) of the Triangular Nanostructures

Finally the vertex angle of the triangular nano-structure was reduced to 20°, this elongated dimensions $h_1 = h_2$ equal to 141.8 nm

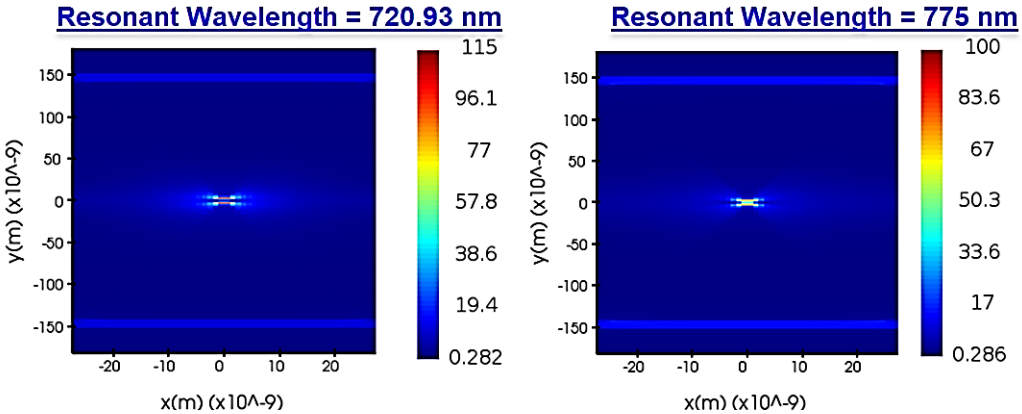

Figure 4.6 Electric field enhancement produced by Array of bowtie with Vertex Angles (θ1 = θ2=20°) of the Triangular Nanostructures.

4.1.7 Results and Observations

From analysis of this section it was inferred that the maximum electric field enhancement was provided by bowtie nanostructure bearing combination of two equal triangular nanostructures with vertex angle 20° providing an electric field enhancement of 115 at resonance wavelength equal to 720.93 nm. Rest of the configurations considered provided sub-hundred electric field intensity enhancements. Results of all the subsections 4.1.2 to 4.1.6 are be brought together in tabular form in Table 4.2.

Vertex Angle	Length of Triangular Nanostructure (nm)	Maximum Electric Field Intensity Enhancement	Enhancement Factor	Resonance Wavelength (nm)
60°	43.3	48.5	5.53×10^6	696.629
50°	53.6	73.7	2.95×10^7	837.838
40°	68.7	83.9	4.96×10^7	837.838
30°	93.3	89.6, 76.1	6.45×10^7	1000, 746.988
20°	141.8	100, 115	1.75×10^8	775, 720.93

Table 4.2 Results obtained from array of symmetric triangular bowtie nanostructure with base length of triangle constant.

It was observed that the maximum enhancement of electric field obtained was of 115 for vertex angle equal to 20° at a resonant wavelength of 720.93 nm.

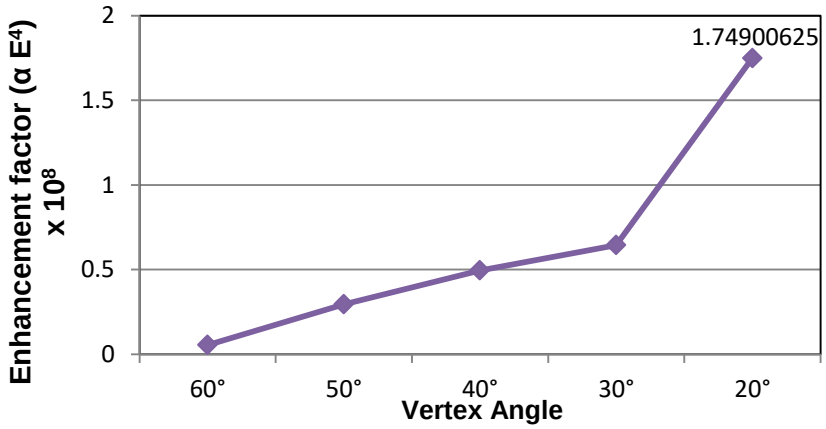

Figure 4.7 Graphical representation of enhancement factor obtained from array of symmetric triangular bowtie nano structure with variable width

From analysis of the nanostructures in this section it was observed that there are many contributing factors towards electric field intensity enhancement, these maybe

(a) Increased length of nano-structures.

(b) Decreased duty cycle of nano-gratings.

(c) Decreased vertex angles providing sharper edges and higher convergence of field lines.

(d) Increased area of nano-structure.

(e) Increased size of base substrate, collecting more electric field lines.

As there are many factors influencing overall field enhancement, therefore it is not feasible to ascertain which factor has contributed towards enhancement and which has reduced the overall electric field intensity. It was noticed that these many contributing factors were generated because of variation of height of isosceles triangular side lobes (h_1 and h_2) in proportion with vertex angles (θ_1 and θ_2). Therefore some alternate method was required to be devised to limit the number of factors influencing the electric field enhancement. To eliminate such kind of anomalies it was decided to vary the width of the triangular nanostructure (a and b) in proportion with vertex angles (θ_1 and θ_2), refer Fig. 4.8, keeping length of the triangular nanostructure constant (h_1 and h_2 = 43.3 nm). This will also ensure that the distance between two consecutive grating walls is constant different structural configurations considered.

4.2 ARRAY OF SYMMETRIC BOWTIE NANOSTRUCTURE WITH VARIABLE BASE LENGTH OF TRIANGULAR NANOSTRUCTURES

In this section the vertex angles of the bowtie nanostructure was varied such that the overall width of the bowtie is not varied and buth length of the bowtie is varied. This ensures that duty cycle of the nano-gratings is maintained constant during the course of all the simulations.

4.2.1 Structural details

The closer edges of triangular nano-structures are 5 nm apart and distance between bowtie nanostructures and grating walls is 10 nm (refer fig. 4.8). Distance between two consecutive bowtie structures is maintained 5 nm in X direction. The angle θ_1 and θ_2 are varied such that dimensions 'a' and 'b' vary, keeping h_1 equal to h_2 constant for all the nanostructures considered in this section. The thickness of base and all nanostructures is 50 nm and monitor bisects the bowtie nano-structure at its middle and passes through point 0,0,0 in XYZ Cartesian coordinates. This structure is so designed that it is periodic in x and y direction.

All the standard parameters which were decided to be followed in previous sections and their subsections followed in this section too and maintained for all the nano structural configurations considered in this section. The standard norms may be recapitulated from following points:

(a) All the nano-structures are placed in XY plane and iterated to create a periodic array in both directions.

(b) Observations were made on a bandwidth of 600 nm ranging from 400 nm to 1000 nm.

(c) Smallest gap between nano-structures (triangular nanostructures) is g=5nm

(d) The nano-gratings are kept at 10nm from the bowtie nano structure.

(e) The duty cycle of the grating is 35% iterating in y direction with following properties:

(i) Grating depth=50 nm

(ii) Grating period = 60 +111.6= 171.6nm

(iii) Filling factor= 60/171.6= 0.35

(f) The height of the isosceles triangular nano-structure is constant and equal to 43.3 nm.

(g) Base length of the triangular nanostructures is varied in proportion with vertex angles θ_1 and θ_2.

(h) Material of all nano structures is gold (Au(CRC)).

(i) The source is maintained above the nano-structure at distance of 20 nm from it, at (0,0,45) in Cartesian coordinates.

All these parameters may be understood easily with the help of Fig. 4.8.

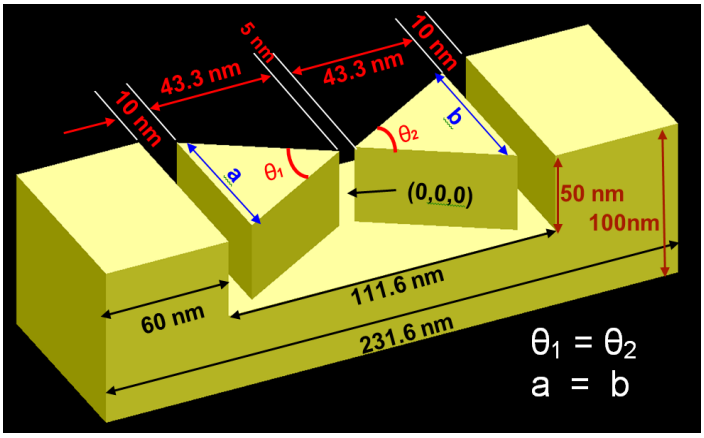

Figure 4.8 Symmetric bowtie nanostructure with variable base length of triangular nanostructures.

4.2.2 Vertex angles (θ_1 and θ_2) of both the nanostructures equal to 20°

First of all the triangular bowtie with vertex angles of 20° of edges of triangular nanostructure facing each other and with corresponding base length of 15.2 nm was analyzed. The wavelength was varied over bandwidth of 600 nm from 400 to 1000 nm and the highest electric field intensity enhancement of 57.2 was obtained at resonance wavelength of 696.629 nm (refer Fig. 4.9 (a)).

4.2.3 Vertex angles (θ_1 and θ_2) of both the nanostructures equal to 30°

Secondly the vertex angle was increased to 30° which in turn increased the length of bowtie nanostructure to 23.2 nm. After scanning over the bandwidth from 400

to 1000 nm the resonance was obtained at 746.988 nm providing electric field intensity enhancement of 51 (refer Fig. 4.9 (b)).

4.2.4 Vertex angles (θ_1 and θ_2) of both the nanostructures equal to 40°

The vertex angle of triangular nanostructures of symmetric bowtie was increased to 40° leading to bowtie increased to 31.6 nm. On scanning the whole bandwidth of 600 nm at 32 wave points, the resonance was obtained at 720.93 nm providing an electric field intensity enhancement of 36.8 (refer Fig. 4.9 (c)).

4.2.5 Vertex angles (θ_1 and θ_2) of both the nanostructures equal to 50°

This was followed by the analysis of nano-bowtie having triangular nanostructures with vertex angle 50° resulting into the base width of each of the triangular nanostructures equal to 40.4 nm. In this case resonance wavelength was obtained at 673.913 nm providing maximum enhanced electric field intensity of 41.7 (refer Fig. 4.9 (d)).

4.2.6 Vertex angles (θ_1 and θ_2) of both the nanostructures equal to 60°

After triangular nanostructures nano-structures with vertex angle of 50° it was increased to 60° which makes width of bowtie triangular nano-structure equal to 25 nm. In this case the resonant wavelength was obtained at 696.629nm and maximum electric field intensity enhancement factor was 48.5 (refer Fig. 4.9 (e)).

4.2.7 Vertex angles (θ_1 and θ_2) of both the nanostructures equal to 70°

The vertex angle of edges of triangular nano-structures of the bowtie facing each other was increased from 60° to 70° to analyse if it further enhances the electric field intensity or not. In this the maximum enhancement of electric field intensity was 48.9 at a resonant wavelength 873.293 nm (refer Fig. 4.9 (f)).

4.2.8 Vertex angles (θ_1 and θ_2) of both the nanostructures equal to 80°

In this vertex angle of edges of triangular nanostructure nano-structure facing each other was increased to 80° leading to base length of each of the nanostructures (a =

b) equal to 72.6 nm. This provided an electric field intensity enhancement of 70.1 at resonant wavelength of 673.913 nm (refer Fig. 4.9 (g)).

4.2.9 Vertex angles (θ_1 and θ_2) of both the nanostructures equal to 90°

Finally the isosceles triangular nanostructures vertex angle of the edges facing each other was increased to 90° leading to base length of triangles (a = b) equal to 86.6 nm. This structural arrangement provided electric field enhancement of 53 at resonant wavelength of 673.913 nm (refer fig. 4.9 (h)).

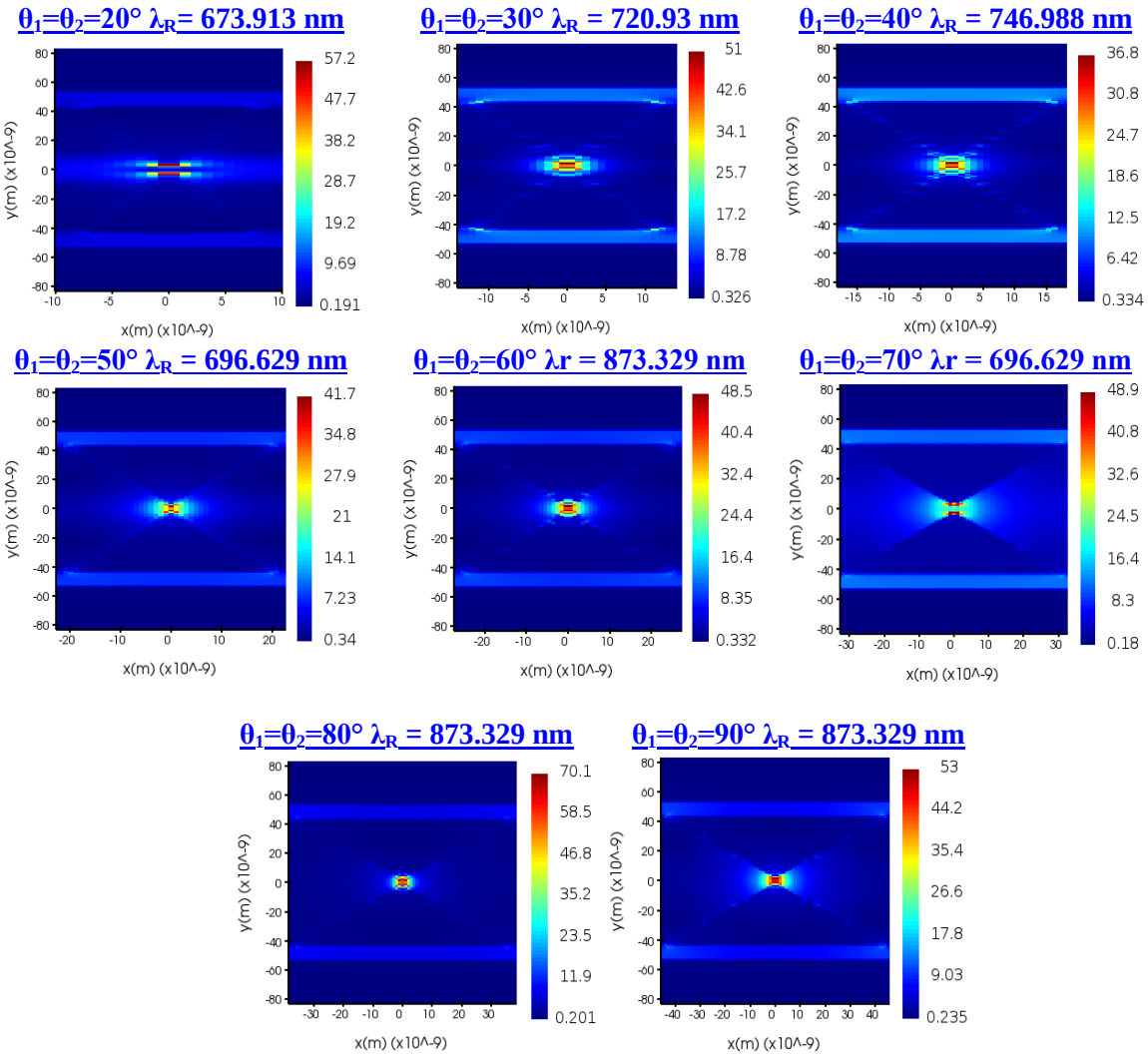

Figure 4.9 Electric field enhancement produced by array of symmetric bowtie nanostructure with variable base length of triangular nanostructures

4.2.10 Results and Observations

In this section nine symmetric structural arrangements of bowtie were studied using triangular nanostructures nano-structures by varying the triangular nanostructures vertex angle of edges facing each other. Performance of each of the structural configuration was studied on bandwidth of 600 nm ranging from 400 to 1000 and it was found that highest intensity of 70.1 and bowtie with vertex angle of 80°, this could have been a possible result of increased width of triangular nanostructure nano-structure. While another maxima of enhancement of electric field intensity of value equal to 57.2 was obtained for structural configuration of bowtie with 20° as its vertex angle this would have been due to higher convergence of electric field at the sharp edges of 20° triangular nanostructure.

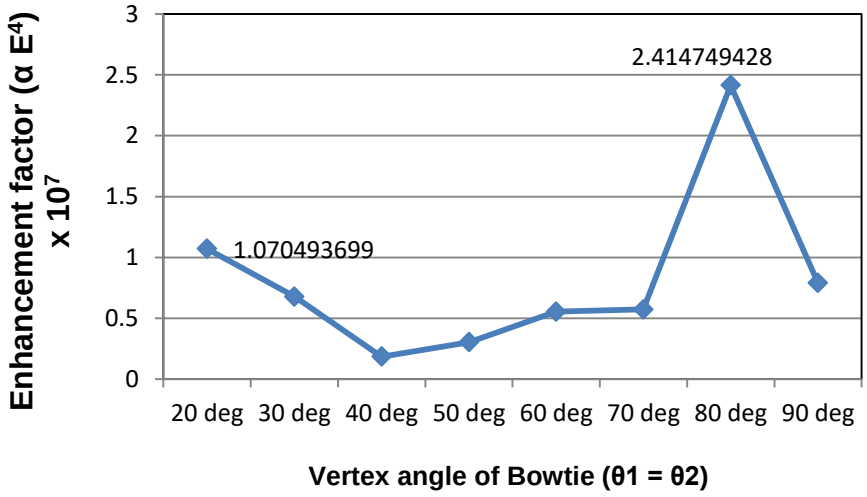

Figure 4.10 Graphical representation of EM enhancement factor produced by array of symmetric bowtie nanostructure with variable length

It was noticed that more or less most of the enhancement values are close to 50 in case of all the symmetric bowties with height of triangles in triangular nanostructure nano-structures constant and equal to 43.3 nm. Results of all these bowtie nano-structures may be put together in the table 4.3.

Sl.no.	Vertex angle of Bowtie $\theta_1 = \theta_2$	Base length of triangular nanostructures	Highest enhanced electric field intensity	Enhancement factor	Resonance wavelength
1	20^0	15.2	57.2	1.07×10^7	696.629
2	30^0	23.2	51	6.77×10^6	746.988
3	40^0	31.6	36.8	1.83×10^6	720.93
4	50^0	40.4	41.7	3.02×10^6	673.913
5	60^0	50	48.5	5.53×10^6	696.629
6	70^0	60.6	48.9	5.72×10^6	873.239
7	80^0	72.6	70.1	2.41×10^7	746.988
8	90^0	86.6	53	7.89×10^6	673.913

Table 4.3 Results of array of symmetric bowtie nanostructure with variable length

In this section it was observed that symmetrical nano-bowties were not able to produce a significant enhancement of electric field intensity therefore in next section the asymmetric bowtie nanostructures will be analyzed.

4.3 ARRAY OF ASYMMETRIC BOWTIE NANOSTRUCTURE WITH VARIABLE BASE LENGTH OF TRIANGULAR NANOSTRUCTURES

Having analyzed the symmetric bowtie nanostructures in the previous section the highest enhancement factor obtained was of the orer of 10^7. The possibility of further enhancement of electric field intensity is analyzed in this section by making bowtie nanostructures asymmetric.

4.3.1 Structural Details

In previous section most of the symmetric nano-bowties provided electric field intensity enhancements of the close to 50. So it cannot be clearly demarcated which nanostructural configuration is better one with narrow vertex angle in which enhancement is due to effective convergence of electric field lines or the one with wider vertex angle enhancing electric field intensity due to collection of more electric field

lines. So to clarify this aspect all the combination of different vertex angles of the two triangular nanostructures of the bowtie will be analyzed in this section. In this section nano-bowtie will be made asymmetric by chosing different values for vertex angles θ_1 and θ_2, but rest of the structural details will remain same as were in the previous section. To make this analysis simpler vertex angle of one of the triangular nanostructures is made fixed and vertex angle of another triangular nanostructure is varied so that all the all the possible combinations may be executed and the best possible asymmetric bowtie nano-structure to provide highest electric field intensity enhancement may be obtained. All these parameters may be more clearly understood using fig. 4.11.

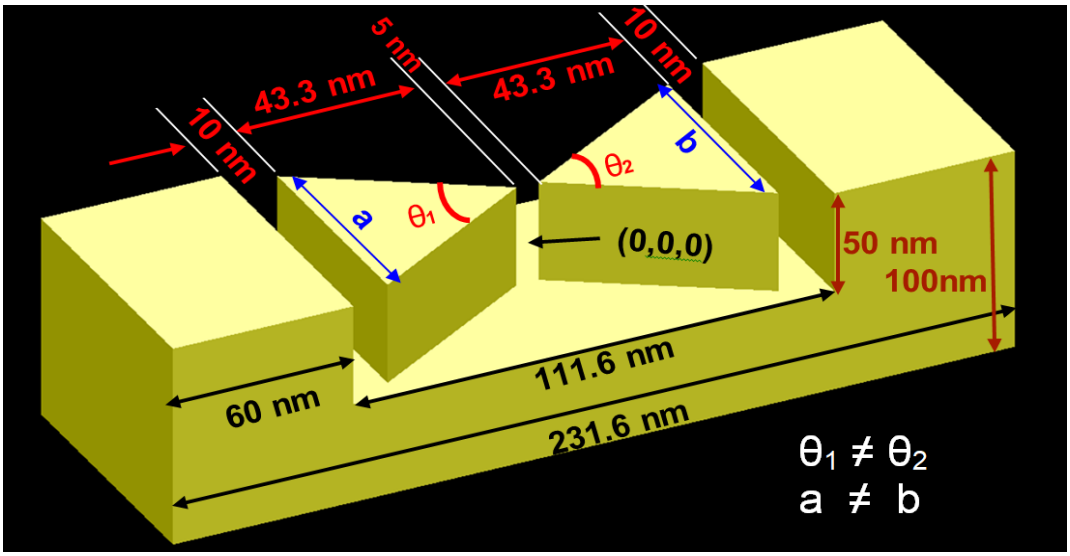

Figure 4.11 Asymmetric Bowtie Nanostructure with Variable Base Length of Triangular Nanostructures

4.3.2 Analysis

Analysis of these asymmetric bowtie in nanostructures is performed in the following subsections. During course of analysis of these structures the vertex angle of one of the triangular nanostructures of asymmetric bowtie will be kept fixed and that of the second triangular nanostructure will be varied to simulate all possible combinations.

4.3.3 Array of asymmetric Bowtie with θ_1 = 20° and θ_2 variable

In this nanostructural arrangement an array of triangular nano-bowtie is considered for its SERS response. In asymmetric bowtie one of the triangular

nanostructure has a vertex angle equal to 20° and it was kept fixed while the second nanostructure was varied with its vertex angle as 30°, 40°, 50°, 60°, 70°, 80° and 90°. When the first nanostructure of the triangular bowtie was kept constant with a vertex angle of θ_1=20° the dimension 'a' was equal to 15.2 nm. The dimension 'b' of the second triangular nanostructure were varied in proportion with variation of angle θ_2 as 30°, 40°, 50°, 60°, 70°, 80° and 90° one by one , refer Fig. 4.12. When the angle θ_2 is 30° the dimension 'b' becomes equal to 23.2 nm. It can be illustrated with the help of Fig.4.12.

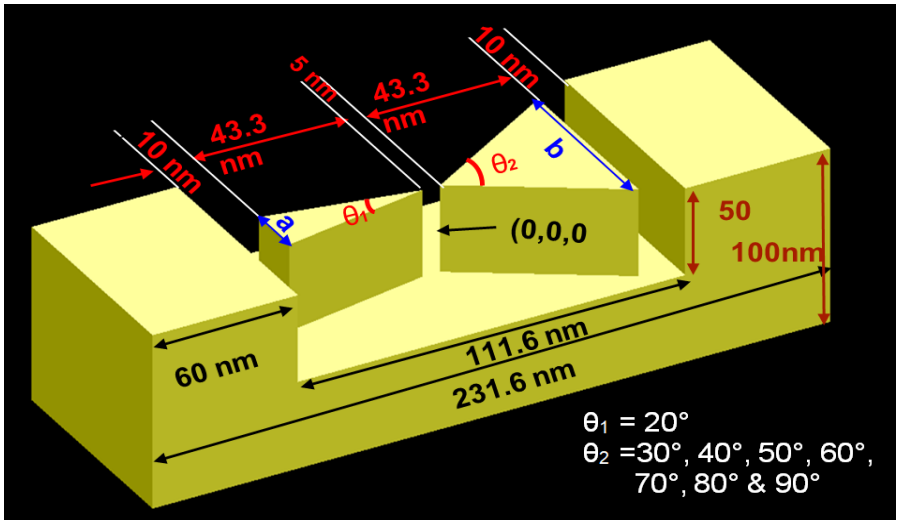

Figure 4.12 Array of Bowtie having Triangular nanostructures with 20° and variable vertex angle.

With this configuration of bowtie with vertex angles of 20° and 30° the maximum electric field enhancement obtained was 91.5 at a resonant wavelength of 720.93 nm. Now again the value of θ_2 is increased to 40°, providing an electric field enhancement of 111 at resonant wavelength of 775 nm. In a similar fashion the similar structure with second vertex angle equal to 50° which has shown enhancement of 137 with resonance at 775 nm. Further increment of angle θ_2 to 60° provided an enhancement of 137 at a resonant wavelength of 775 nm. The angle θ_2 was varied from 60° to 70° with resonance at 632.653 nm and the maximum electric field intensity enhancement of 60.4. For the increment of angle θ_2 to 80° provided an enhancement of electric field intensity equal to 61.5 at resonance wavelength of 652.632 nm. Finally the angle θ_2 was increased to 90° increasing dimension 'b' to 86.6 nm. This configuration has shown a little higher

electric field enhancement of 70.4 at the same resonance wavelength as that of 80° i.e. 652.632 nm. All these results are summarized in the table 4.4.

First triangle vertex angle (θ_1)	Second triangle vertex angle (θ_2)	Electric Field Enhancement	Enhancement Factor	Resonant Wavelength (nm)
20°	30°	91.5	7.01×10^7	720.93
20°	40°	111	1.52×10^8	775
20°	50°	46.9	4.84×10^6	652.632
20°	60°	137	3.52×10^8	775
20°	70°	60.4	1.33×10^7	632.653
20°	80°	61.5	1.43×10^7	652.632
20°	90°	70.4	2.46×10^7	652.632

Table 4.4 Results of bowtie with first triangular side lobe nanostructure with vertex angle 20° and second with variable vertex angle.

Results mentioned in table are elaborated using the following fig. 4.13 depicting all nine configurations of bowtie with first triangular side lobe nanostructures with vertex angle 20° and second with variable vertex angle.

(a) 30° Resonant Wavelength = 720.93 nm **(b) 40° Resonant Wavelength = 775 nm**

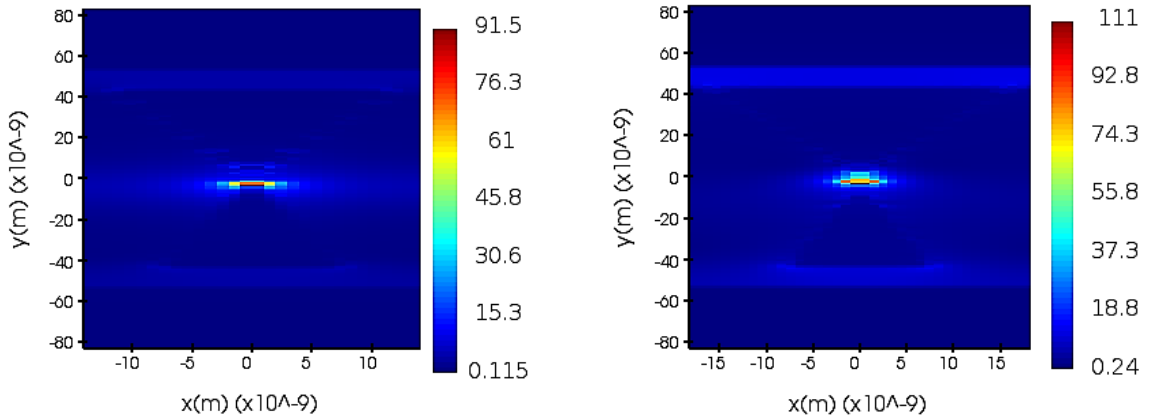

Figure 4.13 Enhacement of electric field intensity by bowtie with first triangular side lobe nanostructures with vertex angle 20° and second with variable vertex angle θ_2 = (a) 30° (b) 40° (c) 50° (d) 60° (e) 70° (f) 80° (g) 90°

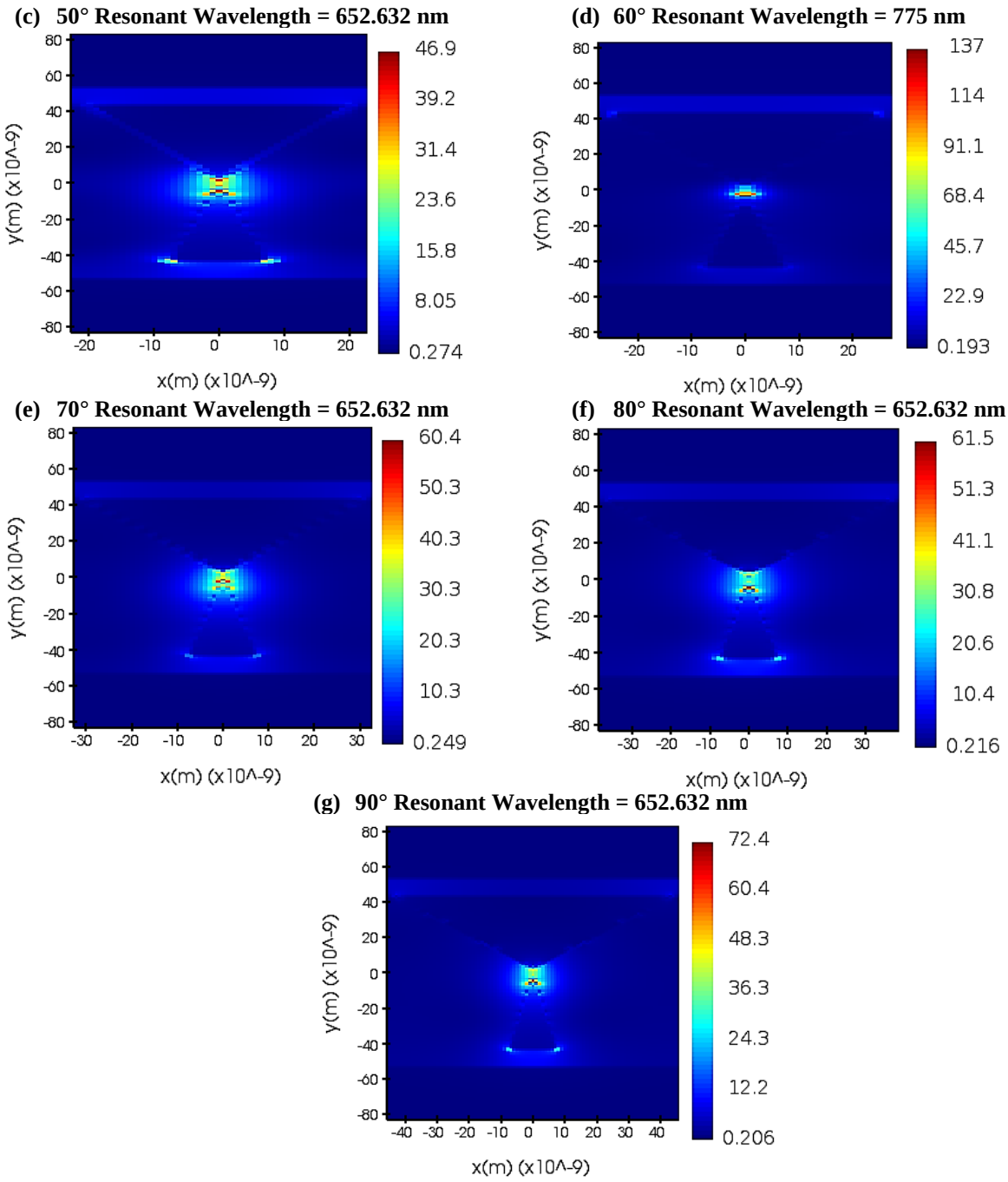

Figure 4.13 Enhancement of electric field intensity by bowtie with first triangular side lobe nanostructures with vertex angle 20° and second with variable vertex angle θ_2 = (a) 30° (b) 40° (c) 50° (d) 60° (e) 70° (f) 80° (g) 90°

From above results it is noted that with smaller dimensions the resonance is obtained at larger wavelength while the bowtie nanostructures with larger vertex angles triangular nanostructure found to have resonance at smaller wavelengths. This subsection may be concluded with the best results obtained from nano-structure with two triangular

nanostructures having vertex angles 20° and 60° respectively at resonance wavelength of 775 nm and maximum electromagnetic field intensity enhancement by a factor of 137.

4.3.4 Array of asymmetric Bowtie with θ_1 = 30° and θ_2 variable

In this configuration all the structural parameters were kept as were in previous subsection the two differences as compared to previous subsection of "bowtie triangular nanostructure 20° and variable vertex angle" are as follows:

(a) $\theta_1 = 30°$ resulting in dimension 'a' equal to 23.2 nm.

(b) θ_2 is varied as 40°, 50°, 60°, 70°, 80° and 90° and dimension 'b' varies proportionally.

With the combination of 30° and 40° as vertex angles of two triangular nanostructures of the asymmetric bowtie, an electric field intensity enhancement of 75.8 at resonance wavelength of 632. 653 nm was obtained. an increment of 10° in the vertex angle of second triangular nanostructure θ_2 making it 50°provided an enhancement of electric field intensity by a factor of 48.7 at resonance wavelength of 720.93 nm. On increasing the second vertex angle to 60° the enhanced electric field intensity was also increased to 91.4 at 634.653 nm as resonant wavelength. When the second triangular nanostructure vertex angle θ_2 was increased to 70° the electric field intensity enhancement factor was found to decrease to 49.3 at the resonance wavelength of 953.846 nm. Minor increase in electric field intensity enhancement was observed as it increased to 57.5 with an increment of 10° in vertex angle θ_2 to 80^0 at resonance wavelength of 720.93 nm. Finally the vertex angle of the second triangular nanostructure of bowtie nano-structure was increased to 90°providing an electric field intensity enhancement of 55.1 at resonant wavelength of 652.632 nm. All these results are brought together in Table 4.5.

First triangle vertex angle (θ_1)	Second triangle vertex angle (θ_2)	Electric Field Enhancement	Enhancement Factor	Resonant Wavelength (nm)
30°	40°	75.8	3.30×10^7	632.653

First triangle vertex angle (θ_1)	Second triangle vertex angle (θ_2)	Electric Field Enhancement	Enhancement Factor	Resonant Wavelength (nm)
30°	50°	48.7	5.62×10^6	720.93
30°	60°	91.4	6.98×10^7	632.653
30°	70°	49.3	5.91×10^6	953.846
30°	80°	57.5	1.09×10^7	720.93
30°	90°	55.1	9.22×10^6	652.632

Table 4.5 Results of bowtie with first triangular side lobe nanostructure with vertex angle 30° and second with variable vertex angle.

Results mentioned in table 4.5 are elaborated using fig. 4.15 depicting simulation output of enhanced electric field of all configurations of bowtie with first triangular side lobe nanostructures with vertex angle 30° and second with variable vertex angle θ_2.

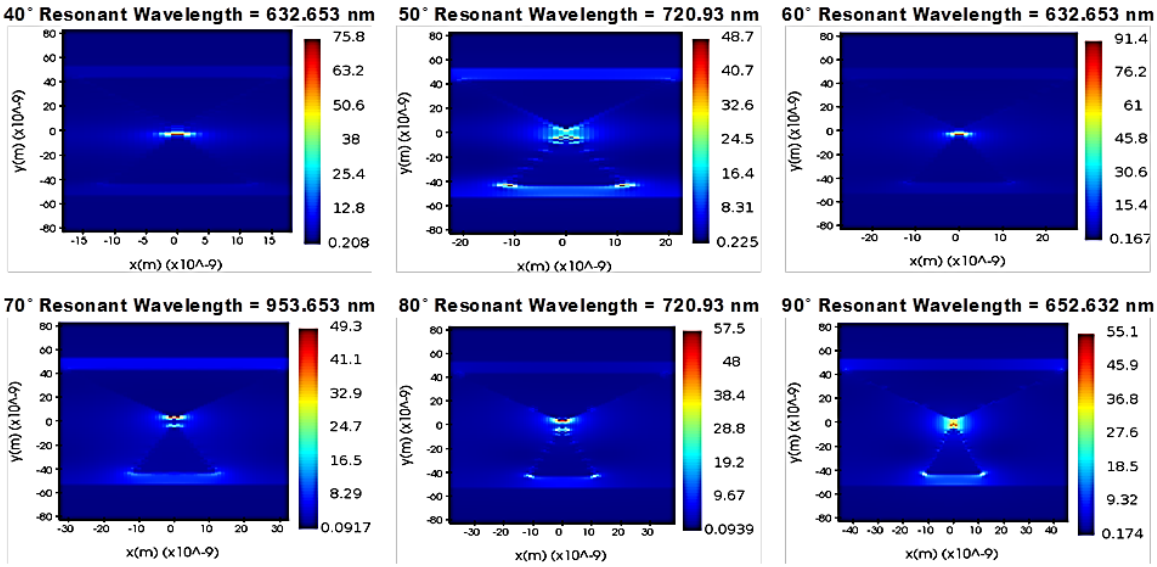

Figure 4.14 Enhancement of electric field intensity by bowtie with first triangular side lobe nanostructures with vertex angle 30° and second with variable vertex angle θ_2 = 40°, 50°, 60°, 70°, 80°, 90°

From the above results it may be concluded that the bowtie nano-structure while keeping one of the triangular nanostructure with constant vertex angle of θ_1 = 30° and with a second triangular nanostructure with variable vertex angle $\theta_2 = 60^0$, provided

the highest electric field intensity enhancement of 91.4 at resonant wavelength of 632.653 nm , which is much less than that obtained in the previous subsection. In the next subsection an increment of 10° will be imposed on the first triangular nanostructure of the bowtie to make it 40° with a second triangular nanostructure with variable vertex angle θ_2 will be implemented.

4.3.5 Array of asymmetric Bowtie with $\theta_1 = 40°$ and θ_2 variable

In this section the bowtie structure with first triangular nanostructure with vertex angle of $\theta_1 = 40°$ and second triangular Nano lobe with variable vertex angle θ_2 is analyzed. Prior to starting the analysis part it will be apt to have a look at the structural details of this nanostructure. All the structural details in this configuration are similar to the previous subsections refer **fig. 4.11** with following two differences:

(a) $\theta_1 = 40°$ resulting in dimension 'a' equal to 31.6 nm.

(b) θ_2 is varied as 50°, 60°, 70°, 80° and 90° and dimension b varies proportionally.

While keeping the first triangular nanostructure of bowtie nano-structure same for all the simulations in this subsection with constant vertex angle of 40° and vertex angle of second nanostructure is varied from 50° to 90°. In this row the first combination is made with vertex angles of 40° and 50° of two triangular nanostructures of bowtie nano-structure. This combination provided a maximum electric field enhancement factor of 74.5 at resonant wavelength of 746.988 nm. The second combination was made between two triangular nanostructures with vertex angles equal to 40° and 60° obtaining a resultant enhancement of 59 at resonant wavelength of 596.154 nm. a third combination of 40° and 70° as vertex angles of the two triangular nanostructures of bowtie nano-structure resulted in an electric field enhancement factor of 83.1 with 746.988 nm as resonance wavelength. The next combination was made between two triangular nanostructures of bowtie nano-structure with vertex angles of 40° and 80° respectively producing 88.2 do as enhancement factor of electric field intensity at resonance wavelength of 746.988 nm.

First triangle vertex angle (θ_1)	Second triangle vertex angle (θ_2)	Electric Field Enhancement	Enhancement Factor	Resonant Wavelength (nm)
40°	50°	74.5	3.08×10^7	746.988
40°	60°	59	1.21×10^7	596.154
40°	70°	83.1	4.77×10^7	746.988
40°	80°	88.2	6.05×10^7	746.988
40°	90°	101	1.04×10^8	746.988

Table 4.6 Results of bowtie with first triangular side lobe nanostructure with vertex angle 40° and second with variable vertex angle θ_2 = 50°, 60°, 70°, 80°, 90°

The final combination of this subsection was between 40° and 90° as vertex angles of the two triangular nanostructures of bowtie nano-structure giving the highest electric field enhancement factor of 101 at resonant wavelength 746.988 nm. The observations made in this subsection may be written together in the following table 4.6 and the same are elaborated using the following fig. 4.16 depicting all nine configurations of bowtie with first triangular side lobe nanostructures with vertex angle 40° and second with variable vertex angle.

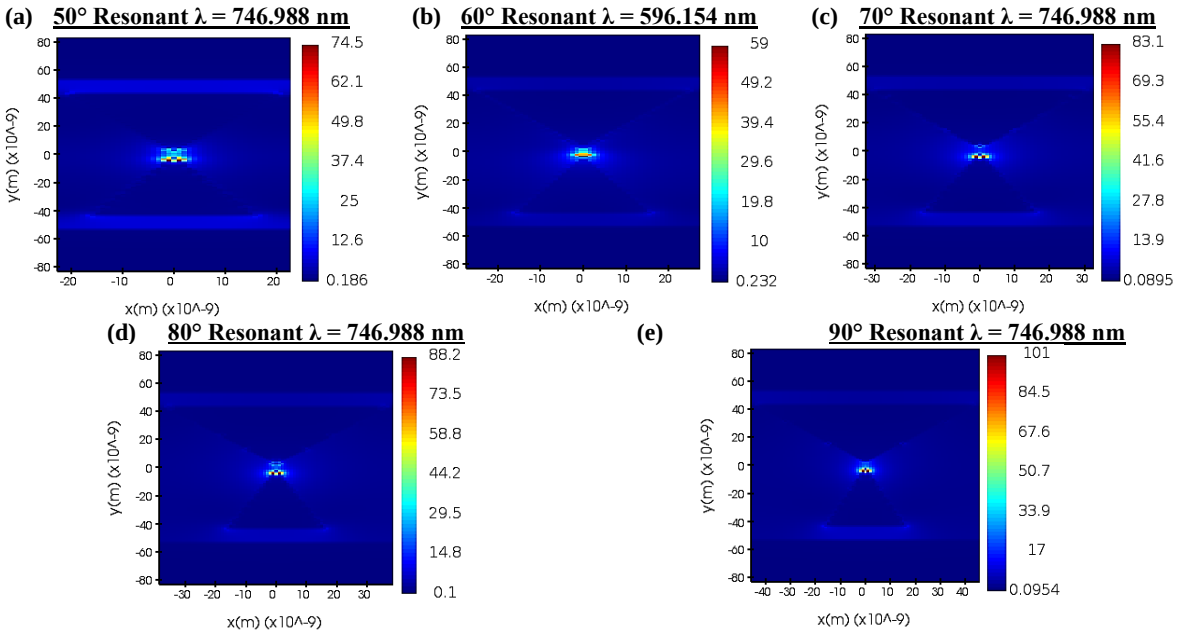

Figure 4.15 Enhancement of electric field intensity by bowtie with first triangular side lobe nanostructures with vertex angle 40° and second with variable vertex angle (a) 50° (b) 60° (c) 70° (d) 80° (e) 90°

From the above results it is inferred that enhancement of electric field intensity produced by all the structural configurations considered in this subsection is better than those produced in the previous subsection. Though out of five nanostructural configurations four produced electric field intensity enhancement factor greater than 80 but the highest enhancement factor of electric field intensity was produced by combination of vertex angles $\theta_1 = 40°$ and $\theta_2 = 90°$ of triangular nanostructures of bowtie providing 101 enhancement factor at 746.988 nm resonant wavelength.

4.3.6 Array of asymmetric Bowtie with $\theta_1 = 50°$ and θ_2 variable

In this subsection the bowtie nanostructure with one of its triangular nanostructure fixed with its vertex angle $\theta_1 = 50°$ and second triangle nanostructure with variable vertex angle θ_2 is considered. All the structural details will be maintained just like the previous subsections but with two deviations, these are as follows:

(a) $\theta_1 = 50°$ resulting in dimension 'a' equal to 50 nm.

(b) θ_2 is varied as 60°, 70°, 80° and 90° and dimension 'b' varies proportionally.

In the first combination between two triangular nanostructures of bowtie nanostructures the vertex angles are equal to 50° and 60° respectively which provided and electric field enhancement of 48.4 at a resonant wavelength of 720.93 nm. In second combination the triangular side job with 60° was replaced by nanostructure with vertex angle of 70° entailing to electric field enhancement of 48.3 at a resonant wavelength of 673.913 nm. The next combination was between 50° and 60° vertex angles of triangular nanostructures of bowtie resulting into enhancement 65.2 at 720.93 nm of resonant wavelength. The final combination of 50° and 90° as vertex angles of the two nanostructures provided 66.2 as enhancement effect of electric field intensity and wavelength of 673.913 nm, refer fig. 4.17 (a), (b), (c), (d).

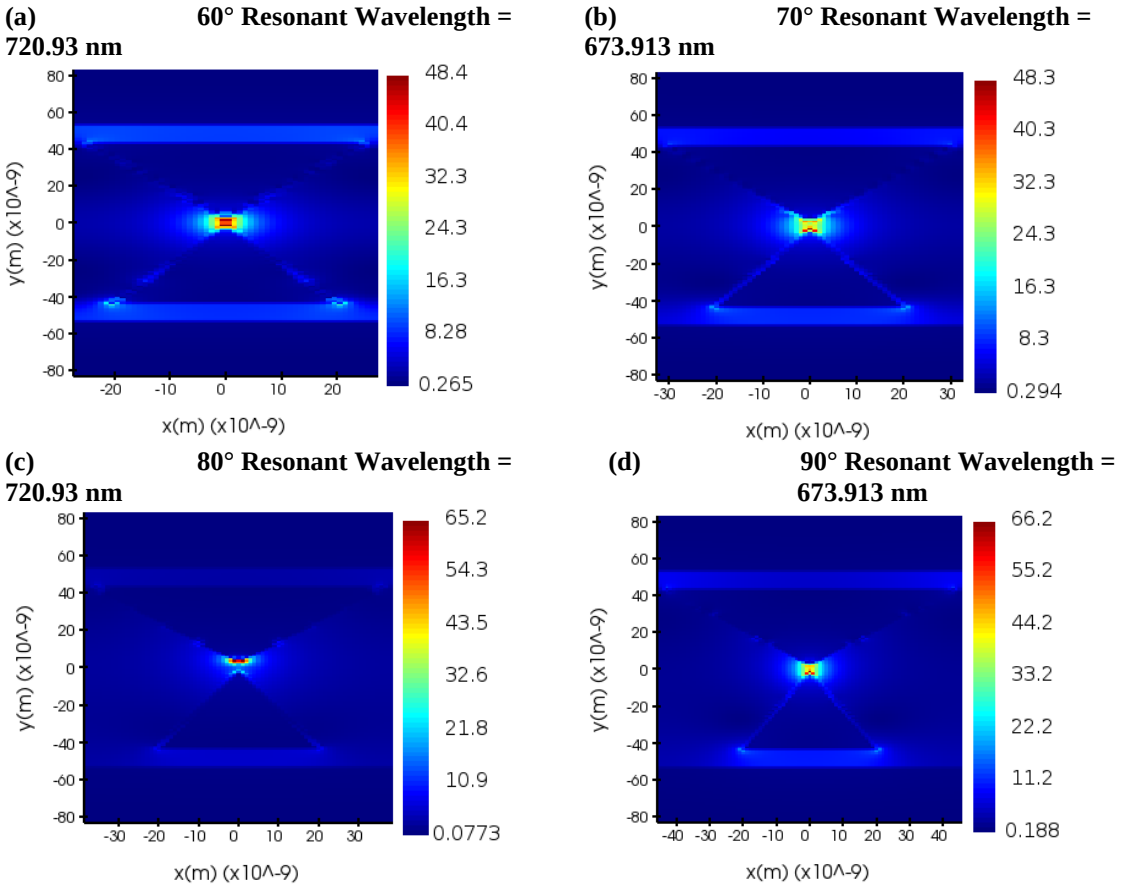

Figure 4.16 Enhancement of electric field intensity by bowtie with first triangular side lobe nanostructures with vertex angle 50° and second with variable vertex angle (a) 60°, (b) 70°, (c) 80°, (d) 90°

All these results covered in this subsection may be concluded into following

All these results obtained in this subsection may be wrapped up into following table:

First triangle vertex angle (θ_1)	**Second triangle vertex angle (θ_2)**	**Electric Field Enhancement**	**Enhancement Factor**	**Resonant Wavelength**
50°	60°	48.4	5.49×10^6	720.93
50°	70°	48.3	5.44×10^6	673.913
50°	80°	65.2	1.81×10^7	720.93
50°	90°	66.2	1.92×10^7	673.913

Table 4.7 Results of bowtie with first triangular side lobe nanostructure with vertex angle 50° and second with variable vertex angle (a) 60°, (b) 70°, (c) 80°, (d) 90°

This subsection may be concluded with the remark that in this subsection bowtie with triangular nanostructure vertex angles as $\theta_1 = 40°$ and $\theta_2 = 90°$ provided the best enhancement of electric field intensity as 66.2 two at resonant wavelength of 673.913 nm. But this electric field enhancement is quite lower as compared to the configurations covered in the first subsection with 20° as vertex angle θ_1 as fixed triangular nanostructure of the nano-bowtie.

4.3.7 Array of asymmetric Bowtie with $\theta_1 = 60°$ and θ_2 variable

This subsection will deal with a nanostructural arrangement with one of its triangular nanostructures fixed with its vertex angle as $\theta_1 = 60°$ and the vertex angle of the second triangular nanostructure is varied from $\theta_2 = 70°$ to 90°. All the structural parameters of the nanostructure configuration are considered in this subsection will remain same as were in the previous subsections with following two exceptions refer fig. 4.11:

(a) $\theta_1 = 60°$ resulting in dimension 'a' equal to 40.4 nm.

(b) θ_2 is varied as 70°, 80° and 90° and dimension 'b' varies proportionally.

This subsection starts with analysis of a bowtie nano-structure with first triangular nanostructure having vertex angle $\theta_1 = 60°$ which will remain same for rest of the three configurations to be considered in this subsection while the second triangular nanostructure had vertex angle θ_2 equal to 70°. This configuration provided a maximum of electric field enhancement factor as 40.7 at resonant wavelength of 696.629 nm. In the second configuration the side with $\theta_2 = 70°$ as vertex angle was replaced by another triangular nanostructure with $\theta_2 = 80°$ as vertex angle resulting in maximum electric field enhancement equal to 67.4 at a resonant wavelength of 720.93 nm. The final configuration had the variable nanostructure vertex angle equal to $\theta_2 = 90°$ with maxima of electric field enhancement equal to 53.8 at 696.629 nm as resonant wavelength, refer fig. 4.18 (a), (b), (c).

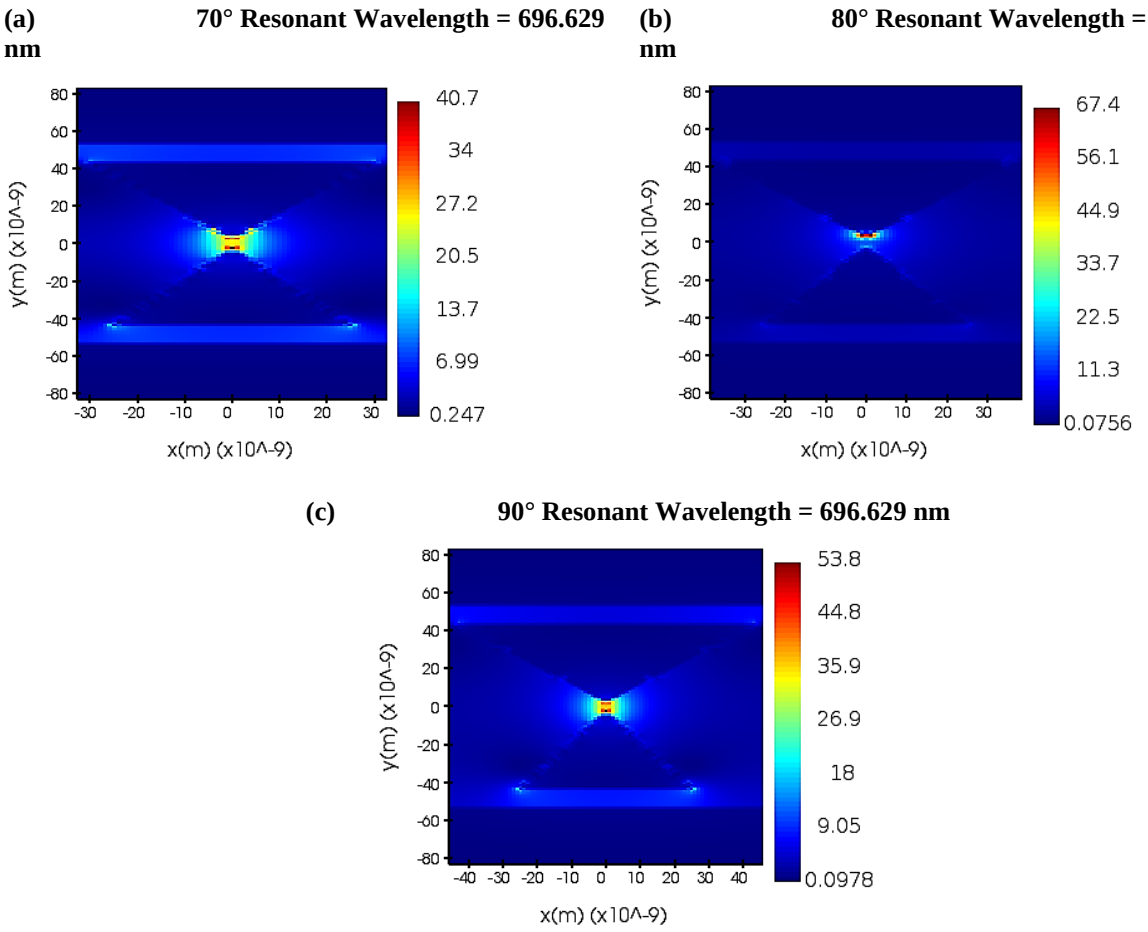

Figure 4.17 Enhancement of electric field intensity by bowtie with first triangular side lobe nanostructures with vertex angle 60° and second with variable vertex angle (a) 70°, (b) 80°, (c) 90°.

Though the results shown in fig. 4.18 are self-elaborative, the results obtained in this subsection may be wrapped up into table 4.8.

First triangle vertex angle (θ_1)	Second triangle vertex angle (θ_2)	Electric Field Enhancement	Enhancement Factor	Resonant Wavelength (nm)
60°	70°	40.7	2.74×10^6	696.629
60°	80°	67.4	2.06×10^7	720.93
60°	90°	53.8	8.38×10^6	696.629

Table 4.8 Results of bowtie with first triangular side lobe nanostructure with vertex angle 60° and second with variable vertex angle (a) 70°, (b) 80°, (c) 90°.

This subsection can be concluded with the best electric field enhancement produced by structural configurations considered in this subsection with fixed vertex angle θ_1 equal to 60° and variable vertex angle θ_2 equal to 80° resulting into electric field enhancement 67.4 at resonant wavelength of 720.93 nm. Just like the previous subsection the enhancement provided by nanostructural configurations considered in this subsection did not provide sufficient enhancement of electric field intensity.

4.3.8 Array of asymmetric Bowtie with θ_1 = 70° and θ_2 variable

This subsection will cover bowtie nano-structure arrangements with first of its triangular side lobe fixed with its vertex angle equal to 70° and the variable side lobes has vertex angles varying as 80° and 90°. All the structural parameters were kept same as previous subsections other than following two refer fig. 4.11.

(a) θ_1 = 70° resulting in dimension 'a' equal to 60.6 nm.

(b) θ_2 is varied as 80° and 90° and dimension 'b' varies proportionally.

Out of two nanostructures considered in this subsection the first had θ_1 = 70° and θ_2 = 80° as vertex angles of the two triangular side lobes resulting into electric field intensity enhancement of 67.9 at resonant wavelength of 720.93 nm while the second bowtie nanostructure with vertex angle of variable triangular side lobe θ_2 equal to 90° provided electric field intensity enhancement maxima of 48.2 at resonant wavelength equal to 746.988 nm, refer fig. 4.19 (a), (b) respectively.

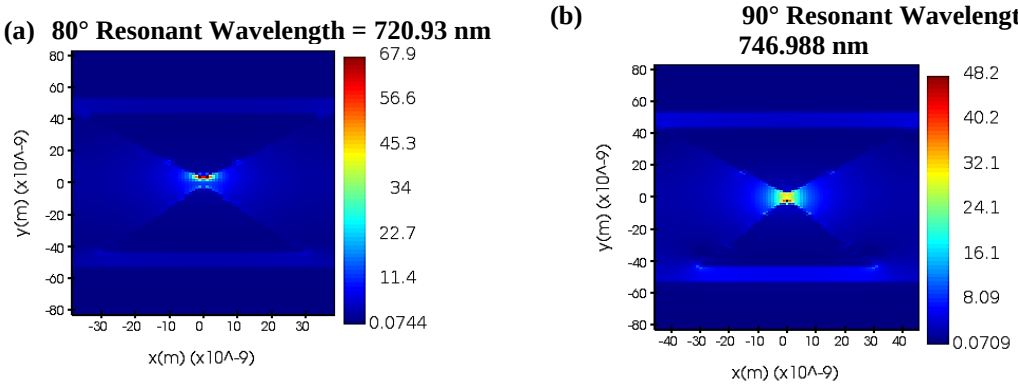

Figure 4.18 Enhancement of electric field intensity by bowtie with first triangular side lobe nanostructures with vertex angle 70° and second with variable vertex angle (a) 80°, (b) 90°

All these results derived in this subsection may be polished off as following table:

First triangle vertex angle (θ_1)	Second triangle vertex angle (θ_2)	Electric Field Enhancement	Enhancement Factor	Resonant Wavelength
70°	80°	67.9	2.13×10^7	720.93
70°	90°	48.2	5.40×10^6	746.988

Table 4.9 Results of bowtie with first triangular side lobe nanostructure with vertex angle $\theta_1 = 70°$ and second with variable vertex angle $\theta_2 =$ (a) 80°, (b) 90°

The nanostructures considered in this subsection provided a maximum electric field enhancement factor of 67.9 and wavelength of 720. 93 nm with two vertex angles $\theta_1 = 70°$ and $\theta_2 = 80°$ of the edges of triangular nanostructures facing each other. Electric field enhancement provided in this subsection was not at par with those obtained from the configurations of subsection 4.3.3 considering triangular nanostructures with $\theta_1 = 20°$ as vertex angles.

4.3.9 Array of asymmetric Bowtie with $\theta_1 = 80°$ and $\theta_2 = 90^0$

As all the possible bowtie nanostructures with variable vertex angles two triangular side lobes are already covered in previous subsections 4.3.3 to 4.3.8, the only configuration left to be considered is with vertex angles of the edges of triangular nanostructures facing each other as $\theta_1 = 80°$ and $\theta_2 = 90°$. All the structural parameters which were maintained in previous subsections will be maintained in this subsection with following two differences:

(a) $\theta_1 = 80°$ resulting in dimension ‘a’ equal to 72.6 nm.

(b) $\theta_2 = 90°$ and dimension ‘b’ equal to 86.6 nm.

This structural configuration of nanostructure provided a maximum electric field enhancement tractor equal to 76.1 at resonant wavelength of 720.93 nm. Refer fig. 4.20.

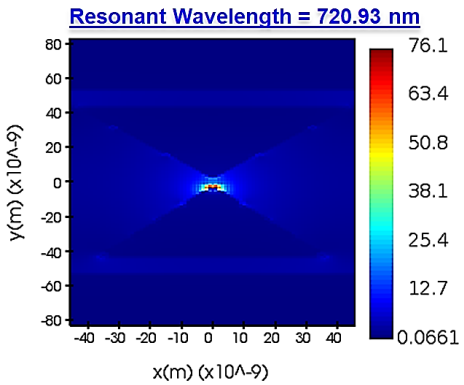

Figure 4.19 Enhancement of electric field intensity by bowtie with first triangular side lobe nanostructures with vertex angle 80° and second with vertex angle 90°

The result may be written into tabular form as in table 4.10:

First triangle	Second triangle	Enhancement	Wavelength
80°	90°	76.1	720.93

Table 4.10 Results of bowtie with first triangular side lobe nanostructure with vertex angle 80° and second with vertex angle 90°,

The bowtie nanostructure considered in this subsection provided enhancement factor of 76.1 which was better than those provided by nanostructures considered in previous three subsections 4.3.6, 4.3.7 and 4.3.8. This higher enhancement of electric field intensity was due to the bigger dimensions of the triangular nanostructures of the bowtie which facilitated collection of more electric field lines by nanostructures.

4.3.10 Results and observations: Asymmetric bowtie nanostructure

In last two sections 4.2 and 4.3 a total of 36 symmetric and asymmetric bowtie nano-structures were analyzed, out of which eight were symmetric and twenty eight were symmetric nano-structures. In symmetric bow tie configuration the highest enhancement factor of electric field equal to 1.07 X 10^7 was achieved by the bowtie with 20^0 as its vertex angle of both triangular nanostructures. This was attributed to efficient convergence of the electric filed lines. On analysis of asymmetric bowtie structures it was observed that highest electric field enhancement of 3.52 X 10^8 was achieved by an asymmetric bowtie with two of its triangular nanostructures having vertex angles equal to 20° and 60°. The results of all these 36 bowtie nano-structures are brought together in tabular form as table 4.11.

Sl.no.	Vertex angle of Triangle1 (θ_1)	Vertex angle of Triangle2 (θ_2)	Highest electric field enhancement	Enhancement Factor	Resonant wavelength (nm)
1.	20°	20°	57.2	1.07×10^7	696.629
2.	20°	30°	91.5	7.01×10^7	720.93
3.	20°	40°	111	1.52×10^8	775
4.	20°	50°	46.9	4.84×10^6	652.632
5.	20°	60°	137	3.52×10^8	775
6.	20°	70°	60.4	1.33×10^7	632.653
7.	20°	80°	61.5	1.43×10^7	652.632
8.	20°	90°	70.4	2.46×10^7	652.632
9.	30°	30°	51	6.77×10^6	746.988
10.	30°	40°	75.8	3.30×10^7	632.653
11.	30°	50°	48.7	5.62×10^6	720.93
12.	30°	60°	91.4	6.98×10^7	632.653
13.	30°	70°	49.3	5.91×10^6	953.846
14.	30°	80°	57.5	1.09×10^7	720.93
15.	30°	90°	55.1	9.22×10^6	652.632
16.	40°	40°	36.8	1.83×10^6	720.93
17.	40°	50°	74.5	3.08×10^7	746.988
18.	40°	60°	59	1.21×10^7	596.154
19.	40°	70°	83.1	4.77×10^7	746.988
20.	40°	80°	88.2	6.05×10^7	746.988
21.	40°	90°	101	1.04×10^8	746.988
22.	50°	50°	41.7	3.02×10^6	673.913
23.	50°	60°	48.4	5.49×10^6	720.93
24.	50°	70°	48.3	5.44×10^6	673.913

25.	50°	80°	65.2	1.81 X 10^7	720.93
26.	50°	90°	66.2	1.92 X 10^7	673.913
27.	60°	60°	48.5	5.53 X 10^6	696.629
28.	60°	70°	40.7	2.74 X 10^6	696.629
29.	60°	80°	67.4	2.06 X 10^7	720.93
30.	60°	90°	53.8	8.38 X 10^6	696.629
31.	70°	70°	48.9	5.72 X 10^6	873.239
32.	70°	80°	67.9	2.13 X 10^7	720.93
33.	70°	90°	48.2	5.40 X 10^6	746.988
34.	80°	80°	70.1	2.41 X 10^7	746.988
35.	80°	90°	76.1	3.35 X 10^7	720.93
36.	90°	90°	53	7.89 X 10^6	673.913

Table 4.11 Consolidated results of array of bowtie (Color-codes: Grey: Array of Symmetric Bowtie nanostructures; White: Array of Asymmetric Bowtie nanostructures; Green: Configuration with highest enhancement factor)

From the above table it may be concluded that the highest electric field intensity enhancement of 137 and highest enhancement factor equal to 3.52 X 10^8 was provided by bowtie with two triangular nanostructures having vertex angles of edges facing each other as $\theta_1 = 20°$ and $\theta_2 = 60°$ at a resonant wavelength of 775 the second best combination of $\theta_1 = 20°$ and $\theta_2 = 40°$ provided electric field enhancement factor equal to 1.52 X 10^8 at same resonant wavelength while the third highest electric field intensity enhancement of 101 and an enhancement factor of 1.04 X 10^8 was provided by a combination of triangular nanostructures of the bowtie with vertex angles of edges facing each other equal to $\theta_1 = 40°$ and $\theta_2 = 90°$ at resonant wavelength equal to 746.988 nm.

Beside these nanostructural configurations there were two more configurations which provided enhancement factor electric field intensity greater than 90 and two provided electric field intensity enhancement greater than 80. All these results are represented in graphical form in Fig. 4.21

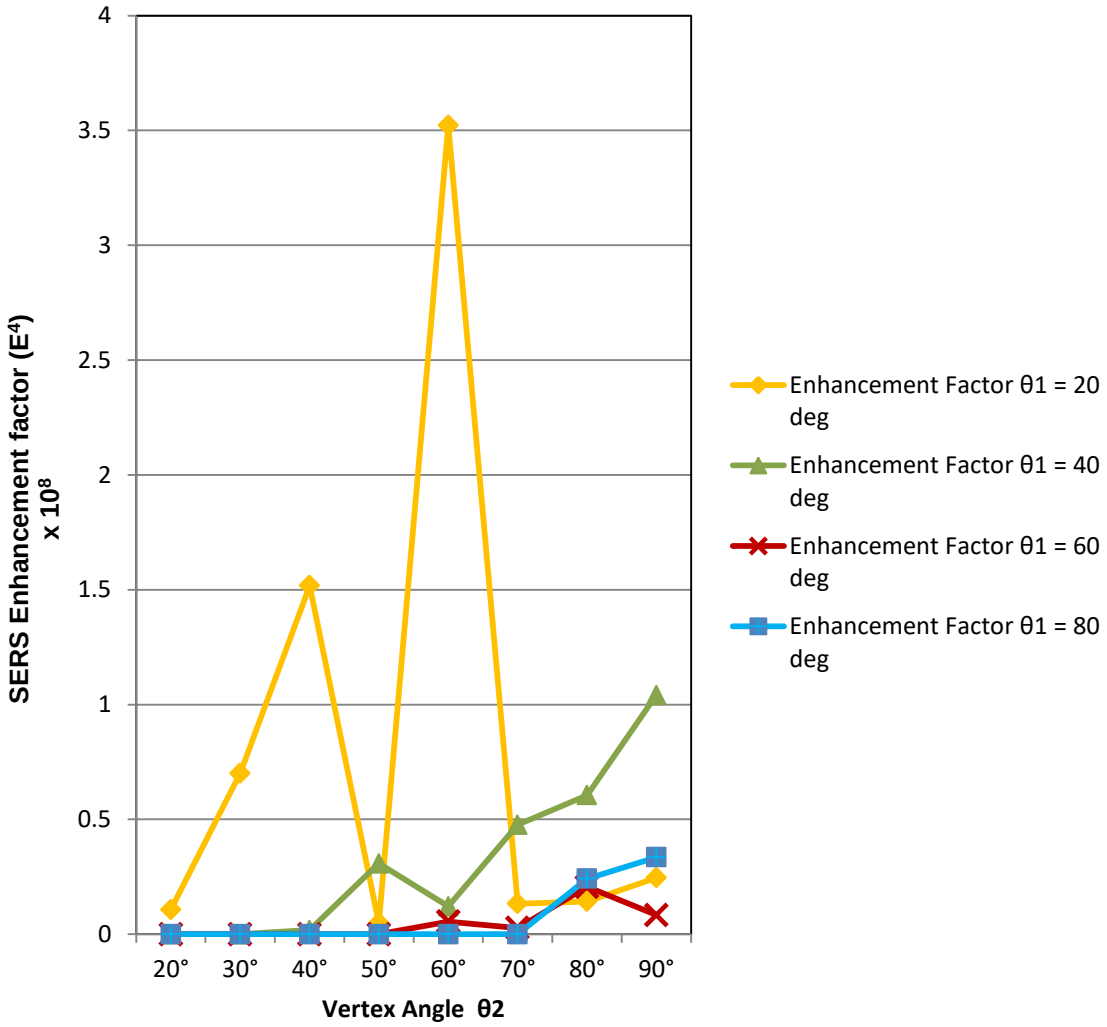

Figure 4.20 Graphical representation of enhancement factors obtained from all the bowtie nanostructures.

The simulations in this were carried out with variation of vertex angles and corresponding base length ‘a’ and ‘b’ of triangular nanostructures were varied, keeping rest of the structural parameters constant for all the 36 nano-structural configurations refer Fig. 4.11. Therefore the number of factors which contributed towards variation of electric field enhancement now reduced from five (as mentioned in section 4.1.7) to one i.e. base length ‘a’ and ‘b’ of triangular nanostructures, thus removing all the ambiguities about contributing factor towards electric field enhancement.

CHAPTER 5

ARRAY OF TRIANGULAR NANO-PLATES MOVING SIDEWAYS

In this chapter the probability of obtaining better enhancement factor by moving the bowtie lobes sideways is explored. As in Chapter 4 where symmetric configurations of bowtie nanostructures were studied it was found that a nano bowtie structure with 20° angle on each side has got the highest electric field intensity enhancement of 57.2 for acute angle triangular bowtie configurations, therefore the same structure is used for analysis in this chapter. Before moving ahead it may be noted that two of the tree side walls of the triangular side lobe is 44 nm long (refer fig. 5.1) and sideways stacking being mentioned in the following subsections is with respect to these 44nm long side walls. The triangular nanostructure being considered till now will be called as triangular nano-plate in this chapter and not triangular side lobes because the bowtie structure will not be maintained in this chapter. The edges of the nano-plates facing each other had vertex angle of 20° and were moved sideways while maintaining their orientation providing four structural arrangements, which are given below:

(a) Edges Face to face.

(b) Vertices side by side.

(c) Half Overlapped Sideways.

(d) Complete sideways overlap.

5.1 STRUCTURAL DETAILS

With this kind of nanostructural arrangements it is not feasible to solely vary position of triangular nano-plates and keep rest of the nanostructures like nano-gratings and base unaltered because gaps between different nanostructures are also to be maintained as were defined in previous chapters. Therefore the parameters which were

standardized in previous sections will be maintained in this section too and are listed below:

(a) The nanostructure is maintained symmetric about Axis passing though point 0,0,0 perpendicular to xy plane for all the nano structural configurations considered.

(b) All the nano-structures are arranged in XY plane and iteratively extended in both directions to create an array.

(c) Observations were made on a bandwidth of 600 nm ranging from 400 nm to 1000 nm.

(d) Smallest gap between nano-structures (triangular nanostructures) is g=5nm

(e) The nano-gratings are kept at a gap of 10nm from the nano structure.

(f) The duty cycle or filling factor of the grating varies as per the nano structure, but linear rectangular grating iterates in y direction with following properties:

(i) Grating depth=50 nm

(ii) Grating period varies= 60 + gap between grating walls (depends on amount of overlap)

(iii) Filling factor= 60/(grating period)

(a) Vertex angles of the edges of triangular nano-plates facing each other are equal to 20° i.e. $\theta_1 = \theta_2 = 20°$.

(b) Thickness of all nano-structures is 50 nm.

(c) All the nano-structures are deposited on a rectangular base of thickness 50 nm.

(d) Material of all nano structures is gold (Au(CRC)).

(e) The source is maintained above the nano-structure at a distance of 20 nm from it, at (0,0,45) in Cartesian coordinates.

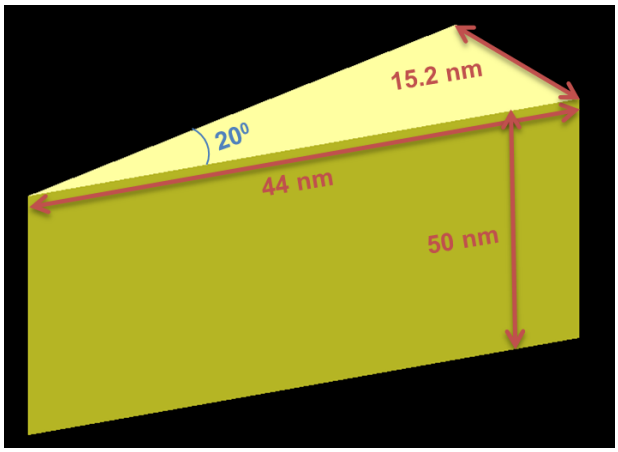

Figure 5.1 Dimensions of triangular nano-plate

All these parameters will be implemented in the following sections and nano-structural arrangements considered in them, which are shown in the **fig.s 5.2, 5.4, 5.6** in the respective subsections.

5.2 ANALYSIS

The analysis of the performance of the four configurations mentioned in the beginning of this chapter will be performed in the following sections. Made in measurement structures are covered in subsequent sections:

5.2.1 Triangular Nano-plates with Edges Face to Face

This configuration is similar to the configuration already analyzed in the chapter 4 section 4.2, in which symmetric triangular bowtie structure was studied. In this arrangement the triangular nano-plates are positioned such that the gap between the edges facing each other is 5 nm. The distance of triangular nano-plates from grating walls is maintained equal to 10 nm. The thickness of nano-plates is 50 nm. Grating walls are 60 nm wide, 50 nm thick and 20.2 nm long. This structure is iterated in x and y direction to create an array. The base substrate, on which this nanostructural arrangement is mounted,

is 50 nm thick. The structural arrangement of face to face triangular nanostructures may be understood from Fig. 5.2.

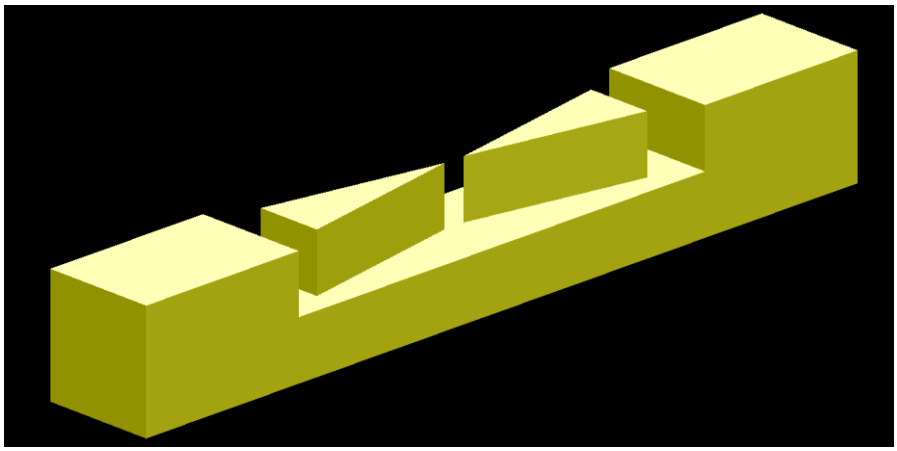

Figure 5.2 Triangular Nano-plates with Edges Face to face

In this nanostructural arrangement the sharp edges of the nanostructures point towards each other which results into effective convergence of the electric field lines and hence as good electric field enhancement is achieved as depicted in fig. 5.3.

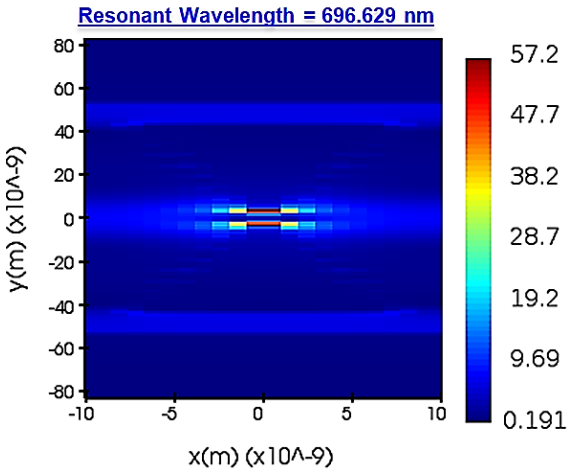

Figure 5.3 Electric field enhancement produced by triangular nano-plates with edges face to face

This structure produced a maximum electric field enhancement of 57.2 and an enhancement factor of 1.07 x 10^7 at resonant wavelength of 696.629 nm. in next section the distance between the edges will be maintained as same as in this section but the edges will not be facing each other but will be aligned sideways.

5.2.2 Triangular Nano-plates with Vertices Side by Side Along X-Axis

In this configuration the vertices were made to align with each other sideways along x-axis at a gap of 5 nm. In this arrangement of nanostructure the grating walls were moved closer to each other by 5 nm, thus having following properties:

(g) Grating depth=50 nm

(h) Grating period = 60 +106.6= 166.6nm

(i) Filling factor= 60/166.6= 0.36

All these parameters may be more clearly understood using the fig. 5.4.

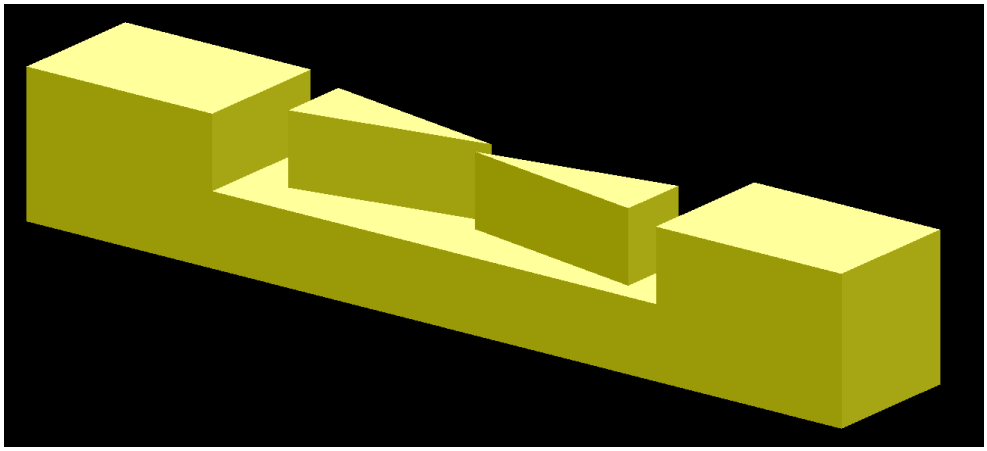

Figure 5.4 Triangular Nano-plates with Vertices side by side along x axis

The edges of the triangular nano plates are not linearly aligned in this case but are laterally aligned refer fig. 5.4. an appreciable increase in electric field enhancement was observed with tis structural arrangement. The enhancement of electric field was by a factor of 75 with arrangement as compared to 57.2 achieved with linearly arranged edges of triangular nano-plates.

Enhanced electric field obtained from the simulations are shown in fig. 5.5. This structure provided a maximum electric field intensity enhancement of 75 and an enhancement factor of 3.1.x 10 ^7 at resonant wavelength of 746.988 nm.

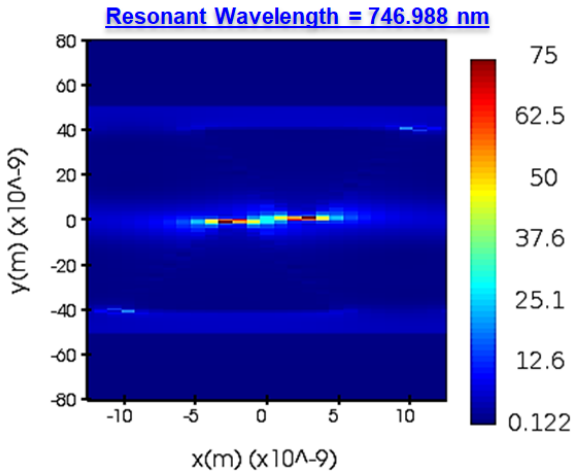

Figure 5.5 Electric field enhancement produced by triangular nano-plates with vertices side by side along x axis

The enhancement factor obtained in this section was almost three times larger than that obtained in section 5.2.1.

5.2.3 Triangular Nano-plates Half Overlapped Sideways

In this structural arrangement the triangular nanostructures overlapped with each other sideways such that half of the first triangular nanostructure lays by the second triangular nanostructure by 22 nm. Therefore this arrangement reduced the overall length of nanostructure by 44 nm as compared to nanostructure considered in previous subsection. However the point to ponder here is that a minimum gap of 5nm is maintained in between the two triangular nanostructures. Thus moving the grating walls closer to each other by 44 nm, the grating had following properties:

(j) Grating depth=50 nm

(k) Grating period = 60 +86= 146nm

(l) Filling factor= 60/146= 0.41

The nanostructural arrangement may be more clearly understood from Fig. 5.6.

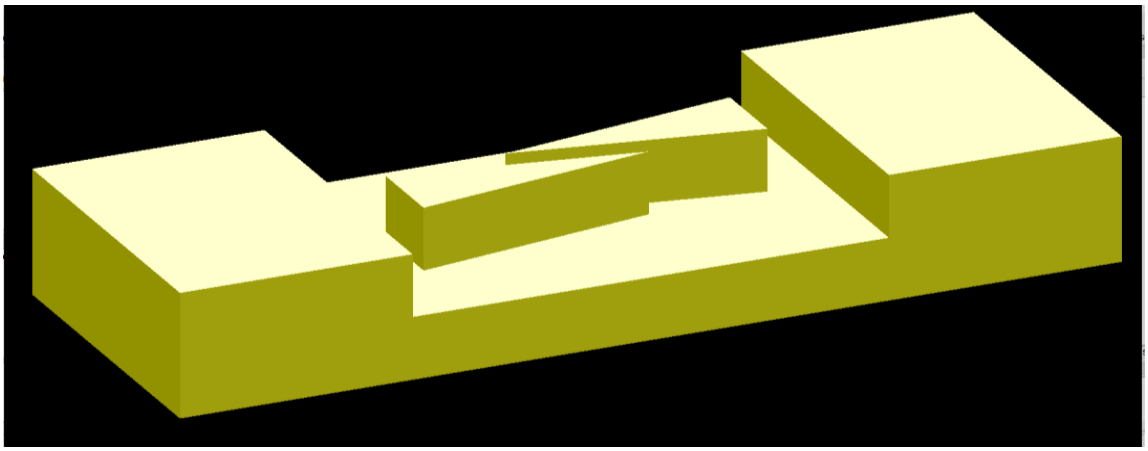

Figure 5.6 Triangular Nano-plates Half Overlapped Sideways

This structure provided a maximum electric field intensity enhancement of 19.1 and an enhancement factor of 1.3x 10^5 at resonant wavelength of 775nm. But this enhancement was not at the sharp edges but in between the grating walls and triangular nanostructures.

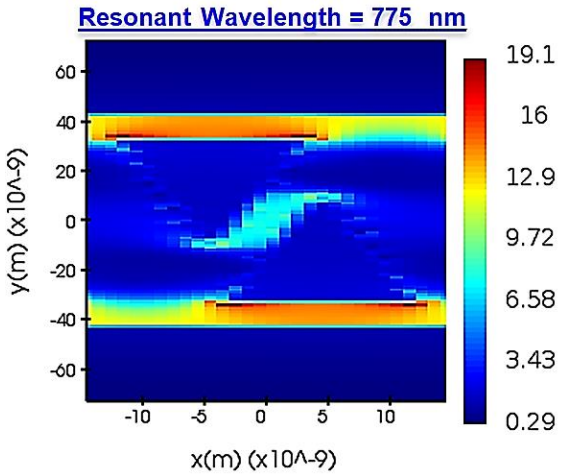

Figure 5.7 Electric field enhancement produced by triangular nano-plates half stacked sideways

5.2.4 Triangular Nano-plates Sideways Stacked Completely

In this section the triangular nano-plates are stacked sideways for the complete length of sidewalls of 44nm while maintaining a minimum gap of 5nm in between the sidewalls. This structural arrangement of nano-plates further reduced the overall length of the nanostructure by 44 nm as compared to that of subsection 5.2.3. The grating had following features in this considered nanostructure:

(m) Grating depth=50 nm

(n) Grating period = 60 +63.3= 123.3nm

(o) Filling factor= 60/123.3= 0.49

All these parameters may be more clearly understood using the fig. 5.8

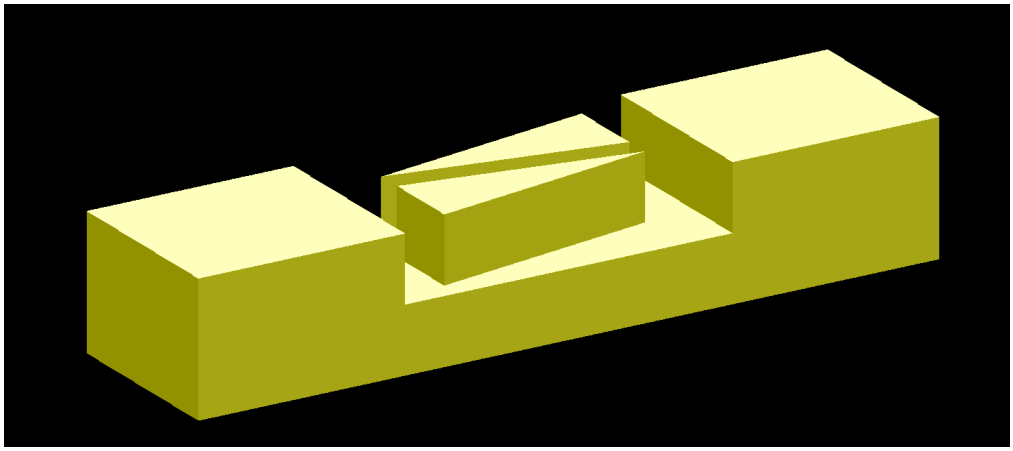

Figure 5.8 Triangular nano-plates sideways overlapped completely

This structure provided a maximum electric field intensity enhancement of 30 and enhancement actor of 0.8 x 10^6 at resonant wavelength of 720.93nm as shown in fig. 5.9.

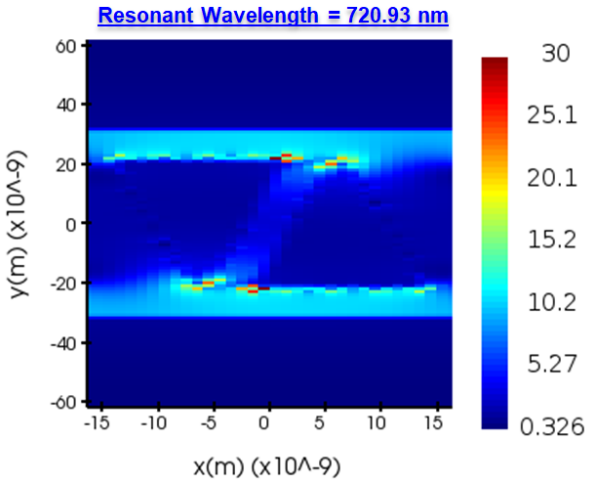

Figure 5.9 Electric field enhancement produced by triangular nano-plates sideways overlapped completely

The enhancement factor achieved in this structural arrangement was almost six times larger than that achieved in section 5.2.3.

The results obtained from an array of sideways moving triangular nanostructures in between the iterating nano-gratings of thickness 60 nm are summarized in Table 5.1:

Sl.no.	**Mutual arrangement of two triangular nanostructures**	**Highest Electric Field Enhancement**	**Enhancement Factor**	**Resonance wavelength (nm)**
1.	Edges Face to face	57.2	1.07 x 10^7	696.629
2.	Vertices side by side along x axis	75	3.16 x 10^7	746.988
3.	Half Overlapped Sideways	19.1	1.33 x 10^5	775
4.	Sideways Overlapped Completely	30	8.10 x 10^5	720.93

Table 5.1 Analysis of array of symmetric bowtie with its triangular side lobes moving sideways.

From the above table it may be inferred that when the triangular nanostructures are moved side by side to each other no significant electric field enhancement is observed except when the vertices of the sharp edges of the triangular nano-plates are lying side by side along x-axis, providing a significant increase in electric field intensity enhancement from 57.2 to 75 with a red shift of about 50 nm in resonant wavelength.

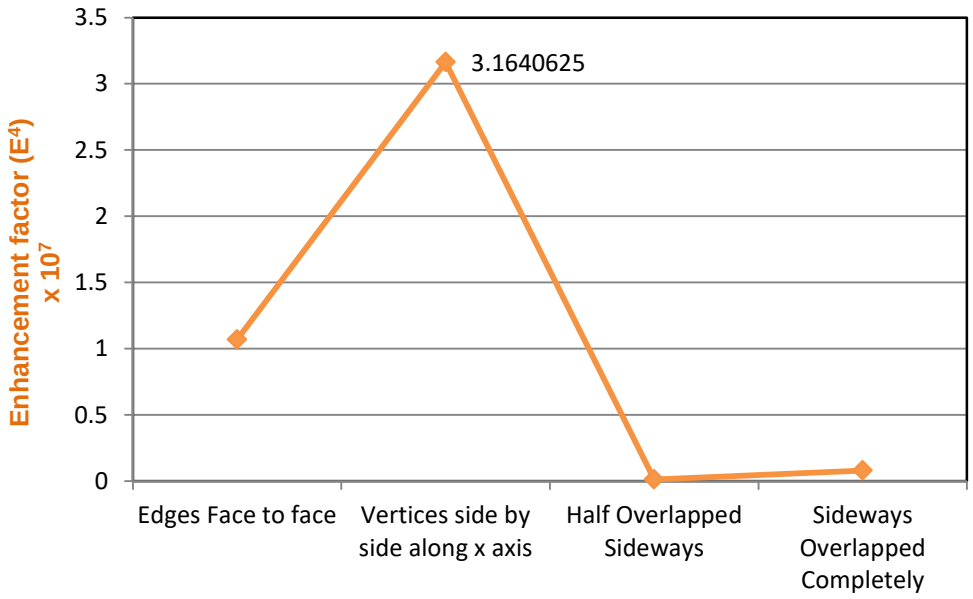

Figure 5.10 Graphical representation of Enhancement factor obtained from array of Sideways stacked triangular nano-plates with vertex angle = 20^0.

From Fig. 5.10 it may be derived that the highest enhancement factor of 3.1 x 10^7 was obtained from the nanostructural arrangement of triangular nano-plates with their edges aligned sideways next to each other. In next subsection 5.2.5 the nanostructural arrangement *"with edges of the triangular nano-plates aligned side by side will be applied to the asymmetric bowtie nanostructure analyzed in Subsection 4.3.3 which provided highest electric field enhancement till this point in this work*" to check if this arrangement enhances electric field intensity in that or not.

5.2.5 Triangular Nano-plates with vertex angles 20^0 and 60^0 positioned with Vertices Side by Side Along X-Axis

In last four sections it was observed that the highest electric field intensity enhancement was obtained from two triangular nano-plates kept next to each other with their vertices aligned sideways, i.e., along x-axis when the nano-plates are aligned in y direction. In this subsection similar nanostructural arrangement was applied on the asymmetric bowtie nanostructure with side lobes having vertex angle equal to 20^0 and 60^0, providing electric field intensity enhancement of 137 (analyzed in Subsection 4.3.3). The structural arrangement of this configuration is shown in the Fig. 5.11.

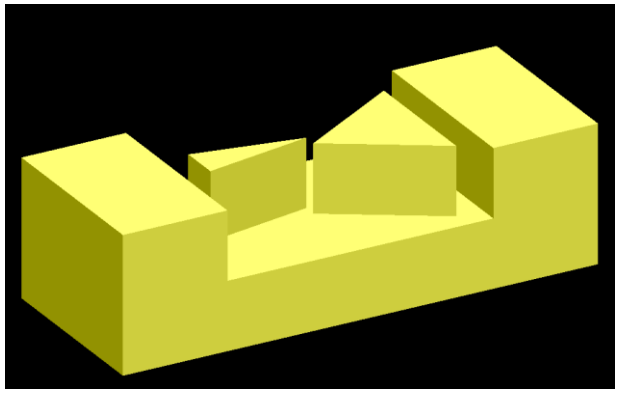

Figure 5.11 Schematic diagram of triangular nano-plates with vertex angles 20^0 and 60^0 positioned with vertices side by side along x-axis

During analysis of this structural arrangement it was observed that instead of increase in electric field enhancement which was observed in symmetric bowtie configuration the enhancement of electric field was hugely reduced by more than half, from 137 to 52.7. The structural arrangement shown in fig 5.11 provided an electric field intensity enhancement by a factor of 52.7 refer fig. 5.12.

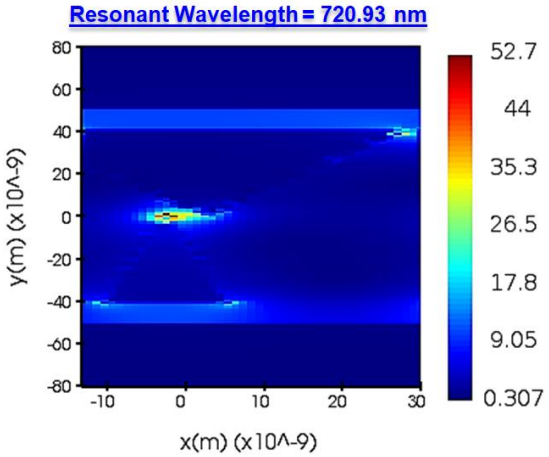

Figure 5.12 Electric field enhancement produced by triangular nano-plates with vertex angles 20^0 and 60^0 positioned with vertices side by side along x-axis

5.3 observations

Therefore this chapter may be concluded with remarks that the best nano structural configuration obtained in this chapter was the one analyzed in section 5.2.2 providing highest electric field enhancement of 3.16 x 10^7.

CHAPTER 6

V-GROOVE BOWTIE NANOSTRUCTURE

In the V-groove bowtie nanostructure as the name suggests one of the triangular side lobes of the bowtie, preferably with larger vertex angle (60° in this work) has v-groove in it and the vertex angle of second triangular side lobe is varied as 20°, 30°, 40°, 50° and 60° to examine the effect on enhancement factor. In this this chapter the second triangular side lobe of bow tie may be referred as triangular nano-plate.

In such nanostructural configurations lobes, there will be three spatial arrangements for each combination of two side, these arrangements are listed below:

(a) Configuration 1. Edge of triangular nano-plate 5 nm away from the edges of the V-groove (refer Fig. 6.1(a)).

(b) Configuration 2. Edge of triangular nano-plate lies in between the V-groove, edges aligned along x-axis(refer Fig. 6.1(b)).

(c) Configuration 3. Edge of triangular nano-plate 5nm inside the V-groove (refer Fig. 6.1(c)).

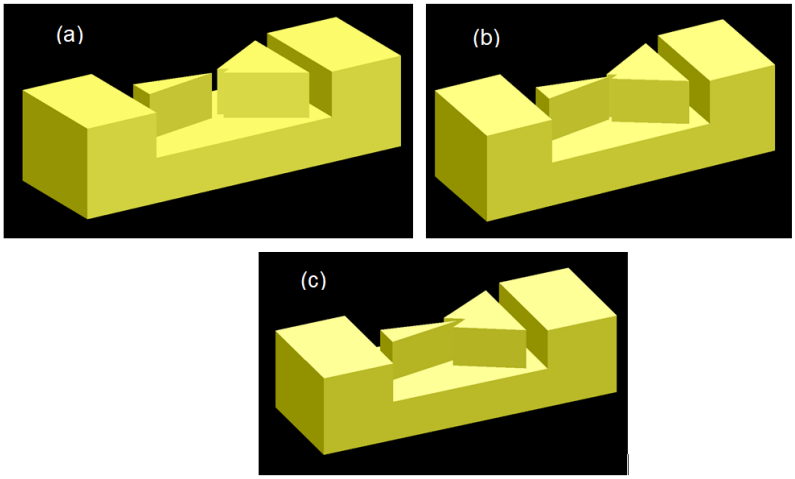

Figure 6.1 Three V-groove Configurations (a) Configuration 1: 5 nm away from the edges of the V-groove. (b) Configuration 2: In between the V-groove, edges aligned along x-axis. (c) Configuration 3: 5nm inside the V-groove.

6.1 ANALYSIS

The analysis of three V-groove structural configurations was conducted by considering the triangular nanostructure with V-groove bearing vertex angle equal to 60° and second triangular nanostructure was varied with its vertex angle from 20° to 60°. These nanostructural configurations may be divided into five categories depending upon the vertex angle of the triangular nano-plate. These five categories and in turn all fifteen nanostructures will be covered in the following subsection.

6.1.1 Triangular nanostructure with vertex angle = 20°

(a) Configuration 1. In this configuration the edge of the triangular nano-plate with vertex angle 20° is 5 nm away from the edges of the V-groove triangular nanostructure with vertex angle equal to 60^0. This provided a maximum electric field enhancement of 133 at a resonant wavelength of 775 nm.

(b) Configuration 2. In this structural arrangement triangular nanostructure with vertex angle 20° has its vertex or edge in between the V-groove edges, with all three edges aligned along the x-axis. The structural arrangement provided a maximum electric field enhancement factor of 112 resonator wavelength of 696.629 nm.

(c) Configuration 3. The edge with 20° vertex angle of triangular nano-plate lies 5nm inside the V-groove. This resulted in a maximum electric field enhancement of 84.5 at resonant wavelength of 746.988 nm.

6.1.2 Triangular nanostructure with vertex angle = 30°

(a) Configuration 1. In this configuration the edge of the triangular nano-plate with vertex angle 30° is 5 nm away from the edges of the V-groove triangular nanostructure with vertex angle equal to 60^0. This provided a maximum electric field enhancement of 90.3 at a resonant wavelength of 632.653 nm.

(b) Configuration 2. In this structural arrangement triangular nanostructure with vertex angle 30° has its vertex or edge in between the V-groove edges, with all three edges aligned along the x-axis. The structural arrangement provided a maximum electric field enhancement factor of 78.2 resonant wavelength of 632.653 nm.

(c) Configuration 3. The edge with 30° vertex angle of triangular nano-plate lies 5nm inside the V-groove. This resulted in a maximum electric field enhancement of 51.2 at resonant wavelength of 746.988 nm.

6.1.3 Triangular nanostructure with vertex angle = 40°

(a) Configuration 1. In this configuration the edge of the triangular nano-plate with vertex angle 40° is 5 nm away from the edges of the V-groove triangular nanostructure with vertex angle equal to 60^0. This provided a maximum electric field enhancement of 58.8 at a resonant wavelength of 596.194 nm.

(b) Configuration 2. In this structural arrangement triangular nanostructure with vertex angle 40° has its vertex or edge in between the V-groove edges, with all three edges aligned along the x-axis. The structural arrangement provided a maximum electric field enhancement factor of 66.1 resonant wavelength of 775 nm.

(c) Configuration 3. The edge with 40° vertex angle of triangular nano-plate lies 5nm inside the V-groove. This resulted in a maximum electric field enhancement of 54.2 at resonant wavelength of 775 nm.

6.1.4 Triangular nanostructure with vertex angle = 50°

(a) Configuration 1. In this configuration the edge of the triangular nano-plate with vertex angle 50° is 5 nm away from the edges of the V-groove triangular nanostructure with vertex angle equal to 60^0. This provided a maximum electric field enhancement of 43.6 at a resonant wavelength of 720.93 nm.

(b) Configuration 2. In this structural arrangement triangular nanostructure with vertex angle 50° has its vertex or edge in between the V-groove edges, with all three edges aligned along the x-axis. The structural arrangement provided a maximum electric field enhancement factor of 52 resonant wavelength of 775 nm.

(c) Configuration 3. The edge with 50° vertex angle of triangular nano-plate lies 5nm inside the V-groove. This resulted in a maximum electric field enhancement of 65 at resonant wavelength of 720.93 nm.

6.1.5 Triangular nanostructure with vertex angle = 60°

(a) Configuration 1. In this configuration the edge of the triangular nano-plate with vertex angle 60° is 5 nm away from the edges of the V-groove triangular nanostructure with vertex angle equal to 60^0. This provided a maximum electric field enhancement of 43.4 at a resonant wavelength of 720.93 nm .

(b) Configuration 2. In this structural arrangement triangular nanostructure with vertex angle 60° has its vertex or edge in between the V-groove edges, with all three edges aligned along the x-axis. The structural arrangement provided a maximum electric field enhancement factor of 62 resonant wavelength of 746.988 nm.

(c) Configuration 3. The edge with 60° vertex angle of triangular nano-plate lies 5nm inside the V-groove. This resulted in a maximum electric field enhancement of 32.9 at resonant wavelength of 673.913 nm.

6.1.6 Results and Observations

In this chapter till now different configurations of triangular nanostructures with variable vertex angle from 20^0 to 60^0 were analyzed by placing it against triangular nanostructure with V-groove at the edge facing the first triangular nanostructure. These structures were analyzed for electric field enhancement. All these combinations of nanostructures were studied for three configurations of spatial arrangements.

The results of these three spatial configurations with all structural combinations and respective enhancement factor and resonant wavelengths are given in Table 6.1.

Configuration	**Triangle1 with v-groove**	**Triangle2**	**Highest Electric Field Intensity**	**Resonance wavelength**
Configuration 1	60	20	133	775
Configuration 2	60	20	112	696.629
Configuration 3	60	20	84.5	746.988
Configuration 1	60	30	90.3	632.653
Configuration 2	60	30	78.2	632.653
Configuration 3	60	30	51.2	746.988
Configuration 1	60	40	58.8	596.154
Configuration 2	60	40	66.1	775
Configuration 3	60	40	54.2	775
Configuration 1	60	50	43.6	720.93
Configuration 2	60	50	52	775
Configuration 3	60	50	65	720.93
Configuration 1	60	60	43.4	720.93

Configuration	Triangle1 with v-groove	Triangle2	Highest Electric Field Intensity	Resonance wavelength
Configuration 2	60	60	62	746.988
Configuration 3	60	60	32.9	673.913

Table 6.1 Analysis of V-groove structural arrangements

On basis of the study carried out in this section it may be noted that no significant increase in electric field enhancement was observed by using the V-groove structure in either of the three configurations.

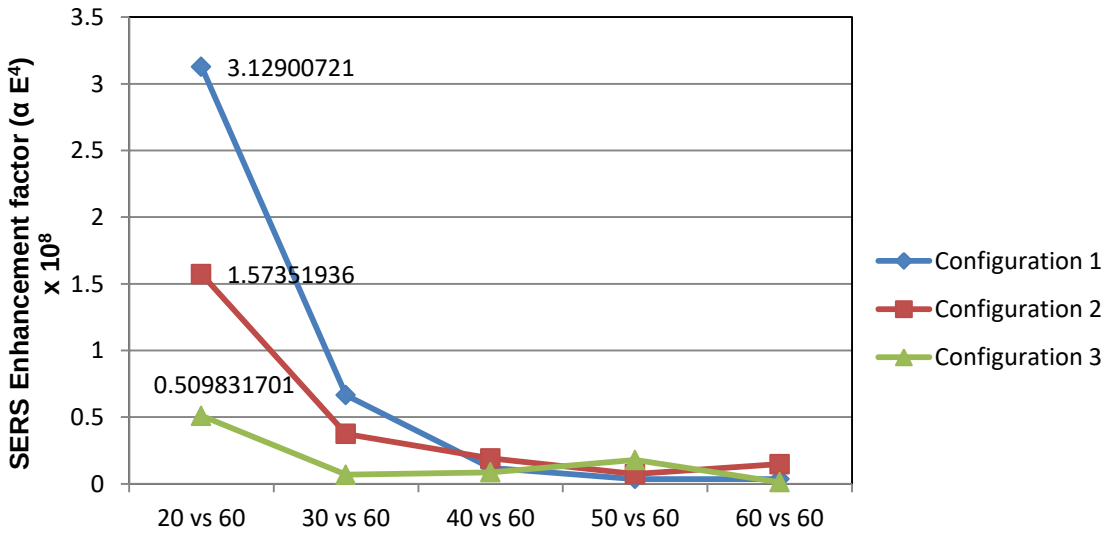

Figure 6.2 Graphical representation of enhancement factor obtained from array of triangular nano-plate and V-groove triangular nanostructure with 60 nm wide nano-gratings arranged in three structural configurations.

The maximum electric field enhancement which was obtained with the combination of 20^0 vertex angle triangular nano-plate and a 60^0 triangle structure with V-groove was 3.1x 10^8 at a resonance wavelength of 775 nm. This is observed that the maximum electric field intensity obtained from this configuration was 133 at resonance wavelength of 775 nm. Thus this section may be concluded with the remark that groove

structures though provided a high enhancement factor of 3.1x 10^8 but still the highest electric field enhancement obtained till now is from array of bowtie having triangular nanostructures with 20° and 60^0 as vertex angle (refer section 4.3.3).

6.2 TRIDENT STRUCTURE VS V-GROOVE NANO STRUCTURES

In this section a trident constituting of three triangular prongs with vertex angle equal to 20^0 was positioned at place of single triangular nano-plate in previous section against a V-groove triangular Nano structure. The structural details may be understood more easily with the help of the Fig. 6.2.

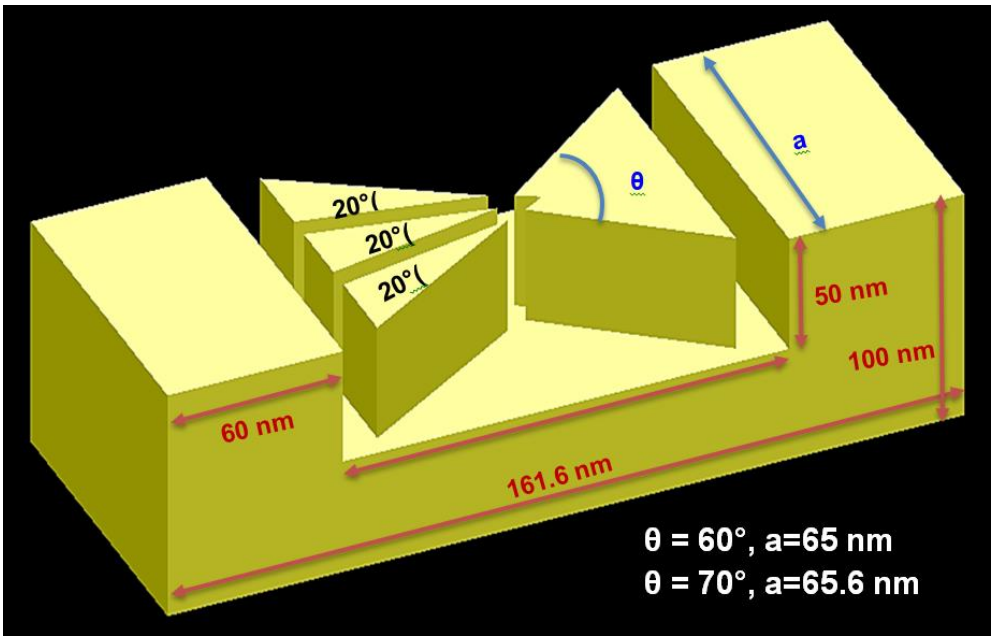

Figure 6.3 Schematic diagram of trident structure vs v-groove nano structures

6.2.1 Structural Details

In analysis part two bowtie in nanostructures will be considered and analysed for electric field intensity enhancement.

(d) These two Nano structures will be as follows:

(e) Trident structure with 20° prongs vs v-groove on 60° triangular nanostructure.

(f) Trident structure with 20° prongs vs v-groove on 70° triangular nanostructure.

The structural parameters considered in previous nanostructures in past sections will be maintained in this section also, these standard structural parameters are as follows:

(g) All the nano-structures are arranged in XY plane and iterated to create a periodic array in both directions.

(h) Observations were made on a bandwidth of 600 nm ranging from 400 nm to 1000 nm.

(i) The grating walls are kept at 10nm from the bowtie nanostructure.

(j) The duty cycle of the nano-gratings is 36% iterating in y direction with following properties:

(k) Grating depth=50 nm

(l) Grating period = 60 +106.6= 166.6nm

(m) Filling factor= 60/166.6= 0.36

(n) Base length of the triangular nanostructure 'a' is varied in correspondence with vertex angles θ and can be defined as:

(o) a=65 nm, θ =60°

(p) a=65.6 nm, θ =70°

(q) Thickness of all nano-structures is 50 nm.

(r) All the nano-structures are deposited on a rectangular base of thickness 50 nm.

(s) Material of all nano structures and base substrate is gold (Au(CRC)).

(t) The source is maintained above the nano-structure at a distance of 20 nm from it, at (0,0,45) in Cartesian coordinates.

6.2.2 Trident structure with 20° prongs pointing towards V-groove triangular nanostructure with vertex angle = 60°

In this structure of triangular nanostructure v groove has vertex angle equal to 60° making dimension 'a' (refer Fig. 6.2) equal to 65 nm, refer fig. 6.2. Structure provided an enhancement of electric field intensity by a factor of 133 at a resonant wavelength equal to 720.93. These results are elaborated using the following fig. 6.4.

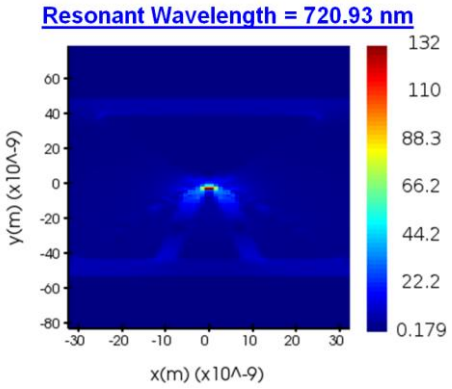

Figure 6.4 Electric field enhancement produced by trident structure with 20° prongs pointing towards v-groove on triangular nanostructure with vertex angle = 60°.

6.2.3 Trident structure with 20° prongs pointing towards v-groove on triangular nanostructure with vertex angle = 70°

In this subsection the triangular structure considered is similar to the one which was considered in previous subsection but the only difference is that the vertex angle of triangular nanostructure with groove is increased from 60^0 to 70^0 resulting into corresponding increment in dimension 'a' (refer Fig. 6.2) from 65 to 65.6 nm. In this nanostructure the highest electric field intensity enhancement obtained was 133 at resonant wavelength of 720.93 nm.

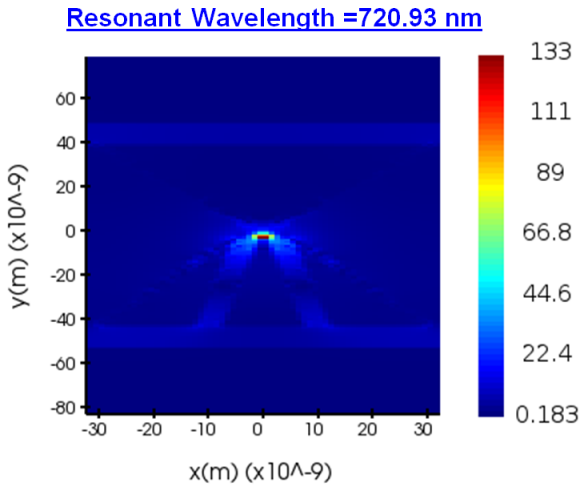

Figure 6.5 Electric field enhancement produced by trident structure with 20° prongs pointing towards v-groove on triangular nanostructure with vertex angle 70°.

6.2.4 Results and observations

From the analysis performed in this chapter, it was observed that triangular nanostructure with V-groove as analyzed in section 6.1.1 provided an enhancement factor same as that provided by the trident nanostructure analyzed in section 6.2.3 equal to 3.1×10^8. The trident structures analyzed in section 6.2.2 and 6.2.3 provided nearly equal electric field enhancement of 132 and 133 respectively.

CHAPTER 7

CONCLUSION AND FUTURE WORK

7.1 CONCLUSION

This thesis work started with introduction to basic concepts of optics namely scattering, Raman and Rayleigh scattering. This was followed by introduction to SPPs and different excitation techniques for SPPs in chapter 2. This was followed by an elaboration of the concept of Surface enhanced Raman spectroscopy along with different structures suitable for Surface enhanced Raman spectroscopy and different factors affecting SERS performance. Finally, in Chapter 2 applications of surface plasmon polaritons and calculation SERS enhancement factor were covered.

In chapter 3, dimers of spherical nanoparticles and dimers of ellipsoidal nanoparticles were analyzed for calculating the E-field enhancement. The effect of confining these dimers inside periodic nano-gratings was also analyzed. Additionally, it was understood how different orientations of these dimers effect the SERS enhancement. Chapter 4 was the most elaborative section of this work in which array of symmetric and asymmetric bowties were studied. In chapter 4, it was deduced that the array of asymmetric bowtie with vertex angles equal to 20°and 60° provided the highest electric fields intensity enhancement of ~137.

In chapter 5, analysis of the movement of triangular side lobes of symmetric bowtie sideways to each other was studied. Four nano-structural arrangements of symmetric bowtie elements were studied and it was concluded in chapter 5 that electric field was further enhanced by moving the edges of triangular nano-plates just besides each other. The same structural arrangement was used for analyzing the array of Asymmetric bowtie nanostructure which provided best electric field enhancement in Chapter 4, i.e, asymmetric bowtie with vertex angles equal to 20°and 60°. In chapter 6 bowties were analyzed with a groove in one of the triangular nanostructure and a

combination of trident with a triangular nanostructure with grove was also analyzed. From the analysis performed in this chapter, it was observed that both structural arrangements provided same electric field enhancement factor, which is equal to 3.1 x 10^8. It was observed that a maximum electric field intensity enhancement of 133 obtained in chapter 6 was still slightly lesser than that provided by simple asymmetric bowtie with triangular side lobes having vertex angles equal to 20° and 60° providing electric field enhancement of 137 i.e. an enhancement factor ~$3.5x10^8$.

Thus it is concluded that out of all the nanostructures considered in this work, the best enhancement was provided by the array of asymmetric bowtie with triangular nanostructures having vertex angles equal to 20° and 60° providing enhancement of the order of 137. The second highest enhancement was provided by V-groove structure of same vertex angles combinations and trident against V-groove configuration as covered in sections 6.1.1, 6.2.2 and 6.2.3.

7.2 FUTURE SCOPE

Different SERS substrates have been developed till date with improvised stability however economic manufacturing of re-employed sturdy, homogeneous and sizeable SERS substrates has always been an issue of concern. Few of the factors which may be considered in future to improvise this work are as follows:

(u) Scope of using cost effective substrate like paper may be exploited and analysis may be done for such substrates that, what are the effects of such substrate on hotspot, SERS intensity and enhancement factor.

(v) The scope of this work is kept limited to two dimensional array of nanostructures. The scope of adding third degree of freedom in SERS substrate by applying layers of such two dimensional arrays with different orientations may be analyzed. The three dimensional array with best enhancement factor may be explored and how this will improve enhancement factor and capability of analyte entrapping may be assessed.

REFERENCES

[1]. Jiao, Y., Ryckman, J. D., Koktysh, D. S., & Weiss, S. M. (2013). Controlling surface enhanced Raman scattering using grating-type patterned nanoporous gold substrates. *Optical Materials Express*, *3*(8), 1137-1148.

[2]. Offerhaus, H. L., Van Den Bergen, B., Escalante, M., Segerink, F. B., Korterik, J. P., & Van Hulst, N. F. (2005). Creating focused plasmons by noncollinear phasematching on functional gratings. *Nano letters*, *5*(11), 2144-2148.

[3]. Iqbal, T., Ashfaq, Z., Afsheen, S., Ijaz, M., Khan, M. Y., Rafique, M., & Nabi, G. (2020). Surface-Enhanced Raman Scattering (SERS) on 1D Nano-gratings. *Plasmonics*, 1-7.

[4]. Devaux, E., Ebbesen, T. W., Weeber, J. C., & Dereux, A. (2003). Launching and decoupling surface plasmons via micro-gratings. *Applied physics letters*, *83*(24), 4936-4938.

[5]. Kalachyova, Y., Mares, D., Jerabek, V., Zaruba, K., Ulbrich, P., Lapcak, L. & Lyutakov, O. (2016). The effect of silver grating and nanoparticles grafting for LSP–SPP coupling and SERS response intensification. *The Journal of Physical Chemistry C*, *120*(19), 10569-10577.

[6]. Yaremchuk, I., Petrovska, H., Karelko, I., Fitio, V., & Bobitski, Y. (2017, April). Optimization of the grating-based structures for the efficient SERS substrates. In *2017 IEEE 37th International Conference on Electronics and Nanotechnology (ELNANO)* (pp. 119-123). IEEE.

[7]. Rycenga, M., Cobley, C. M., Zeng, J., Li, W., Moran, C. H., Zhang, Q., ... & Xia, Y. (2011). Controlling the synthesis and assembly of silver nanostructures for plasmonic applications. *Chemical reviews*, *111*(6), 3669-3712.

[8]. Petrovska, H. A., Yaremchuk, I. Y., Fitio, V. M., Suriadova, O. D., & Bobitski, Y. V. (2016, September). Optimization metal-coated gratings for sensors applications. In *2016 IEEE 13th International Conference on Laser and Fiber-Optical Networks Modeling (LFnm)* (pp. 30-31). IEEE.

[9]. Zhang, J., Irannejad, M., & Cui, B. (2015). Bowtie nanoantenna with single-digit nm gap for surface-enhanced Raman scattering (SERS). *Plasmonics*, *10*(4), 831-837.

[10]. Gupta, N., & Dhawan, A. (2018). Bridged-bowtie and cross bridged-bowtie nanohole arrays as SERS substrates with hotspot tunability and multi-wavelength SERS response. *Optics Express*, *26*(14), 17899-17915.

[11]. Kleinman, S. L., Frontiera, R. R., Henry, A. I., Dieringer, J. A., & Van Duyne, R. P. (2013). Creating, characterizing, and controlling chemistry with SERS hot spots. *Physical Chemistry Chemical Physics*, *15*(1), 21-36.

[12]. Wang, L., Cai, L., Zhang, J., Bai, W., Hu, H., & Song, G. (2011). Design of plasmonic bowtie nanoring array with high sensitivity and reproducibility for surface-enhanced Raman scattering spectroscopy. *Journal of Raman Spectroscopy*, *42*(6), 1263-1266.

[13]. Zhan, P., Wen, T., Wang, Z. G., He, Y., Shi, J., Wang, T., ... & Ding, B. (2018). DNA Origami Directed Assembly of Gold Bowtie Nanoantennas for Single-Molecule Surface-Enhanced Raman Scattering. *Angewandte Chemie International Edition*, *57*(11), 2846-2850.

[14]. Feng, L., Ma, R., Wang, Y., Xu, D., Xiao, D., Liu, L., & Lu, N. (2015). Silver-coated elevated bowtie nanoantenna arrays: Improving the near-field enhancement of gap cavities for highly active surface-enhanced Raman scattering. *Nano Research*, *8*(11), 3715-3724.

[15]. Laha, R., Das, G. M., Ranjan, P., & Dantham, V. R. (2018, May). Experimental optimization during SERS application. In *AIP Conference Proceedings* (Vol. 1953, No. 1, p. 030188). AIP Publishing LLC.

[16]. Basu, S. (2017). Surface Enhanced Raman Scattering (SERS) Substrates and Probes.

[17]. García-Vidal, F. J., & Pendry, J. B. (1996). Collective theory for surface enhanced Raman scattering. *Physical Review Letters*, *77*(6), 1163.

[18]. Gopinath, A., Boriskina, S. V., Reinhard, B. M., & Dal Negro, L. (2009). Deterministic aperiodic arrays of metal nanoparticles for surface-enhanced Raman scattering (SERS). *Optics Express*, *17*(5), 3741-3753.

[19]. Fromm, D. P., Sundaramurthy, A., Schuck, P. J., Kino, G., & Moerner, W. E. (2004). Gap-dependent optical coupling of single "bowtie" nanoantennas resonant in the visible. *Nano letters*, *4*(5), 957-961.

[20]. Jäckel, F., Kinkhabwala, A. A., & Moerner, W. E. (2007). Gold bowtie nanoantennas for surface-enhanced Raman scattering under controlled electrochemical potential. *Chemical Physics Letters*, *446*(4-6), 339-343.

[21]. Ko, H., Singamaneni, S., & Tsukruk, V. V. (2008). Nanostructured surfaces and assemblies as SERS media. *Small*, *4*(10), 1576-1599.

[22]. Ko, K. D., Kumar, A., Fung, K. H., Ambekar, R., Liu, G. L., Fang, N. X., & Toussaint Jr, K. C. (2011). Nonlinear optical response from arrays of Au bowtie nanoantennas. *Nano letters*, *11*(1), 61-65.

[23]. Valovič, M., Akers, R., Cunningham, G., Garzotti, L., Lloyd, B., Muir, D., ... & Walsh, M. (2009). Scaling of H-mode energy confinement with Ip and BT in the MAST spherical tokamak. *Nuclear Fusion*, *49*(7), 075016.

[24]. Galarreta, B. C., Norton, P. R., & Lagugne-Labarthet, F. (2011). SERS detection of streptavidin/biotin monolayer assemblies. *Langmuir*, *27*(4), 1494-1498.

[25]. Xu, D., Liu, L., Teng, F., Wu, F., & Lu, N. (2016). Trapping analyte molecules in hotspots with modified free-standing silver bowtie nanostructures for SERS detection. *RSC advances*, *6*(87), 84480-84484.

[26]. Sharac, N., Sharma, H., Veysi, M., Sanderson, R. N., Khine, M., Capolino, F., & Ragan, R. (2016). Tunable optical response of bowtie nanoantenna arrays on thermoplastic substrates. *Nanotechnology*, *27*(10), 105302.

[27]. Rycenga, M., Camargo, P. H., Li, W., Moran, C. H., & Xia, Y. (2010). Understanding the SERS effects of single silver nanoparticles and their dimers, one at a time. *The journal of physical chemistry letters*, *1*(4), 696-703.

[28]. Chen, X., Jiang, C., & Yu, S. (2014). Nanostructured materials for applications in surface-enhanced Raman scattering. CrystEngComm, 16(43), 9959-9973.

[29]. Kennedy, B. J., Spaeth, S., Dickey, M., & Carron, K. T. (1999). Determination of the distance dependence and experimental effects for modified SERS substrates based on self-assembled monolayers formed using alkanethiols. *The Journal of Physical Chemistry B*, *103*(18), 3640-3646.

[30]. Pettinger, B., Domke, K. F., Zhang, D., Schuster, R., & Ertl, G. (2007). Direct monitoring of plasmon resonances in a tip-surface gap of varying width. *Physical Review B*, *76*(11), 113409.

[31]. Leem, J., Kang, H. W., Ko, S. H., & Sung, H. J. (2014). Controllable Ag nanostructure patterning in a microfluidic channel for real-time SERS systems. *Nanoscale*, *6*(5), 2895-2901.

[32]. Cao, Y., Li, D., Jiang, F., Yang, Y., & Huang, Z. (2013). Engineering metal nanostructure for SERS application. *Journal of Nanomaterials*, *2013*.

[33]. Sajanlal, P. R., & Pradeep, T. (2012). Functional hybrid nickel nanostructures as recyclable SERS substrates: detection of explosives and biowarfare agents. *Nanoscale*, *4*(11), 3427-3437.

[34]. Fateixa, S., Nogueira, H. I., & Trindade, T. (2015). Hybrid nanostructures for SERS: materials development and chemical detection. *Physical Chemistry Chemical Physics*, *17*(33), 21046-21071.

[35]. Fleischmann, M., Hendra, P., & McQuillan, A. (1974). RAMAN SPECTRA OF PYRIDINE ADSORBED AT A SILVER ELEC. *Chemical physics letters*, *26*(2).

[36]. Marques, P. A., Nogueira, H. I., Pinto, R. J., Neto, C. P., & Trindade, T. (2008). Silver-bacterial cellulosic sponges as active SERS substrates. *Journal of Raman Spectroscopy: An International Journal for Original Work in all Aspects of Raman Spectroscopy, Including Higher Order Processes, and also Brillouin and Rayleigh Scattering*, *39*(4), 439-443.

[37]. Sinha, G., Depero, L. E., & Alessandri, I. (2011). Recyclable SERS substrates based on Au-coated ZnO nanorods. *ACS applied materials & interfaces*, *3*(7), 2557-2563.

[38]. Cınta, S., Vogel, E., Maniu, D., Aluas, M., Iliescu, T., Cozar, O., & Kiefer, W. (1999). SERS mechanisms of the Vitamin PP on different Au and Ag surfaces. *Journal of molecular structure*, *482*, 679-684.

[39]. Giallongo, G., Pilot, R., Durante, C., Rizzi, G. A., Signorini, R., Bozio, R., ... & Granozzi, G. (2011). Silver nanoparticle arrays on a DVD-derived template: an easy&cheap SERS substrate. *Plasmonics*, *6*(4), 725.

[40]. Sinha, G., Depero, L. E., & Alessandri, I. (2011). Recyclable SERS substrates based on Au-coated ZnO nanorods. *ACS applied materials & interfaces*, *3*(7), 2557-2563.

[41]. Liu, S., Yu, J., Wang, T., & Li, F. (2017). A multifunctional Ag/PAOCG reusable substrate for p-nitrophenol reduction and SERS applications. *Journal of Materials Science*, *52*(24), 13748-13763.

[42]. Yu, J., Shen, M., Liu, S., Li, F., Sun, D., & Wang, T. (2017). A simple technique for direct growth of Au into a nanoporous alumina layer on conductive glass as a reusable SERS substrate. *Applied Surface Science*, *406*, 285-293.

[43]. ul Ahmad, A., Liang, H., Ali, S., Abbas, Q., Farid, A., Ali, A., ... & Farooq, Z. (2020). Cheap, reliable, reusable, thermally and chemically stable fluorinated hexagonal boron nitride nanosheets coated Au nanoparticles substrate for surface enhanced Raman spectroscopy. *Sensors and Actuators B: Chemical*, *304*, 127394.

[44]. Shan, Y., Yang, Y., Cao, Y., Yin, H., Long, N. V., & Huang, Z. (2015). Hydrogenated black TiO 2 nanowires decorated with Ag nanoparticles as sensitive and reusable surface-enhanced Raman scattering substrates. *RSC Advances*, *5*(44), 34737-34743.

[45]. Yu, C. C., Chou, S. Y., Tseng, Y. C., Tseng, S. C., Yen, Y. T., & Chen, H. L. (2015). Single-shot laser treatment provides quasi-three-dimensional paper-based substrates for SERS with attomolar sensitivity. *Nanoscale*, *7*(5), 1667-1677.

[46]. Zhu, Y., Zhang, L., & Yang, L. (2015). Designing of the functional paper-based surface-enhanced Raman spectroscopy substrates for colorants detection. *Materials Research Bulletin*, *63*, 199-204.

[47]. Zhang, W., Li, B., Chen, L., Wang, Y., Gao, D., Ma, X., & Wu, A. (2014). Brushing, a simple way to fabricate SERS active paper substrates. *Analytical Methods*, *6*(7), 2066-2071.

[48]. Cialla, D., März, A., Böhme, R., Theil, F., Weber, K., Schmitt, M., & Popp, J. (2012). Surface-enhanced Raman spectroscopy (SERS): progress and trends. *Analytical and bioanalytical chemistry*, *403*(1), 27-54.

[49]. Le Ru, E. C., Grand, J., Felidj, N., Aubard, J., Levi, G., Hohenau, A., ... & Etchegoin, P. G. (2008). Experimental verification of the SERS electromagnetic model beyond the| E| 4 approximation: polarization effects. *The Journal of Physical Chemistry C*, *112*(22), 8117-8121.

[50]. Le Ru, E. C., Meyer, M., Blackie, E., & Etchegoin, P. G. (2008). Advanced aspects of electromagnetic SERS enhancement factors at a hot spot. *Journal of Raman Spectroscopy: An International Journal for Original Work in all Aspects of Raman Spectroscopy, Including Higher Order Processes, and also Brillouin and Rayleigh Scattering*, *39*(9), 1127-1134.

[51]. Fang, J., Yi, Y., Ding, B., & Song, X. (2008). A route to increase the enhancement factor of surface enhanced Raman scattering (SERS) via a high density Ag flower-like pattern. *Applied physics letters*, *92*(13), 131115.

[52]. Kovacs, G. J., Loutfy, R. O., Vincett, P. S., Jennings, C., & Aroca, R. (1986). Distance dependence of SERS enhancement factor from Langmuir-Blodgett monolayers on metal island films: evidence for the electromagnetic mechanism. *Langmuir*, *2*(6), 689-694.

[53]. Zhang, J., Zhang, L., & Xu, W. (2012). Surface plasmon polaritons: physics and applications. *Journal of Physics D: Applied Physics*, *45*(11), 113001.

[54]. Quinten, M., Leitner, A., Krenn, J. R., & Aussenegg, F. R. (1998). Electromagnetic energy transport via linear chains of silver nanoparticles. *Optics letters*, *23*(17), 1331-1333.

[55]. Weeber, J. C., Dereux, A., Girard, C., Krenn, J. R., & Goudonnet, J. P. (1999). Plasmon polaritons of metallic nanowires for controlling submicron propagation of light. *Physical Review B*, *60*(12), 9061.

[56]. Oulton, R. F., Sorger, V. J., Genov, D. A., Pile, D. F. P., & Zhang, X. (2008). A hybrid plasmonic waveguide for subwavelength confinement and long-range propagation. *nature photonics*, *2*(8), 496-500.

[57]. Sajanlal, P. R., & Pradeep, T. (2008). Electric-Field-Assisted Growth of Highly Uniform and Oriented Gold Nanotriangles on Conducting Glass Substrates. *Advanced Materials*, *20*(5), 980-983.

[58]. Millstone, J. E., Park, S., Shuford, K. L., Qin, L., Schatz, G. C., & Mirkin, C. A. (2005). Observation of a quadrupole plasmon mode for a colloidal solution of gold nanoprisms. *Journal of the American Chemical Society*, *127*(15), 5312-5313.

[59]. Hao, F., Nehl, C. L., Hafner, J. H., & Nordlander, P. (2007). Plasmon resonances of a gold nanostar. *Nano letters*, *7*(3), 729-732.

[60]. Hao, F., Nehl, C. L., Hafner, J. H., & Nordlander, P. (2007). Plasmon resonances of a gold nanostar. *Nano letters*, *7*(3), 729-732.

[61]. Chen, L., Han, X., Yang, J., Zhou, J., Song, W., Zhao, B., ... & Ozaki, Y. (2011). Detection of proteins on silica–silver core–shell substrates by surface-enhanced Raman spectroscopy. *Journal of colloid and interface science*, *360*(2), 482-487.

[62]. Péron, O., Rinnert, E., Toury, T., De La Chapelle, M. L., & Compere, C. (2011). Quantitative SERS sensors for environmental analysis of naphthalene. *Analyst*, *136*(5), 1018-1022.

[63]. Zhang, J., Irannejad, M., & Cui, B. (2015). Bowtie nanoantenna with single-digit nm gap for surface-enhanced Raman scattering (SERS). *Plasmonics*, *10*(4), 831-837.

[64]. Hecht, B., Bielefeldt, H., Novotny, L., Inouye, Y., & Pohl, D. W. (1996). Local excitation, scattering, and interference of surface plasmons. *Physical review letters*, *77*(9), 1889.

[65]. McLellan, J. M., Siekkinen, A., Chen, J., & Xia, Y. (2006). Comparison of the surface-enhanced Raman scattering on sharp and truncated silver nanocubes. *Chemical Physics Letters*, *427*(1-3), 122-126.

[66]. Shen, A., Chen, L., Xie, W., Hu, J., Zeng, A., Richards, R., & Hu, J. (2010). Triplex Au–Ag–C core–shell nanoparticles as a novel Raman label. *Advanced Functional Materials*, *20*(6), 969-975.

[67]. Ghosh, S. K., & Pal, T. (2007). Interparticle coupling effect on the surface plasmon resonance of gold nanoparticles: from theory to applications. *Chemical reviews*, *107*(11), 4797-4862.

[68]. Sherry, L. J., Jin, R., Mirkin, C. A., Schatz, G. C., & Van Duyne, R. P. (2006). Localized surface plasmon resonance spectroscopy of single silver triangular nanoprisms. *Nano letters*, *6*(9), 2060-2065.

[69]. Jeanmaire, D. L., & Van Duyne, R. P. (1977). Surface Raman spectroelectrochemistry: Part I. Heterocyclic, aromatic, and aliphatic amines adsorbed on the anodized silver electrode. *Journal of electroanalytical chemistry and interfacial electrochemistry*, *84*(1), 1-20.

[70]. Baker, G. A., & Moore, D. S. (2005). Progress in plasmonic engineering of surface-enhanced Raman-scattering substrates toward ultra-trace analysis. *Analytical and bioanalytical chemistry*, *382*(8), 1751-1770.

[71]. Li, K., Stockman, M. I., & Bergman, D. J. (2003). Self-similar chain of metal nanospheres as an efficient nanolens. *Physical review letters*, *91*(22), 227402.

[72]. Binder, W. H. (2005). Supramolecular assembly of nanoparticles at liquid–liquid interfaces. *Angewandte Chemie International Edition*, *44*(33), 5172-5175.

[73]. Liao, J., Bernard, L., Langer, M., Schönenberger, C., & Calame, M. (2006). Reversible formation of molecular junctions in 2D nanoparticle arrays. *Advanced Materials*, *18*(18), 2444-2447.

[74]. Genson, K. L., Holzmueller, J., Jiang, C., Xu, J., Gibson, J. D., Zubarev, E. R., & Tsukruk, V. V. (2006). Langmuir− blodgett monolayers of gold nanoparticles with amphiphilic shells from v-shaped binary polymer arms. *Langmuir*, *22*(16), 7011-7015.

[75]. Lee, S. J., Morrill, A. R., & Moskovits, M. (2006). Hot spots in silver nanowire bundles for surface-enhanced Raman spectroscopy. *Journal of the American Chemical Society*, *128*(7), 2200-2201.

[76]. Wang, H. H., Liu, C. Y., Wu, S. B., Liu, N. W., Peng, C. Y., Chan, T. H., ... & Wang, Y. L. (2006). Highly raman-enhancing substrates based on silver nanoparticle arrays with tunable sub-10 nm gaps. *Advanced Materials*, *18*(4), 491-495.

[77]. Kneipp, K., Wang, Y., Kneipp, H., Itzkan, I., Dasari, R. R., & Feld, M. S. (1996). Population pumping of excited vibrational states by spontaneous surface-enhanced Raman scattering. *Physical review letters*, *76*(14), 2444.

[78]. Nie, S., & Emory, S. R. (1997). Probing single molecules and single nanoparticles by surface-enhanced Raman scattering. *science*, *275*(5303), 1102-1106.

[79]. Lezec, H. J., Degiron, A., Devaux, E., Linke, R. A., Martin-Moreno, L., Garcia-Vidal, F. J., & Ebbesen, T. W. (2002). Beaming light from a subwavelength aperture. *science*, *297*(5582), 820-822.

[80]. Oulton, R. F., Sorger, V. J., Zentgraf, T., Ma, R. M., Gladden, C., Dai, L., & Zhang, X. (2009). Plasmon lasers at deep subwavelength scale. *Nature*, *461*(7264), 629-632.

[81]. Kneipp, K., Wang, Y., Kneipp, H., Perelman, L. T., Itzkan, I., Dasari, R. R., & Feld, M. S. (1997). Single molecule detection using surface-enhanced Raman scattering (SERS). *Physical review letters*, *78*(9), 1667.

[82]. Xu, W., Zhang, J., Zhang, L., Hu, X., & Cao, X. (2009). Ultrasensitive detection using surface enhanced raman scattering from silver nanowire arrays in anodic alumina membranes. *Journal of nanoscience and nanotechnology*, *9*(8), 4812-4816.

[83]. Fang, Y., Wei, H., Hao, F., Nordlander, P., & Xu, H. (2009). Remote-excitation surface-enhanced Raman scattering using propagating Ag nanowire plasmons. *Nano letters*, *9*(5), 2049-2053.

[84]. Zijlstra, P., Chon, J. W., & Gu, M. (2009). Five-dimensional optical recording mediated by surface plasmons in gold nanorods. *nature*, *459*(7245), 410-413.

[85]. Stenzel, O., Stendal, A., Voigtsberger, K., & Von Borczyskowski, C. (1995). Enhancement of the photovoltaic conversion efficiency of copper phthalocyanine thin film devices by incorporation of metal clusters. *Solar energy materials and solar cells*, *37*(3-4), 337-348.

[86]. Zhao, Yong & Tong, Rui-jie & Xia, Feng & Peng, Yun. (2019). Current status of optical fiber biosensor based on surface plasmon resonance. Biosensors and Bioelectronics. 142. 111505. 10.1016/j.bios.2019.111505.

[87]. Slusher, R. B., & Derr, V. E. (1975). Temperature dependence and cross sections of some Stokes and anti-Stokes Raman lines in ice Ih. Applied Optics, 14(9), 2116-2120.

[88]. Ritchie, R. H. (1957). Plasma losses by fast electrons in thin films. Physical review, 106(5), 874.

[89]. Polman, A., & Atwater, H. A. (2005). Plasmonics: optics at the nanoscale. Materials Today, 8(1), 56.

[90]. Maier, S. A. (2007). *Plasmonics: fundamentals and applications*. Springer Science & Business Media.

[91]. Kneipp, K., Kneipp, H., Itzkan, I., Dasari, R. R., & Feld, M. S. (2002). Surface-enhanced Raman scattering and biophysics. *Journal of Physics: Condensed Matter*, *14*(18), R597.

[92]. Kerker, M., Wang, D. S., & Chew, H. (1980). Surface enhanced Raman scattering (SERS) by molecules adsorbed at spherical particles: errata. *Applied optics*, *19*(24), 4159-4174.